SPATIAL DISTRIBUTION OF CHARGED PARTICLES ALONG THE ION-OPTICAL AXIS IN ELECTRON CYCLOTRON RESONANCE ION SOURCES
-EXPERIMENTAL RESULTS-

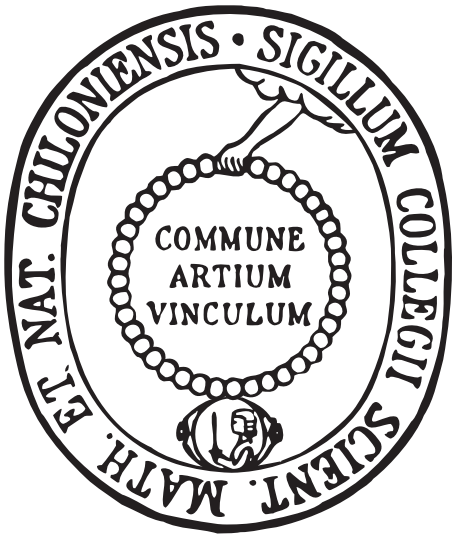

Dissertation
zur Erlangung des Doktorgrades
der Mathematisch-Naturwissenschaftlichen Fakultät
der Christian-Albrechts-Universität zu Kiel
vorgelegt von

LAURI PANITZSCH

– Kiel, Dezember 2012 –

Lauri Panitzsch:
Spatial Distribution of Charged Particles Along the Ion-Optical Axis in Electron Cyclotron Resonance Ion Sources
-Experimental Results-

ERSTER GUTACHTER (SUPERVISOR):
Prof. Dr. R. F. Wimmer-Schweingruber

ZWEITER GUTACHTER (ADVISOR):
Prof. Dr. H. Kersten

TAG DER MÜNDLICHEN PRÜFUNG:
08.02.2013

ZUM DRUCK GENEHMIGT:
08.02.2013

gez. Prof. Dr. W. J. Duschl, Dekan

ABSTRACT

The experimental determination of the spatial distribution of charged particles along the ion-optical axis in electron cyclotron resonance ion sources (ECRIS) defines the focus of this thesis. The spatial distributions of different ion species were obtained in the object plane of the bending magnet (≈ 45 cm downstream from the plasma electrode) and in the plane of the plasma electrode itself, both in high spatial resolution. The results show that each of the different ion species forms a bloated, triangular structure in the aperture of the plasma electrode. The geometry and the orientation of these structures are defined by the superposition of the radial and axial magnetic fields. The radial extent of each structure is defined by the charge of the ion. Higher charge states occupy smaller, more concentrated structures. The total current density increases towards the center of the plasma electrode. The circular and star-like structures that can be observed in the beam profiles of strongly focused, extracted ion beams are each dominated by ions of a single charge state. In addition, the spatially resolved current density distribution of charged particles in the plasma chamber that impinge on the plasma electrode was determined, differentiating between ions and electrons. The experimental results of this work show that the electrons of the plasma are strongly connected to the magnetic field lines in the source and thus spatially well confined in a triangular-like structure. The intensity of the electrons increases towards the center of the plasma electrode and the plasma chamber, as well. These electrons are surrounded by a spatially far less confined and less intense ion population.

All the findings mentioned above were already predicted in parts by simulations of different groups. However, the results presented within this thesis represent the first (and by now only) direct experimental verification of those predictions and are qualitatively transferable to other ECR ion sources with hexapolar radial confinement.

Furthermore, based on the results a new theory for the creation of the different sputter and deposition marks inside the plasma chamber of ECR ion sources is proposed. The thin and deeply sputtered grooves seem to stem from the high-energetic electrons while the surrounding, broad halo is ion-induced.

The custom-built detectors (for each of the mentioned axial positions a different detector adapted to the special demands and purposes was developed) are presented in detail within this work as well, with one of these detectors (the "Faraday cup array" or FCA) now having established itself as our standard beam-profile measuring device.

ZUSAMMENFASSUNG

Die räumliche Verteilung von geladenen Teilchen entlang der Achse einer Elektron-Zyklotron-Resonanz (EZR) Ionenquelle experimentell zu bestimmen, stellt den Fokus dieser Arbeit dar. In der Objektebene des Sektormagneten (≈ 45 cm hinter der Plasmaelektrode) und an der Plasmaelektrode selbst wurde die räumliche Verteilung verschiedener Ionenspezies des extrahierten Ionenstrahls in hoher Auflösung bestimmt. Es zeigt sich, dass die einzelnen Ionenspezies an der Plasmaelektrode jeweils zu aufgeblähten, triangularen Strukturen zusammengefasst werden können. Die Geometrie und die Ausrichtung dieser Strukturen werden von der Überlagerung der radialen und axialen Magnetfelder vorgegeben. Die radiale Ausdehnung der Strukturen hängt invers vom Ladungszustand ab. Hoch geladene Ionen weisen dabei eine geringere radiale Ausdehnung auf. Die Gesamtstromdichte steigt zum Zentrum der Plasmaelektrode hin an. Die Ringe und die sternähnlichen Strukturen, die bei stark fokussierten Ionenstrahlen im Strahlprofil sichtbar werden, werden jeweils durch Ionen eines Ladungszustandes dominiert. Außerdem wurde die ortsaufgelöste Stromdichteverteilung der geladenen Teilchen gemessen, die in der Plasmakammer auf die Plasmaelektrode einfallen. Hier wurde ausschließlich zwischen Ionen und Elektronen unterschieden. Diese Ergebnisse zeigen, dass die Elektronen stark an das Magnetfeld gebunden sind und daher zu räumlich stark begrenzten, triangularen Strukturen zusammengefasst sind. Die Intensität der Elektronen steigt zum Zentrum der Plasmaelektrode und der Plasmakammer hin an und wird von einer räumlich breiteren und weniger dominanten Ionenverteilung umgeben.

Sämtliche oben erwähnten Erkenntnisse wurden bereits in Teilen in Simulationen verschiedener Gruppen vorhergesagt, konnten jedoch erst (und bisher ausschließlich) durch die hier präsentierten Messungen experimentell bestätigt werden. Die Ergebnisse sind qualitativ auf andere EZR-Ionenquellen übertragbar, deren radialer magnetischer Einschluß über einen Hexapol gewährleistet ist.

Basierend auf den Messergebnissen wurde außerdem eine Theorie für das Entstehen der Zerstäubungs- und Ablagerungsmale innerhalb der Plasmakammer von EZR-Ionenquellen aufgestellt. Die schmalen und verhältnismäßig tiefen Zerstäubungsmale scheinen durch hochenergetische Elektronen hervorgerufen zu werden, die von breiteren, ioneninduzierten Malen umgeben werden.

Die verwendeten Detektoren (für jede der erwähnten axialen Positionen wurde ein anderer, speziell an die Anforderungen angepasster Detektortyp entwickelt) werden in dieser Arbeit ebenfalls im Detail erläutert. Einer der Detektoren (das "Faraday-cup array", kurz FCA) hat sich dabei als Standard für die Erfassung von Strahlprofilen entlang der ionenoptischen Achse etabliert.

PUBLICATIONS

Direct high-resolution ion beam-profile imaging using a position-sensitive Faraday cup array Lauri Panitzsch, Michael Stalder, and Robert F. Wimmer-Schweingruber, Rev. Sci. Instrum. 80, 113302 (2009), DOI:10.1063/1.3246787

Spatially resolved measurements of electron cyclotron resonance ion source beam profile characteristics Lauri Panitzsch, Michael Stalder, and Robert F. Wimmer-Schweingruber, Rev. Sci. Instrum. 82, 033302 (2011), DOI:10.1063/1.3553013

Spatially resolved charge-state and current-density distributions at the extraction of an electron cyclotron resonance ion source Lauri Panitzsch, Thies Peleikis, Michael Stalder, and Robert F. Wimmer-Schweingruber, Rev. Sci. Instrum. 82, 093302 (2011), DOI:10.1063/1.3637462

Current density distributions and sputter marks in electron cyclotron resonance ion sources Lauri Panitzsch, Thies Peleikis, Stephan Böttcher, Michael Stalder, and Robert F. Wimmer-Schweingruber, Rev. Sci. Instrum. 84, 013303 (2013), DOI:10.1063/1.4774052

PROCEEDINGS

Preliminary results of spatially resolved ECR ion beam profile investigations Lauri Panitzsch, Michael Stalder, and Robert F. Wimmer-Schweingruber, The 19th International Workshop on Electron Cyclotron Resonance Ion Sources (ECRIS-2010), Grenoble, France

A new system for monitoring transverse beam profiles Lauri Panitzsch, Stephan Böttcher, Michael Stalder, and Robert F. Wimmer-Schweingruber, The 2012 Beam Instrumentation Workshop (BIW12), Newport News, Virginia, USA

Experimental results: charge-state- and current-density distributions at the plasma electrode of an ECR ion source Lauri Panitzsch, Thies Peleikis, Michael Stalder, and Robert F. Wimmer-Schweingruber, The 20th International Workshop on Electron Cyclotron Resonance Ion Sources (ECRIS-2012), Sydney, Australia

EBIS engineers at least understand
why their source performs poorly,
whereas the poor ECRIS people
don't even understand
why the ECRIS performs so well.

[joke muttered in the eighties by accelerator people,
as conveyed by R. Geller]

DANKSAGUNG

An erster Stelle möchte ich Herrn Prof. Dr. Robert F. Wimmer-Schweingruber meinen herzlichen Dank aussprechen, unter seiner freundlichen und motivierenden Betreuung diese Arbeit anfertigen zu können. Das von ihm entgegengebrachte Vertrauen und die Offenheit zur Umsetzung eigener Ideen habe ich stets sehr geschätzt. Dank ihm kam die Ionenquelle nach Kiel und bescherte mir eine ebenso spannende wie herausfordernde Arbeit.

Ebenso möchte ich mich bei Herrn Dr. Michael Stalder herzlich bedanken, der mit der Entwicklung der Kieler Ionenquelle den Grundstein für die folgenden Untersuchungen gelegt hat. Ein paar konstruktionelle Besonderheiten haben sich dabei als besonders wertvoll erwiesen. Mein Verständnis vieler Grundlagen geht auf unsere ausgedehnten Gespräche zurück, die erfreulicher Weise nicht ausschließlich beruflicher Natur waren. Ein besonderer Dank gilt auch Frau Christiane Helmke insbesondere für ihre tatkräftige Unterstützung in vielen technischen und handwerklichen Belangen, sowie Herrn Stefan Kolbe, der das stetig wachsende Projekt im CAD in Zaum hält. Auch Herrn Thies Peleikis gebührt mein Dank für die fruchtbaren Diskussionen und Hilfen beim Erstellen dieser gesamten Arbeit. Es ist eine große Freude, mit ihm zusammen an der Ionenquelle zu arbeiten. Herr Dr. Stephan Böttcher war maßgeblich an der Entwicklung der neuen Elektronik des FCA beteiligt. Seine Erfahrung und sein Wissen im Bereich der Elektronik lassen sich beim Betrachten der entstandenen Hardware erahnen. Auch dafür ein großes Dankeschön. Mein Dank gilt außerdem Herrn Bent Ehresmann für das Korrekturlesen der Veröffentlichungen und Herrn Jan Grunau für die Bereitschaft, mir bei der Klärung vieler technischer und wissenschaftlicher Fragestellungen spontan zu helfen. Insgesamt hat mir das Arbeiten in dieser Gruppe aufgrund des ausgesprochen netten Klimas ausserordentlich gut gefallen. Nicht zuletzt möchte ich auch der Zentralen Werkstatt für ihre Dienste danken. Es hat mich stets fasziniert, mit welcher Präzision und Qualität dort unser Equipment entstanden ist.

Ein herzliches Dankeschön natürlich auch an meine Eltern und meine liebe Freundin, die gerade in der letzten Zeit noch mehr Geduld mit mir aufbringen musste!

CONTENTS

LIST OF TABLES

ACRONYMS

CDD	Current-Density Distribution
CSD	Charge-State Distribution
ECR	Electron Cyclotron Resonance
ECRH	Electron Cyclotron Resonance Heating
ECRIS	Electron Cyclotron Resonance Ion Source
FC	Faraday Cup
FCA	Faraday Cup Array
HCI	Highly-Charged Ion
LEBT	Low-Energy Beam Transport
MC	Monte Carlo
PIC	Particle-In-Cell
RG	Residual Gas
RGHE	Residual Gas (with) Helium
UHV	Ultra-High Vacuum

SYMBOLS

α	pitch angle
γ	Lorentz factor
λ	mean free path length
λ_D	Debye length
λ_s	sheath length
μ	magnetic moment
ω_c	cyclotron frequency
ω_{RF}	wave frequency

σ	cross section
τ	relaxation time
B	magnetic flux density
b_{min}	distance of closest approach
c_{si}	ion speed of sound
E_{kin}	kinetic energy
j_p	current density
m	mass *
n	density *
P_{kin}	kinetic pressure
P_{mag}	magnetic pressure
q	charge
r_c	cyclotron radius
T	temperature *
v	speed *
V_P	plasma potential
V_S	sheath potential

* index i corresponds to ions, index e corresponds to electrons

1

INTRODUCTION

Since their invention in the late 1970's by Richard Geller, Electron Cyclotron Resonance Ion Sources (ECRIS) have been continuously developed further. For many applications, high currents and high charge states are the most important performance parameters. According to the semi-empirical scaling-laws given by Geller [1] both parameters can be optimized by injecting microwaves of higher frequencies into the plasma. This has to be accompanied by an increase of the confining magnetic fields as this is necessary for the electron cyclotron resonance heating (ECRH) condition (see section 2.2). But it is not only the particle source that needs optimization, also beam losses during the low-energy beam transport (LEBT) need to be minimized as they can lead to a significant decrease of the effectively transfered beam. The so-called transmissivity is influenced by the emittance of the source to a large extend. However, an increase of the magnetic fields leads to an increase of the emittance at the extraction as well [1]. Therefore, the emittance of the beam at the extraction is an additional key parameter for optimization. To optimize the extraction of charged particles from ion sources has become a task of great importance that often is approached by simulations. These ion-extraction simulations then take the electric and magnetic fields present in the extraction region into account and consider the interactions between the different particles [8, 9, 10, 11]. To achieve results as realistic as possible the (true) spatial distribution of the various ion species in the plane of the plasma electrode needs to be included in the simulations. This represents a very challenging task which, again, is coped by the use of simulations. These simulations emulate the plasma formation in the ion source and also require three dimensions (3D) for realistic results as the problem is not rotationally symmetric. These codes for plasma formation [12, 7, 5] do not only yield the particle distribution in the plane of the plasma electrode, they also provide further insight into the processes inside the plasma. The true geometry of the distribution present in the plasma chamber is conserved in the extracted ion beam and only modified by the ion-optical elements along the beam line. Thus, experimental observations of the spatially resolved distribution of different ion species at different axial positions (with the focus on the extraction region and close to the source) would provide very valuable data to verify these simulations. In addition, knowledge of the spatial characteristics of the beam and the plasma at the extraction will help to further understand the process of ECR plasma formation itself.

However, to our best knowledge, such experimental data has not been reported in the literature so far: The beam profiles that are recorded along the beam line before passing the bending magnet do not differentiate between the various ion species or charge states but only show the total current distribution. Close to the extraction (which includes the aperture of the plasma electrode) no spatially resolved measurements of the beam profile have been performed at all. In particular,

there are no spatially resolved measurements of different ion species or charge states.

Therefore, a couple of fundamental predictions have not been verified experimentally yet: It was proposed [13, 3, 14] that each of the hollow rings and star-like structures in strongly focused ion beams is dominated by one single ion species. In the plane of the plasma electrode, the different ion species are proposed to form triangular structures of the same orientation but different sizes with the highly-charged ions being confined to smaller effective radii [12].

To overcome this lack of data thus defines the focus of this thesis. We have performed measurements of the spatial distribution of charged particles at multiple positions along the ion-optical axis in our electron cyclotron resonance ion source (ECRIS) with the emphasis on the extraction region and the plasma chamber.

This thesis is structured as follows: First, a theoretical background of the plasma formation and extraction in ECR ion sources is given. After that, four papers published in peer-reviewed journals are included in this work, each introduced by a short overview. The papers are presented in chronological order of publication as this order also represents a systematically reasonable thread with regard to the contents. By this choice the investigations start at the greatest distance to the ion source and approach the plasma with each included publication.

Following this thread a new kind of detector system (the "Faraday cup array" or FCA [15]) for the acquisition of beam profiles is presented first. Its main characteristics will be summarized and compared to other existing detector types for that purpose.

The next publication can be seen as a further demonstration of the detector's performance though its major scientific yield is to give the first experimental proof that each of the hollow rings and star-like structures in strongly focused ion beams extracted from ECRIS with hexapolar radial confinement is dominated by ions of the same charge state [16]. A $\frac{m}{q}$-dependence was not detectable with this technique because of the small mass differences. The measurements were performed at an axial distance of about 45 cm to the plasma electrode.

Further approaching the plasma the next publication presents the beam profile in the plane of the plasma electrode. At this position, so far no beam profiles have been acquired. Beyond that, the beam profiles presented within this publication resolve the spatial distribution of selected charge states in that plane [17]. The results are discussed in detail.

The last included paper summarizes the investigations performed inside the plasma chamber. The spatial distribution of charged particles (differentiating between ions and electrons) impinging onto the plasma electrode was recorded. The results show a sharply confined, star-shaped electron population that is strongly connected to the magnetic fields. The surrounding ions show the same geometry but are far less confined and less intense [18]. Based on these results, a new explanation for the creation of the different sputter marks inside the plasma chamber of ECR ion sources is developed. We propose the hot electrons of the plasma with $E_{kin} \gtrsim 200\,\text{keV}$ (which is the threshold energy for electron-induced sputtering of solids) to cause the thin and deeply sputtered grooves, as observed in many high-performance ECRIS. The much broader halo surrounding the thin

structures we agree to be caused by the ions of the plasma.

The findings reported in these publications are summarized in the conclusions and where possible compared to the simulations (see chap. 8).

2

ECR PLASMA FORMATION

ECR ion sources are well-suited for the production of highly charged ions of multiple elements and are used in many applications [19]. The absence of wearing parts makes these sources very reliable and suitable for long-term operation. The achievements in current extraction and mean charge state have been strongly increasing and subject of intense investigations around the world. The key mechanisms in these sources which determine the formation and maintain the plasma are discussed below. They are: magnetic structures, ECR heating, charged-particle confinement, collisions, ionization, and charge-exchange processes.

2.1 MAGNETIC CONFINEMENT

To ignite and sustain an ECR plasma, a well-adjusted microwave is injected into the low-pressure gas in the plasma chamber. The latter is surrounded and penetrated by sophisticated magnetic field structures. These structures are typically a superposition of coaxial and radial magnetic contributions which serve to confine the plasma and ensure electron heating. The superposition of the magnetic field structures results a magnetic configuration called "minimum-B-structure": The magnetic flux density reaches a minimum at the center and increases in all directions.

Axial magnetic confinement

The magnetic bottle is established in axial direction by the use of solenoids and/or magnets. By increasing the magnetic flux density at both ends of the confinement region the electrons of the plasma are trapped and gyrate back and forth around the magnetic field lines. As will be pointed out below, the ions of the plasma are far too collisional to be effectively coupled to the magnetic field lines. Nevertheless, the following discussion is in general valid for both, ions and electrons.

Charged particles that oscillate in a magnetic bottle follow helical paths around the magnetic field lines. Their cyclotron (or Larmor or gyro) -radius r_c and -frequency ω_c are given as

$$r_c = \frac{m v_\perp}{|q| B} \tag{1}$$

and

$$\omega_c = \frac{|q| B}{m} \tag{2}$$

respectively, with m being the particle's mass, $v_\perp$ its velocity perpendicular to the magnetic field lines, q the charge, and B the local magnetic flux density. In the relativistic case, the increase of the mass needs to be considered ($m = \gamma m_0$). In

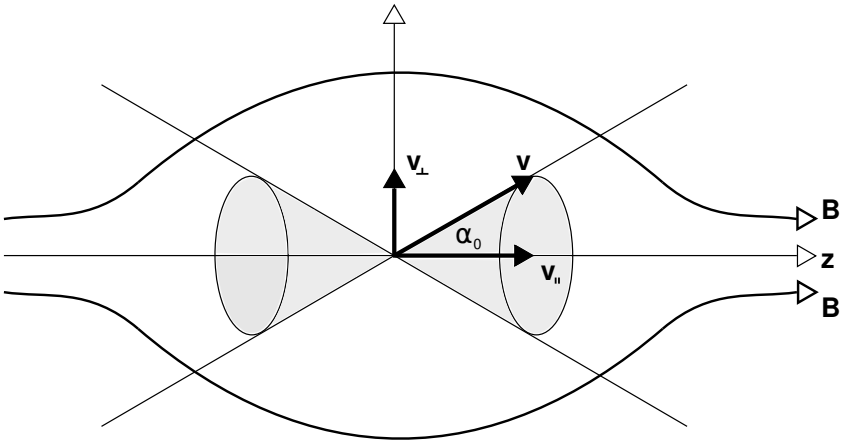

Figure 1: The pitch angle α_0 and the loss cone in a coaxial magnetic mirror system. The loss cone is tinted in gray. After [1].

the absence of collisions and electric fields their kinetic energy E_{kin} is conserved and the magnetic moment μ is an adiabatic invariant:

$$E_{kin} = E_\perp + E_\parallel = \frac{1}{2}mv_\perp^2 + \frac{1}{2}mv_\parallel^2 \tag{3}$$

$$\mu = \frac{mv_\perp^2}{2B} \tag{4}$$

When a charged particle moves on its helical trajectory towards a region with increasing magnetic field strength, its perpendicular velocity increases because of the adiabatic invariance of the magnetic moment. Due to the conservation of the kinetic energy the parallel velocity decreases accordingly. In other words, energy is transferred from $E_\parallel$ to $E_\perp$ when approaching higher magnetic fields. If the velocity (or energy) contribution parallel to the magnetic field lines vanishes, the particle is reflected. As the magnetic moment is a conserved quantity, we have, in a static magnetic field:

$$\frac{mv^2\sin^2(\alpha)}{2B} = \frac{mv^2\sin^2(\alpha_0)}{2B_{min}} \tag{5}$$

with α_0 and B_{min} being the pitch angle and the magnetic field intensity in the center of the bottle. α and B are the corresponding values at any coaxial position. The tangent of the pitch angle α is defined as the ratio of both velocity contributions (see figure 1):

$$\tan(\alpha) = \frac{v_\perp}{v_\parallel} \tag{6}$$

The axial position with the highest magnetic flux density, B_{max}, defines the latest-possible plane in which reflection can occur. From equation 6 one can conclude that in the event of a reflection ($v_\parallel = 0$) the pitch angle is $\alpha = \frac{\pi}{2}$. Formula 5 then yields:

$$\frac{\sin^2\alpha(z)}{B(z)} = \frac{\sin^2(\alpha_0)}{B_{min}} \tag{7}$$

Therefore:

$$\frac{1}{B_{max}} = \frac{\sin^2(\alpha_0)}{B_{min}} \tag{8}$$

and:

$$\alpha_0 = \sin^{-1}[(B_{min}/B_{max})^{\frac{1}{2}}] \tag{9}$$

This means that particles having a pitch angle greater than α_0 at the center of the bottle are trapped inside the magnetic bottle. The so-called "loss cone" is defined as a cone of half-angle α_0 with its vertex in the center of the magnetic bottle (see figure 1). Particles that have a velocity vector with a pitch angle falling inside the loss cone are not trapped. It is obvious (see formula 9) that the magnetic mirror ratio $R_m = B_{max}/B_{min}$ is a crucial parameter for the confinement of the plasma. In most ECR ion sources the mirror ratios at the injection and the extraction differ. Often, the magnetic flux density at the injection is higher compared to the extraction. This results in an increased particle flux of lost particles towards the extraction which is beneficial for the performance of the source as more ions can be extracted. It was stated before, that the ions are too collisional to be confined by the magnetic fields. Nevertheless, as the tendency of the electron population to approach the extraction is increased, also the ions that are electrostatically connected to the electrons are shifted towards the extraction. Usually, the magnetic mirror ratios are chosen according to R. Gellers semi-empirical scaling laws [1]. In general it can be stated that higher mirror ratios improve the plasma confinement and shift the charge state distribution (CSD) to higher average charges as the loss rates of the warm and hot electrons are reduced significantly [20].

Radial magnetic confinement

The confinement of the plasma is improved in radial direction by the use of a multipole magnet system. Most of the high-performance ion sources use hexapolar magnetic fields for that purpose (see figure 2). This leads to a radially increasing magnetic flux density with magnetic isobars of circular geometry. This so-called radial "cusp field" increases the stability of the plasma against MHD instabilities: The kinetic pressure of the particles in the plasma can be expressed according to the kinetic theory as:

$$P_{kin} = n_e k_B T_e + n_i k_B T_i \tag{10}$$

with P_{kin} being the kinetic pressure, k_B the Boltzmann constant, and n and T being the particular particle densities and temperatures of the ions and electrons, respectively. The kinetic pressure gradient would cause the plasma to expand/diffuse radially. Therefore, a radially increasing magnetic flux density evoked by the superposed magnetic multipole counteracts this diffusion by applying a magnetic pressure in the direction transverse to the field:

$$P_{mag} = \frac{B^2}{2\mu_0} \tag{11}$$

with B being the magnetic flux density and μ_0 the permeability. Thus, the magnetic pressure strongly increases with increasing radial distance effectively reducing

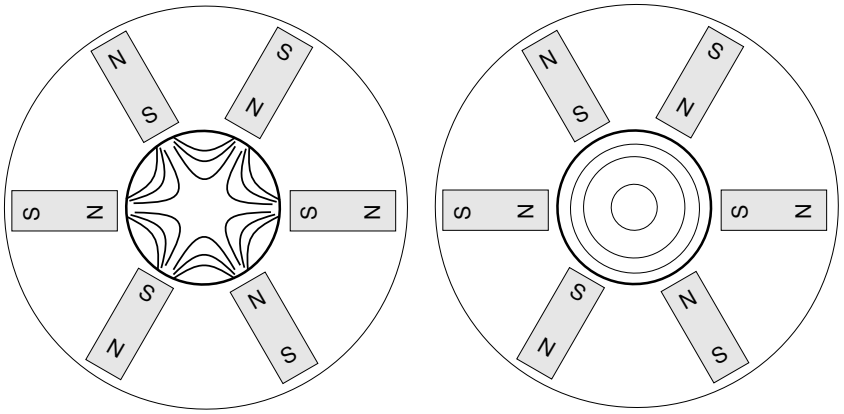

Figure 2: Left: magnetic field lines in the middle plane of a hexapole; Right: corresponding magnetic isobars. After [1].

the radial plasma escape. The ratio of both pressures is defined as the plasma β which is accordingly given as:

$$\beta = \frac{P_{kin}}{P_{mag}} = \frac{2\mu_0(n_e k_B T_{e\perp} + n_i k_B T_{i\perp})}{B_{ext}^2} \tag{12}$$

Here, only the kinetic pressure transverse to the field is relevant (as indicated in the formula by a "$\perp$"). Due to equilibrium conditions the magnetic field referred to in formula 12 is defined by the external magnetic field close to the surrounding chamber walls. As the kinetic pressure in ECR ion sources is far lower than the magnetic pressure the plasma β is usually $\ll 1$ [21].

2.2 ECR HEATING (ECRH)

For ion beams of low emittance it is beneficial to keep the ions at temperatures as low as possible [1]. Thus, a selective heating of the electrons of the plasma is desired (and achieved) in ECR ion sources. As described above, the electrons trapped in the axial magnetic bottle gyrate around the field lines at cyclotron frequencies depending on the local magnetic field strength (see formula 2). The circular motion of charged particles in magnetic fields carries a sign corresponding to the charge q that indicates the sense of the particle's rotation around the magnetic field lines: the electron gyro-motion is right-handed while for ions it is left-handed. Thus, to have the electro-magnetic wave gyrating in the same direction as the electrons a right-hand polarized wave is required. The frequency ω_{RF} of the injected wave has to equal the gyro-frequency ω_c of the electrons, which defines the resonance condition:

$$\omega_{RF} = \omega_c \tag{13}$$

Then, an extremely efficient, resonant energy transfer from the coaxially propagating microwaves (RF-waves) to the electrons of the plasma is achieved. The electrons are accelerated by the resonant electric field of the wave [20]. This heating mechanism is called ECR heating (ECRH) and can only occur in regions with the

appropriate magnetic flux density B_{res} (see formula 2). All the energy required to ignite and sustain ECR plasmas is transported there by the incident waves [1] and transferred exclusively to the electrons of the plasma [20].

In conventional ECR ion sources the frequency of the injected RF-wave is adapted to the magnetic flux densities close to the center of the source. Then, the ECR condition is met on a closed ellipsoidal surface (with magnetic field strength B_{res}) around the center. Close to that surface (with $B_{min} < B_{res} < B_{max}$) the electrons cyclotron motion is resonant with the injected microwaves.

The collective phenomena induced by the interaction of the electro-magnetic wave with the plasma are still the subject of investigations. As the wave creates/sustains the plasma, the plasma in turn influences the properties of the wave in a self-consistent manner. A commonly accepted model to describe the heating of the plasma is called "stochastic heating": Each passage through the resonance zone (with magnetic field strength B_{res}) changes the perpendicular energy of an electron (gain or loss) depending on the gyro-phase angle of the electron relative to the wave field. The particle performs a random walk in energy. However, the energy gain averaged over a random phase angle is always positive and proportional to the wave energy density $|E|^2$ and the time spent in the resonant region [1]. This results in a time-averaged heating. It was found that this heating mechanism is most efficient for the cold and warm electrons [22] with the corresponding energies mentioned in section 2.5. The product of the electron density n_e and their energy E_e scales with the frequency of the wave [20] (corrected for relativistic effects):

$$n_e E_e = \frac{\epsilon_0 \gamma m_{e0} \omega_{RF}^2}{e^2} (\gamma m_{e0} c^2) \tag{14}$$

with ϵ_0 the permittivity of free space, γ the Lorentz factor, c the speed of light, m_{e0} the rest mass of the electron, e the electron's charge, and ω the frequency of the wave. Therefore, with increasing frequency of the injected RF-wave the electron density and energy both increase. This is a widely-desired achievement as this shifts the charge state distribution (CSD) to higher charge states and increases the extractable currents due to an increase of the plasma density. However, there is an upper energy barrier that limits the kinetic energy an electron can attain during ECRH in a mirror field. The limitations appear due to the relativistic change in the electron's mass at high velocities (see formula 14). Also, the interactions of the hot electrons are more linked to the magnetic fields of the propagating waves than to the electric fields. The interactions with the magnetic fields often lead to a scattering of the hot electrons into the loss cone [22].

The ions are not heated by the RF-wave as their higher masses result in much lower Larmor-frequencies (see formula 2). Therefore, the ions do not gyrate in resonance with the injected wave. Moreover, as their charge is positive, the ions gyrate in the opposite direction, thus inhibiting resonance.

2.3 COLLISIONS

The basic interaction mechanisms among the particles of a plasma are collisions. In contrast to the theory applied for ordinary gases, in a plasma the interac-

tions between the various charged particles are dominated by the long-distance Coulomb forces instead of discrete collisions. Energy and momentum of the related particles are exchanged mostly by a large number of distant Coulomb encounters rather than by a few close collisions. Therefore, the change in the particle's energy and momentum is much more gradual than sudden. The change of a particle's propagation direction and its velocity can be described as a random walk with a small step size. As a consequence, the single small-angle scattering induced by the Coulomb forces is not so much of interest. The focus lies much more on a sufficiently high number of these small-angle scatterings that in sum provoke a deflection of the tracked particle of about 90°. These summed-up long-distance Coulomb encounters are called "Spitzer collisions" [1]. In that reference it is pointed out that large-angle deflections via multiple small-angle collisions are about two orders of magnitude more probable than such deflections via a single large-angle collision. Though the Coulomb forces in general show a comparatively large range of influence, their effective coverage inside a plasma is strongly limited by the screening abilities of plasmas regarding electric fields. The corresponding mechanism is called "Debye screening". It describes the damping of electric fields and it is caused by the presence of mobile charge carriers. The mobility of these charge carriers allows the charges to rearrange and to compensate for local electric fields. The Debye length is defined as the distance that is required under given plasma parameters to damp the field of a local electric charge to $\frac{1}{e}$ of its original value. The Debye-length in a plasma is given as:

$$\lambda_D = \sqrt{\frac{\epsilon_0 k_B T_e}{n_e e^2}} \tag{15}$$

This expression is only valid if the mobility of ions is negligible compared to the timescales of the processes involved. In ECR plasmas with their cold (and massive) ions this assumption can be regarded as true [1]. The Debye length is the upper distance limit for Coulomb interactions inside a plasma. The corresponding lower limit is the classical distance of closest approach:

$$b_{min} = \frac{2e^2}{mv^2} \tag{16}$$

with m the mass of the scattered particle, and v its velocity [1]. Starting from these assumptions one can derive a set of formulas to estimate (on average) the timescales for the collisions and the transfer of energy and momentum. As mentioned above, the small-angle deflections are the main scattering processes among the charged particles in a plasma. Therefore, to describe the coherent processes with larger timescales, the concept of collision times is withdrawn and replaced by the so-called "relaxation times" τ. In the terminology also the expression "collision time" is sometimes used though it is referred to relaxation times. In general, the relaxation times characterize typical durations needed to thermalize the momentum or energy, or to deflect a particle by 90°, respectively, as a result of the already mentioned random walk processes [2]. These times can be given for the same kind of particles (e.g. electrons) at different energies or even

for different kinds of interacting particles (e.g. electrons and ions). In reference [2], the relaxation times for 90°-deflections are given as:

$$\tau^{ee} = \left(\frac{4\pi\epsilon_0}{e^2}\right)^2 \frac{3\sqrt{3m_e}T_e^{3/2}}{8\pi n_e \ln\Lambda} \approx 1.4\times10^{10}\frac{T_e^{3/2}}{n_e} \tag{17}$$

$$\tau^{ei}\left(\frac{4\pi\epsilon_0}{e^2}\right)^2 \frac{3\sqrt{3m_e}T_e^{3/2}}{4\pi Z_i^2 n_i \ln\Lambda} \approx 2.8\times10^{10}\frac{T_e^{3/2}}{Z_i^2 n_i} \tag{18}$$

$$\tau^{ii} \approx \left(\frac{4\pi\epsilon_0}{e^2}\right)^2 \frac{3\sqrt{3m_i}T_i^{3/2}}{8\pi Z_i^4 n_i \ln\Lambda} \approx 6\times10^{11}\frac{A_i^{1/2}T_i^{3/2}}{Z_i^4 n_i} \tag{19}$$

differentiating between electron-electron (ee), electron-ion (ei), and ion-ion (ii) deflections. The ion density (in m^{-3}) is represented by n_i. Z_i and A_i are the charge state and the mass number of the ions, respectively. The particular temperatures T need to be given in eV. Then the resulting relaxation times correspond to seconds. The term $\ln[\Lambda]$ is the so-called Coulomb logarithm. It is given by the ratio $\ln[\Lambda] = \lambda_D/b$ with λ_D the Debye-length and b the classical distance of closest approach as defined above. The Coulomb logarithm is quasi insensitive to the plasma parameters and usually lies in the range between 10 and 20 in ECR plasmas [1].

Evaluating formulas 17 to 18 one can conclude that the 90°-deflection times for the electron-electron and electron-ion encounters do not differ significantly and it is $\tau^{ee} \approx \tau^{ei}$ [1]. At this point one could assume that the ions can be heated by the electrons. To estimate that, the corresponding relaxation times for energy transfer (or thermalization) need to be considered. The relaxation times for energy transfer can be found from the collision kinematics (conservation of energy and momentum) and are given in [2]:

$$\tau_E^{ee} \approx \left(\frac{4\pi\epsilon_0}{e^2}\right)^2 \frac{3\sqrt{m_e}T_e^{3/2}}{4\sqrt{\pi}n_e \ln\Lambda_e} \approx 2.9\times10^{10}\frac{T_e^{3/2}}{n_e} \tag{20}$$

$$\tau_E^{ei} \approx \left(\frac{4\pi\epsilon_0}{e^2}\right)^2 \frac{3m_i T_e^{3/2}}{8Z_i^2\sqrt{2\pi m_e}n_i \ln\Lambda_i} \approx 1.9\times10^{13}\frac{A_i T_e^{3/2}}{Z_i^2 n_i} \tag{21}$$

$$\tau_E^{ii} \approx \left(\frac{4\pi\epsilon_0}{e^2}\right)^2 \frac{3\sqrt{m_i}T_i^{3/2}}{4Z_i^4\sqrt{\pi}n_i \ln\Lambda_i} \approx 1.2\times10^{12}\frac{A_i^{1/2}T_i^{3/2}}{Z_i^4 n_i} \tag{22}$$

It is obvious that the relaxation times for energy thermalization do indeed differ. The electron-electron thermalization is the fastest and resembles the corresponding 90°-deflection time:

$$\tau_E^{ee} \approx \tau^{ee} \tag{23}$$

But the electron-ion- and ion-ion-thermalizations take significantly longer. The main reason is found in the mass-ratios. If one relates the particular energy thermalization times τ_E to τ^{ee} one finds as a first estimate for the ion-ion-process (neglecting the particle densities and the ion charge state)

$$\tau_E^{ii} \sim \left(\frac{m_i}{m_e}\right)^{1/2}\tau^{ee} \tag{24}$$

and even

$$\tau_E^{ei} \sim \frac{m_i}{m_e}\tau^{ee} \tag{25}$$

for the corresponding electron-ion process. From these findings one can conclude that the electrons of the plasma can thermalize much faster than the other particle species. However, it is observed in experiments that the electron population does not follow a single but rather three Maxwellian distributions. Therefore, the electrons are not thermalized. To explain this observation the relaxation frequency needs to be introduced. In that context and for the sake of completeness some additional parameters to describe the particle kinetics in a plasma are presented here:

The definition of the mean-free-path length λ is in analogy to the kinetic theory:

$$\lambda = \frac{1}{n\sigma} \tag{26}$$

with n the appropriate particle density and σ the cross-section for that process. The relaxation time τ is related to the mean-free-path length λ, the cross-section σ, the particle density n, and the mean particle velocity, v, by:

$$\tau = \frac{\lambda}{v} = \frac{1}{n\sigma v} \tag{27}$$

with the relaxation frequency being the reciprocal of the relaxation time:

$$\nu = \frac{1}{\tau} = n\sigma v \tag{28}$$

Accordingly, we have

$$\nu^{ee} = \frac{1}{\tau^{ee}} \approx \frac{1}{\tau_E^{ee}} \ll \omega_c \tag{29}$$

Therefore, as ω_c is usually in the range of several to multiple GHz, the heating of the electrons by the incident waves happens on shorter timescales than the collisions and/or the energy equipartition (i.e. thermalization). This explains why one observes non-thermalized electron-populations in ECR plasmas. Also, since $\nu^{ee} \ll \omega_c$, the plasma is characterized as collisionless. As the typical times needed to thermalize the ions are even longer, the ions stay cold which is a desired property for the extraction of low-emittance ion-beams [1]. However, as the energy relaxation time for ion-ion interactions also depends on $T_i^{-3/2}$ and on the charge states of the ions (the ions in ECR plasmas are cold, in the eV-domain, and highly charged), the efficiency of ii-thermalization is high enough to result in well-thermalized ions in ECR plasmas [1]. This, however, is only possible, if the ions are confined longer than τ_E^{ii}.

2.4 IONIZATION AND CHARGE EXCHANGE

Ionization and charge exchange are the results of particle collisions (in general also called "interactions") inside the plasma. However, only inelastic collisions can lead to both processes as in elastic collisions the internal states of the involved particles are not allowed to change. This is founded in the conservation of the kinetic

energy in elastic collisions. Consequently, in inelastic collisions the internal states of the particles involved are indeed allowed to change and these collisions can lead to excitation, ionization, and recombination. The last two of the mentioned processes are important parameters for plasma formation, maintenance, and source performance, and will be briefly presented within this section.

In ECR plasmas the main ionization process is electron impact ionization [1, 20]. To strip an orbital electron from an atom or an ion by electron impact the primary electron needs to have a minimum kinetic energy E_e which is defined by the binding energy W of the corresponding electron. If the energy of the impinging primary electron is below that value that particular electron cannot be removed from the nucleus. In that case the target can be excited and potential outer electrons with accordingly lower binding energies may be expelled instead. The ionization potentials Φ_i (which correspond to the binding energies via $W = e\Phi_i$) for all the elements at all charge states were calculated and published in [23] and can be found as a graphical presentation in [21]. The error compared to experimental data is said to be only about 5%. It also was found in experiments that the probability to remove an electron with ionization potential Φ_i is at maximum when the energy of the primary electron is about 3 to 4 times Φ_i [1, 21]. At still increasing energies of the primary electron the ionization probability (which can be expressed by the ionization cross section) decreases gradually [1, 21]. Semi-empirical formulas to calculate the cross sections fitted to experimental data have been presented by [24] and [25].

Induced by the impact of an energetic electron there exist several ionization processes among which the so-called stepwise ionization is the by far most probable and therefore dominant [1, 20]. It can be described with the following formula:

$$e^- + A^{n+} \rightarrow A^{n+1} + 2e^- \tag{30}$$

An electron interacting with an atom or an ion results (in the case of ionization) in an increase by one of the charge state of the heavy particle and an additional electron. As a consequence, at each ionization process more free electrons are created and the discharge grows. After the ionization the primary electron carries the main part of the residual energy E_{res} of that reaction: $E_{res} \lesssim E_e - W$. It also tends to conserve its initial direction. In contrast, the secondary electron emitted from the nucleus is comparatively cold and its direction of emission follows an isotropic distribution [1]. They serve to replenish the reservoir of cold electrons. This implies that to maintain the plasma, power has to be coupled into the discharge at a rate sufficient to compensate for the energy loss of the electrons caused by the ionizing collisions.

But it is not only the energy of the electrons that needs to be adapted to the desired charge state of the particular element, it is also the confinement time of the ions that is required to be appropriate: The electrons need to have enough time to (mainly stepwise) ionize the ions. The corresponding confinement times $\tau_i(Q)$ needed for the creation of an ion of charge state Q from a neutral atom can be calculated with the following formula [21]:

$$\tau_i(Q) = \sum_{k=0}^{Q-1} \frac{1}{n_e \langle \sigma_{k,k+1} v_e \rangle} \tag{31}$$

Again, n_e and v_e describe the density and the velocity of the electrons, respectively. The term $\sigma_{k,k+1}$ characterizes the cross section for the ionization from charge state k to k+1. As mentioned above, proper values of the particular cross section σ for all the elements and charge states can be found in the literature. Thus, the denominator of equation 31 represents the frequency at which each ionization step occurs. The average indicated by the angle bracket is taken over the distribution of the electron velocities. All together, the sum of the inverses of the ionization frequencies yields the time to create an ion of charge state Q by successive electron impact and stepwise ionization. It is obvious that the combination of both parameters, the plasma electron density times the confinement time $n_e\tau_i$ is a crucial parameter to adjust for a good performance [21].

The emission of multiple electrons can be induced by one primary electron via Auger- or shake-off ionization. As these processes are by far less probable they only shall be mentioned in this context. A comprehensive description is for example given in [1].

Charge exchange on the other hand is besides a bad confinement or non-appropriate electron temperatures a process that may strongly decrease the performance of a source regarding high charge states. The reaction for charge exchange can be expressed as:

$$A^{n+} + B^{m+} \rightarrow A^{(n-1)+} + B^{(m+1)+} \quad \text{with} \quad n > m \tag{32}$$

In the reaction described above, an electron is transferred from particle B to particle A which corresponds to a decrease of the charge state of the higher-charged ion. The cross sections of highly-charged ions to incorporate an electron from a low-charged or neutral particle are usually extremely high. Typical charge exchange cross sections are 3-4 orders of magnitude larger than the corresponding electron impact cross sections. Fortunately, the reaction rates are proportional to the velocities of the particular projectiles. This is valid for the charge exchange cross sections as well as for the ionization cross sections. As the neutral atoms and also the ions of the plasma are cold, their reaction rates among each other are low while they strongly increase for the warm and hot electrons. In addition, to minimize the effect of charge exchange reactions the density of neutral atoms (with the highest cross section to donate electrons) should be at least two orders of magnitude lower than the electron density [1, 21]. Therefore, ECR plasmas are typically operated at low pressures p with $p < 10^{-5}$mbar.

2.5 CONCLUSIONS: IMPACTS ON THE ECR PLASMA

The ECRH mechanism is a very efficient way to selectively heat the electrons of the plasma. The energy gain of the electrons imparted by the RF-waves is perpendicular with respect to the magnetic field lines [20]. This has a positive influence on the pitch angle distribution and thus on the confinement as well, as the perpendicular velocity component increases significantly. From that point of view the confinement of the electrons increases with increasing energy, and the resulting velocity contributions $v_{\parallel}$ and $v_{\perp}$ are very anisotropic. This characteristic

is very beneficial for the production of highly-charged ions (HCIs) [26] as the electrons can gain high energies and are well confined.

As the collision-frequencies of the electrons are small compared to the injected RF-frequency ($\nu^{ee} \ll \omega_c$), the electrons are not able to thermalize. As a result, the electrons do not follow a single Maxwellian temperature distribution. Their energy distribution can rather be fitted by the superposition of three Maxwellians (cold, warm, and hot) [27]: The hot electrons ($E_{kin} \gtrsim 10keV$) can be regarded as collisionless [28], and therefore as well confined in the magnetic mirror. They are commonly assumed to populate the center of the source, and to establish there a negative potential dip that enhances the confinement times of the cold ions [1]. In this energy range scattering of the high-energy electrons mostly occurs due to interactions with the magnetic field component of the RF-wave [20, 22]. The warm electrons ($50eV \lesssim E_{kin} \lesssim 10keV$) are the main contributors for the ionization processes that establish and sustain the plasma. They suffer more frequent scattering collisions and are less well-confined. The cold electrons ($E_{kin} \lesssim 50eV$) that are emitted during the ionization processes (see section 2.4) or by sputtering hardly contribute to the ionization processes. They replenish the population of higher energy electrons via ECRH. The magnetic confinement of the cold electrons is poor [21, 28].

The highly collisional ions undergo ionizing collisions with the electrons and scattering Coulomb- or charge-exchange collisions with other ions and are therefore almost not magnetized [20]. The fact that the ions are strongly collisional leads to the conclusion that the ions indeed follow a Maxwellian temperature distribution [27]. Since the ions cannot be effectively heated by the energetic electrons due to their mass-ratio, the ions stay comparatively cold in the few eV-domian [27, 29]. Therefore, the ions are electrostatically confined by the magnetically well-confined warm and hot electrons.

However, there is one process in the plasma that somewhat counteracts this electrostatic confinement of the ions. It is caused by the poorly-confined cold electrons of the plasma. Due to their small mass compared to the ion's mass their velocities in the same thermal energy range are accordingly much higher. Thus, the flux of electrons that leaves the plasma is higher than that of the ions. This results in a net removal of negative charges from the plasma which is self-consistently balanced by the formation of a positive potential in the bulk of the plasma, the so-called "plasma potential", V_P [1]. The details of that process are discussed in section 3.2. As a consequence, this positive potential balances the low-energy electron losses, but in return weakens the confinement of the also positively-charged ions. Typical values for V_P lie in the region of a few tens of eV [30], depending on the operating conditions of the particular source.

3 ION EXTRACTION FROM ECR ION SOURCES

The properties of an ion beam extracted from an ECR ion source depend in principle on three major contributions which are the spatial distribution of the various ion species in the plasma volume and in particular close to the plasma electrode, the formation of the plasma meniscus where the ions are extracted from, and the influence of static magnetic and electric fields at the extraction region. The basic principles of all the three contributions will be discussed in this chapter.

3.1 SPATIAL DISTRIBUTION OF THE IONS

The spatial distribution of the various ion species in the source is determined by the geometry of the magnetic fields to a large extent. These magnetic structures define the regions of ECR heating and the regions of high electron density. To conserve charge neutrality, the ions are supposed in a first order approximation to be accordingly distributed. This seems a plausible assumption as the ions are created via electron impact which requires a close vicinity. As reported in [22], the magnetic isobars in such a configuration have been found to equal the isobars of the plasma. Thus, the static magnetic field influences the plasma density distribution in front of the extraction aperture, and the hexapolar cusp field leads to a strong plasma density variation in the azimuthal direction [21]. Also, from that information (magnetic isobars $\widehat{=}$ plasma isobars) the plasma loss regions can be deduced: Along those magnetic field lines that cross the walls of the plasma chamber the particles of the plasma can be lost. As a consequence of the magnetic field geometry of the hexapolar radial field superimposed on the axial magnetic mirror, the plasma and its loss regions establish characteristic, triangular-shaped distributions at both ends of the plasma chamber. They are observed as sputter or deposition marks in all sources with hexapolar radial confinement. In addition, the spatial distribution of the particles is also influenced by diffusion and collisions. However, detailed information about the spatial distribution of the ions in the plasma, resolving the different ion species and charge states, has so far only been given as the results of sophisticated computer simulations (see chapter 8) and in this work when limiting to the plane of the plasma electrode and to selected charge states.

3.2 PLASMA POTENTIAL AND SHEATH FORMATION

The basics of the plasma potential and the mechanism of sheath formation gathered in this section are needed for the further studies presented in the next section. The processes of potential and sheath formation in a plasma are triggered when the plasma is disturbed. This disturbance can be evoked by exposing the plasma to an external metallic boundary. This situation is closely related to the operation

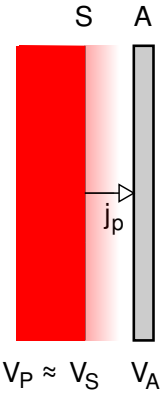

Figure 3: Schematic drawing of a plasma exposed to a planar boundary A at potential V_A. S represents an equipotential surface in close vicinity of the external boundary. The corresponding potentials of the surface S (V_S) and the bulk plasma (V_P) are alike. j_p is the transfered current density. After [1].

of ECR ion sources as in these sources the plasma is nearly entirely surrounded by a metallic plasma chamber. The potential of the boundary is defined as V_A in the following discussion. The resulting potentials inside the plasma are always related to this boundary and therefore to V_A. Only in figure 4, this potential is referred to as V_{FL}, as it is convenient in this context to use the expression "floating potential". In the case of a plasma fully enclosed by metallic boundaries as described above, both potentials are equivalent ($V_{FL} = V_A$).

The interactions of the plasma with the surroundings occur in axial and radial direction. Usually, the interferences are stronger in the axial direction which is founded in the positioning of the biased disc and the plasma electrode close to or even inside the axial magnetic mirror configuration. Nevertheless, the exact symmetry of the source is discarded in the following argumentation and simplified to a planar problem which is an adequate first order approximation [1]. A sketch of the problem is displayed in figure 3.

In a plasma which interferes with a boundary, a sheath (see figure 4) will establish between the boundary and the plasma. The formation of this sheath is mainly caused by the higher velocities of the electrons compared to the ions with the ratio given as:

$$\frac{v_e}{v_i} \sim \sqrt{\frac{T_e m_i}{T_i m_e}} \tag{33}$$

Thus, the electrons are more efficient to leave the plasma, and charge is effectively transfered from the bulk plasma to the boundaries (i.e. the plasma chamber walls). As a consequence, in the bulk plasma a positive potential (the plasma potential V_P) establishes with respect to the potential V_A (V_{FL} in figure 4) of the chamber walls. This potential balances the electron losses to the ion losses. In the equilibrium state the charge losses of both polarities occur at the same rate and the sheath turns into a region of positive space charge shielding the neutral bulk plasma from the potential distortion induced by the walls [31]. Under "normal" conditions of disturbance (the plasma interferes with a planar boundary of uniform potential), the length of this sheath is determined by the plasma parameters and given as the

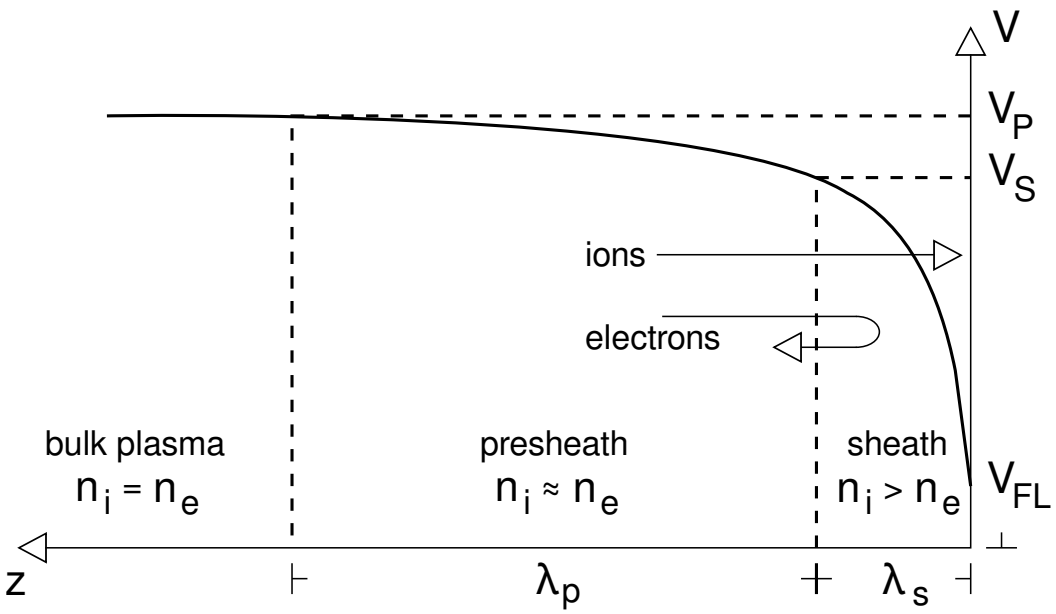

Figure 4: Distribution of the potential across the various sheaths in the vicinity of a boundary interacting with the plasma. After [2].

Debye length λ_D (see formula 15). As will be pointed out in the next section, the length of that sheath can be modified when external voltages are locally applied. Therefore, a more general term is used and the sheath is named λ_s in figure 4. When entering the sheath from the plasma (or more accurately from the presheath that will be introduced now), the electric potential gradient becomes very steep. The curvature of the potential causes the electrons to be repelled from and ions to be accelerated towards the outer walls [32] as schematically shown in figure 4. Accordingly, the density gradient of the electrons is by far steeper when entering the sheath than that of the ions [2]. Langmuir postulated that ions enter those regions of a plasma that are dominated by density perturbations, with a directed velocity [33]. Bohm found (as described in detail in [31]) that their velocity then needs to exceed the ion speed of sound c_{si}. This inequality is referred to as the Bohm criterion [32]:

$$v_i \geq c_{si} = \sqrt{\frac{k_B T_e}{m_i}} \tag{34}$$

For $T_e \gg T_i$ (which is always true in ECRIS) the ion sound speed depends on the electron temperature rather than on the ion temperature [32]. As the ions need to hold velocities higher than or equal to the ion speed of sound already when entering the sheath, an adequate acceleration process needs to take place prior to entering. From that necessity the presence of a second sheath, the so-called presheath (see figure 4) was derived. This presheath separates the bulk of the plasma from the sheath. The potential drop through the presheath needs to be high enough for the ions to attain velocities to fulfill the requirements of the Bohm

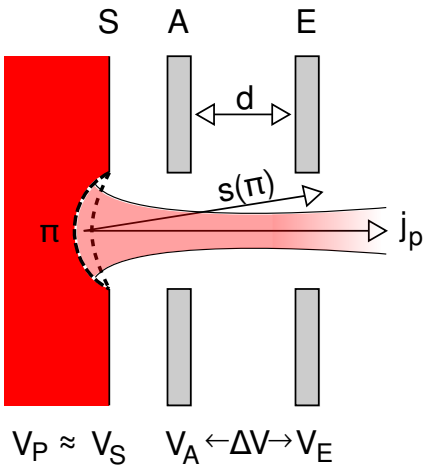

Figure 5: Schematic drawing of the simplest extractor system. S illustrates the boundary-closest equipotential surface with $V_S \approx V_P$. π is the plasma meniscus where the ions are effectively extracted from. A and E represent the plasma electrode and the extraction electrode. The corresponding voltages are denoted below. j_p is the extracted current density. After [1].

criterion [31]. For singly-charged ions the energy balance can be expressed as a function of the potential drop through the presheath [2]:

$$e(V_P - V_S) \geq \frac{1}{2} m_i c_{si}^2 \tag{35}$$

In summary, in the regions where a plasma interacts with its surroundings a sheath and a presheath establish themselves. The main potential drop from the resulting bulk plasma potential V_P to the reference potential of the chamber walls V_A (V_{FL} in figure 4) occurs within the sheath and amounts to V_S, as presented in figure 4. The definition of the presheath originates from the need to satisfy the Bohm criterion. Therefore, the potential drop through the presheath $V_P - V_S$ is just high enough to adequately accelerate the ions and is therefore distinctly lower than that in the sheath. In the presheath the deviations from the potential and the particle densities as present in the bulk plasma are small and vanish over the distance λ_p when further approaching the bulk plasma. These processes of plasma potential and sheath formation are further elaborated in the next section to derive the plasma meniscus, a key property for the extraction of ions from the ECRIS.

3.3 PARTICLE EXTRACTION FROM THE PLASMA MENISCUS

The plasma meniscus corresponds to that equipotential surface of the plasma where the ions are effectively extracted from. Its curvature has a major influence on the extracted ion beam. Therefore, this section will address the formation mechanisms of the meniscus and explain the physical correlations. The simplified situation presented in figure 3 is now adapted to describe the still simplified extraction system presented in figure 5. The basics of this principle are applied in all ECR ion sources to form and extract the ion beam.

The evaluations so far have been made for planar boundaries of uniform potential. Hence, the geometries of the resulting sheath and presheath are planar and the sheath has a length of λ_D. If now a spatially limited area of the still planar boundaries is biased to a different voltage, the length of the sheath λ_s (refer to figure 4) covering this area is not solely determined by the plasma parameters as λ_D is, but scales with the square-root of the applied potential V_{ext} (and the inverse of the square-root of the electron temperature T_e) according to [1, 21]:

$$\lambda_s \sim \lambda_D \sqrt{\frac{eV_{ext}}{k_b T_e}} \tag{36}$$

This situation in principle equals that presented in figure 5 displaying the simplest extractor system. Here, the planar boundary is pierced to imitate the plasma electrode terminating the plasma chamber in the downstream direction. That electrode A at potential V_A is electrically connected to the plasma chamber and separates the plasma from the subsequent beam line. A second pierced electrode, the extraction electrode, E, at potential V_E, is placed further downstream at a distance d from the plasma electrode. In analogy to an operating ECR ion source the plasma chamber and the plasma electrode are biased to a high positive voltage, V_A, relative to the extraction electrode. The electric potential of the lower-biased electrode E is mostly screened from the plasma by the solid plasma electrode A and the plasma chamber. However, due to the aperture in the plasma electrode the potential is not totally screened but reaches the plasma at its radial center. As a consequence, in this radially central region of the plasma, the length of the sheath λ_s adopts accordingly to screen the locally deviated electric field from the neutral plasma bulk. As already discussed, the major part of the plasma potential drops through the sheath λ_s to the potential of the boundaries. Therefore, one can assume that the potential at the edge of the sheath (where the presheath switches over to the sheath) is approximately at the same potential as the bulk plasma: $V_P \approx V_S$. That equipotential surface (with $V_P \approx V_S$) that is closest to the plasma electrode is marked as S in figure 5. As the electric field of the extraction electrode reaches inside the plasma chamber, the previously planar equipotential surface S is deformed accordingly in its central part. This deformation of S is called the plasma meniscus π (see figure 5), the location from which the ions are extracted [1]. The position and shape of S depend on all the parameters of the discharge, the extraction voltage and the exact geometry of the extraction electrodes. The shape and the position of the plasma meniscus can be approximated by the following formula [1]:

$$s(\pi) = \frac{2}{3}\epsilon_0 \left(\frac{2q}{m_i}\right)^{1/4} \frac{(\Delta V)^{3/4}}{j_p^{1/2}} (1 + \epsilon(\pi))^{1/2} \tag{37}$$

Here, s describes the distance between the extraction electrode E and the points of the plasma meniscus. ΔV is the voltage difference between both electrodes (it is assumed that $V_S - V_A \ll V_A - V_E = \Delta V$) and $\epsilon(\pi)$ is a correction factor that takes the shape of the electrode itself into account. The initial ion energy distribution is not considered. j_p is the current density of the extracted beam that in the close vicinity of the extraction hole also can be expressed as [1]

$$j_p = q n_i^+ \overline{v}_i = j_{sc} \tag{38}$$

where n_i^+ denotes the ion density and $\overline{v}_i$ the mean velocity of the ions crossing the sheath. v_i is given by the Bohm criterion (see formula 34). j_{sc} represents the space-charge-limited current that is given by the Child-Langmuir law [1] with V_E the extraction voltage:

$$j_{sc} = \frac{4}{9}\epsilon_0\sqrt{\frac{2q}{m_i}}\frac{V_E^{3/2}}{d^2} \tag{39}$$

This formula yields the maximum extractable current under space-charge limited conditions. In other words, the source is capable of producing more ions than can be removed at any time. The limitations concerning the amount of extractable currents are caused by the resulting space charge that a beam of positively charged ions establishes.

In practice, the curvature of the plasma meniscus is modified by adapting the extraction voltage and/or the distance between the electrodes to the plasma parameters (mainly the ion density n_i^+) inside the source. Therewith, the properties of the extracted ion beam are matched to the subsequent beam line. For the beam optics it is favorable if the plasma meniscus is concave to a certain extent. Then, the extracted ion beam is convergent an can pass through the hole of the extraction electrode [1]. As the extraction of the particles is evoked by electrostatic acceleration, in principle all the ions passing the sheath can be extracted. Electrons coming from the source are reflected if their velocity in longitudinal direction is too low to overcome the potential barrier.

Inside the plasma the electric fields are effectively screened and the spatial distribution of the charged particles is mainly determined by the magnetic fields. Both processes have been discussed in the previous sections. When the ions are extracted from the plasma, the potential-screening effects vanishes and both, electric and magnetic fields have to be considered for the ion trajectories.

NEXT REFERRED PUBLICATION: OWN CONTRIBUTION: approx. 80%

DIRECT HIGH-RESOLUTION ION BEAM-PROFILE IMAGING USING A POSITION-SENSITIVE FARADAY CUP ARRAY Lauri Panitzsch, Michael Stalder, and Robert F. Wimmer-Schweingruber, Rev. Sci. Instrum. 80, 113302 (2009), DOI:10.1063/1.3246787

MEASURING TECHNIQUE AND POSITION OF DATA ACQUISITION:

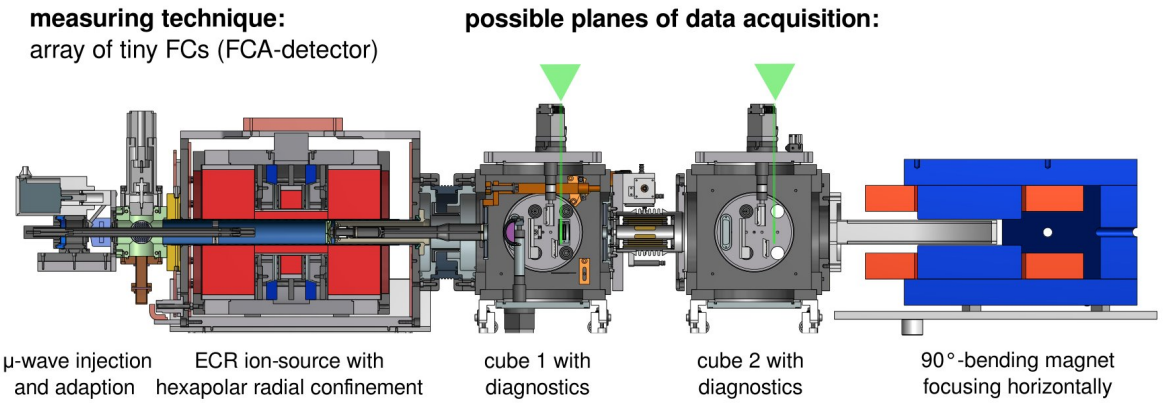

MOTIVATION:

Conventional ion-beam profile-monitors offer some useful features but they also show some critical limitations. When regarding scintillation screens these critical limitations include the detector's durability and the linearity of the signal (which is the luminescence of the screen not yielding quantitative results for the current distributions). Wire harps on the other hand show very limited and ambiguous spatial resolution. To face these limitations the well-proven technique of FC-measurements was developed further: A total of 44 tiny FCs is arranged in a grid. This grid is driven through the ion beam while acquiring the beam currents impinging into the different cups. The developed detector (the FCA) presented in the following publication has proven its reliability and performance during several published and non-published tests and measurements.
This new measuring system presented in the following paper played an important role during the investigations to determine the spatial distribution of various ion species ≈ 45 cm downstream from the extraction (the plane marked in green in cube 1 in the figure above, see publication 2 for details). The electronics were also used for the investigations described in publication 4 where the current density distribution inside the plasma chamber close to the plasma electrode was examined.

NEW DEVELOPMENTS:

A new technique for the detection of beam profiles has been developed. It offers high durability, high spatial resolution, and precise, absolute readings for the recorded current densities.

Direct high-resolution ion beam-profile imaging using a position-sensitive Faraday cup array

Lauri Panitzsch,[a] Michael Stalder, and Robert F. Wimmer-Schweingruber
Institute for Experimental and Applied Physics (IEAP), University of Kiel, Kiel 24118 Germany

(Received 17 July 2009; accepted 19 September 2009; published online 10 November 2009)

Ion sources have wide-spread use in a multitude of applications. For many, an accurate knowledge, or better, an accurate imaging, of the beam profile and intensity is an important criterion. We are developing an ion source to calibrate instruments for space-based measurements of solar wind and suprathermal particles in the energy range from below 1 keV/nuc to above 200 keV/nuc. In order to establish accurate beam profiles for calibration purposes, we have developed a new method based on an array of very small ($\varnothing$=0.3 mm) Faraday cups. Here, we describe the experimental setup and discuss how to achieve several requirements such as a large thermal load due to the ~40 W of beam power. © *2009 American Institute of Physics.* [doi:10.1063/1.3246787]

I. INTRODUCTION

The profile is one of the main parameters of an ion beam in many applications. Knowledge about the profile provides additional information about the position of the beam and the spatial and temporal distributions of the beam current. Two systems are in general use to monitor the beam profile, wire scanners and scintillation screens (e.g., Refs. 1–3). Both systems have proven their functionality and are chosen depending on the needs of the particular application. Their basic principles are well known and can be found, for example, in Ref. 4. Though they will not be discussed in detail within this paper, their advantages and disadvantages will be briefly mentioned. Residual gas monitors with segmented residual gas ion detecting plates as a third technique are based on a similar principle as wire scanners regarding the reconstruction of the profile from the measured data. Since they offer a worse resolution in position due to the space charge effect of the ion beam accelerating the residual gas ions radially away from the beam center and facing the same difficulties as wire scanners in profile reconstruction (discussed below), these detectors will not be further discussed within this paper either. Their basic principle can also be found in the reference mentioned above.

Scintillation screens on the other hand operate very fast and at very high resolution in position. They offer a convenient way to image the beam profile. The most sensitive screens are made of alkali halide crystals, but also other crystals (i.e., SiO_2) are used. Their functionality is based on (iono)luminescence.[5] In a limited range the intensity of the emitted spectrum is linearly proportional to the beam current density hitting the screen. If the beam current exceeds this range, the emitted intensity is saturated and proportionality is lost. Furthermore, changing the ion beam parameters influences the relative intensity of the (intrinsic and activated) luminescence.[5] Since the light yield also decreases with operational time, this method does not provide absolute values for the beam current. Also the lifetime of these kinds of detectors is strongly limited at higher beam powers. In such cases tantalum foils are used to illustrate the beam profile. Absorbing the beam power a profile-dependent heat-induced glow is visible. To minimize the structure-smoothening and image-broadening heat flux inside the foil, the foils are chosen to be very thin. Nevertheless, their resolution is distinctly lower than that of crystal based scintillators. More examples for this detection system can be found in Refs. 1 and 2, for example.

Wire scanners offer a quasi-non-destructive way to measure the profile in absolute current values. Their resolution and measuring speed generally behave antiproportional and depend on the number of wires used for detection and the analyzing electronics. To calculate a two-dimensional model of the beam profile from the measured data, an Abel inversion needs to be performed. Therefore, the data points have to be fitted to a function, and (axial or radial) symmetry has to be assumed. This may have a strong influence possibly falsifying the results. A reliable determination of the beam profile can only be achieved if the ion distribution in the beam is Gaussian-like or at least single-peaked with only moderate asymmetry. Problems occur if one unknowingly samples a hollow beam or a beam with more than one maximum in the current distribution. Figures 4 and 7 show two unusual but possible (and measured) beam profiles. Both could hardly be correctly inverted from data measured with the wire scanner method. Additional details about this detection system can be found in Refs. 3 and 6, for example.

To combine high-resolution profile measurements with the advantage of absolute current values, we have developed a new kind of detection system. It consists of an array of multiple tiny Faraday cups (FCs). This system allows direct beam profile measurements and offers independence of assumptions that could distort the results. In our first tests this system has proven to be fast and reliable while offering a sufficiently high resolution in position and current. In the following sections we will discuss this new kind of detector

[a]Electronic mail: panitzsch@physik.uni-kiel.de.

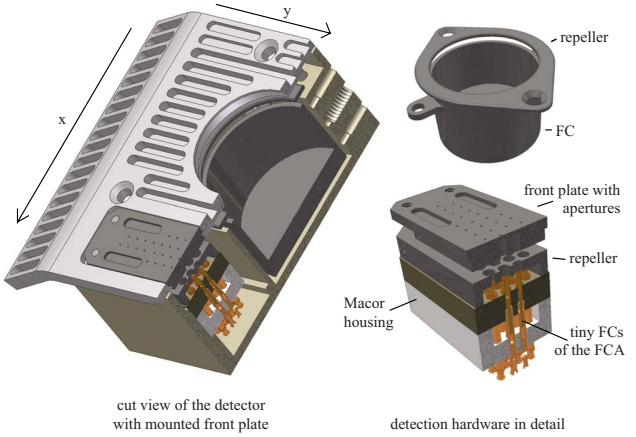

FIG. 1. (Color online) CAD-drawings of the detector system. Left: cut-view of the complete detector in the housing; right: FC and FCA in detail with part names.

in detail and show first beam profiles measured at the electron-cyclotron-resonance-ion-source of the solar wind laboratory being established in Kiel.

II. BASIC PRINCIPLE

The detector system we have developed uses the well known and established FC as the measuring principle. Incoming ions deposit their charge and energy in the cup, which is grounded via a sensitive amperemeter. The neutralizing current flowing to the cup directly equals the ion current hitting the cup as long as the created secondary electrons are efficiently prevented from leaving the cup by the use of a repeller on negative high voltage (secondary electron suppression). In most applications only one FC is used to measure the current without any resolution in position. To scan the profile, one needs–depending on the desired resolution–a certain amount of measuring points with certain diameter in a plane perpendicular to the beam line. Knowing their position and the current measured at each point, one can easily create the profile. This is the strategy we have pursued. A detailed explanation for two existing systems with distinctly lower resolution based on a similar principle can be found in Refs. 7 and 8.

III. DESIGN AND CONSTRUCTION

The FC array (FCA) is built of 44 small FCs arranged into an array of four rows with increased cup density in the center (see Fig. 1, lower right). Their effective scanning area is reduced by the use of apertures ($\varnothing$=0.3 mm each). This provides a high resolution in the center of the beam and a lower one in the outer regions. By moving this array through the beam, we are able to reach a total scanned area of about 45×30 mm^2 at a spatial resolution of 58×51 dpi. Because of the limited space we have decided to include a large FC with a diameter of 22.8 mm, which uses the same measuring electronics in the detector housing. This allows us to measure the total beam current at the same location along the beam. All 45 signals of the different cups are routed out of the vacuum using a standard SubD-50 UHV-feedthrough. Two of the remaining wires are used to provide high voltage for the repellers of the single FC (up to -3 kV) and the array (up to -300 V). The last three wires guarantee adequate grounding of the complete housing. Figure 1 shows the CAD-drawings of the complete detector, the array, and the single FC, respectively. Due to space limitations we were forced to choose the design as compact as possible.

A. Thermal design considerations

Our source is designed for an extraction voltage of 20 kV. Given an ion current of 2 mA, we needed to design the imaging system to withstand a thermal load of 40 W. This results in an enormous heat stress, especially for the large single FC and the front plate, which defines the FCA's apertures. In fact, the heat load on the small FCs of the FCA is still considerable, necessitating detailed simulations of the detector assembly. The need for such careful thermal design considerations is underlined by the fact that heat radiation and, to a lower extend, heat conduction are the only processes that can cool the detector. The critical locations are the wire connections to the miniature FCs and the ceramics, which hold the mini-FCs in place. We have thermally insulated the hot parts from the rest of the detector and increased the radiative area of the front plate with grooves and sideways extension (see Fig. 1). Thus, the detector system can be cooled by passive radiative cooling. We found maximum temperatures around 1300 K on the surface and ~500 K inside the housing. This lower temperature is low enough to allow use of standard vacuum and high voltage proof materials such as Kapton and Macor.

B. Measuring scheme and electronics

The measuring electronics consists of three main parts, all included within a shielded box directly mounted on a vacuum flange outside the vacuum. One of the mentioned parts is a microcontroller triggering the commands and routines mentioned in the following and measuring the voltage with an integrated 10 bit analog-digital-converter (ADC). The second essential part is a current-to-voltage-converter (I-U-converter). Because of the direction of the current flux, we additionally need an inverter to get a positive voltage measurable with the mentioned ADC. To reach high resolution over a wide current range, the microcontroller automatically changes the measuring range of the I-U-converter from at the moment 50 μA maximum in three steps (factor of 10 each) to a minimum current of 50 nA with 10 bit resolution in each range. This is done by changing the value of the feedback resistor of the I-U-converter. A sketch of the switching circuit is shown in Fig. 2. The measuring speed is adapted to the speed of the stepping motor driving the detector through the beam at a frequency of 300 Hz, though the electronics is designed for a maximum measuring speed of effectively 10 kHz. The last part of the electronics is a 45-to-1 multiplexer consisting of switches with a leakage current as low as typically 2 pA. All of the cups (44 of the FCA and one FC) are connected via their own switch to ground by default or to the same measuring electronics separately when

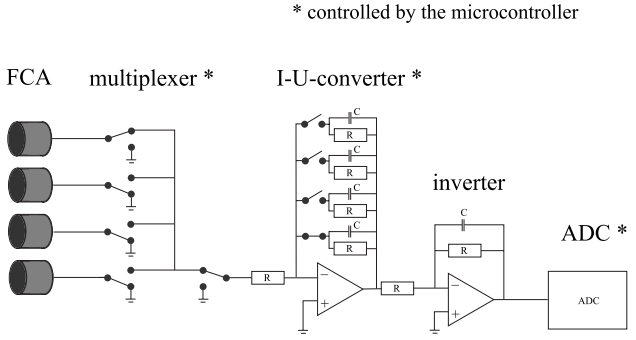

FIG. 2. Scheme of the measuring electronics.

needed. The standard grounding of each cup protects the electronics from high voltage discharges.

When measuring the total beam current using the FC, the detector with all cups grounded is driven–controlled by the microcontroller–to the right position. Then the FC is connected to the measuring electronics, grounding is resolved, and the measurements are made.

To scan the profile, a special routine is performed, again controlled by the microcontroller. This routine prevents the electronics from being damaged by high voltage discharges and from falsifying the results by measuring charges that have collected on the cups while not measuring and not being grounded. The routine begins with all cups connected to ground. Then the detector is moved one step in the direction of the beam. The size of one single step is 10 μm. Next, the first cup is connected via the multiplexer to the measuring electronics. Now the grounding of this cup is resolved and the measurement can be performed. After successful measurement the cup is grounded again and then disconnected from the multiplexer. Afterward, the detector is moved one step further in direction of the beam. After this routine is finished for the first cup, it is repeated for one cup after the other according to the scheme described above until all of the 44 cups of the array have performed a gaging. Until here, the detector has moved 0.44 mm in beam direction (10 μm $\times$ 44 cups of the array). To scan a length (at the detector-specific constant width) of i.e., 45.6 mm (as seen in Fig. 3), the complete array needs to be iteratively measured 90 times [90 repetitions $\times$ 44 cups $\times$ 10 μm + length of the detectors scanning area (6 mm)]. The number of repetitions can be defined by software. A typical scan with about 4000 measured points takes about 15 s. This includes moving the detector, automatically choosing the right measuring range and calculating the mean value of three measured values for each point. To move the detector back to the starting position and to transfer the readings to a personal computer, additional 20 s are needed. The limiting factor by now is the driving speed of the stepping motor, which is set to 300 Hz. The switching and measuring electronics are able to work at a frequency of about 1 kHz and higher. Then, a complete scan with data transmission would take only about 10 s.

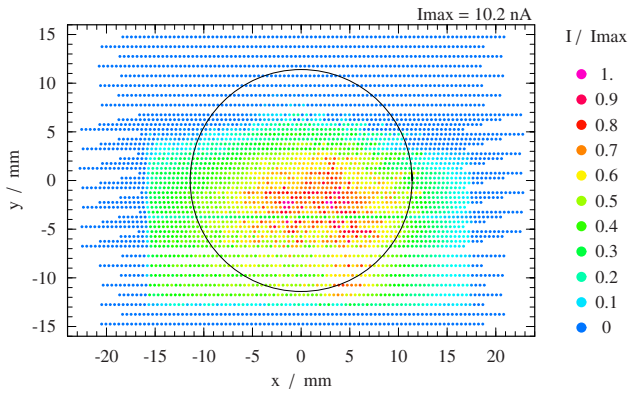

FIG. 3. (Color online) Illustration of the first measured profile of the beam (true to scale but enlarged). This image is used to evaluate the characteristical qualities of this detector system.

IV. FIRST MEASUREMENTS

Here we describe some of our first measurements of beam profiles with the new detector system presented in this paper. We will discuss some of the main characteristics and also the detailed calibration of the system. The latter is crucial, as small variations in the open diameter of the small apertures of the miniature FCs have a non-negligible effect on the measured currents.

A. General considerations

Figure 3 shows one of the first measured profiles. It specifies a profile with one peak in the intensity distribution. The orientation of the detector can be deduced from Fig. 1, where the directions of the x- and y-axis are shown. As one can see, the FCA is mounted parallel to the y-axis in the detector housing and is driven through the beam in x-direction. This is why the figure shows 44 "lines" parallel to the x-axis. Each of the lines corresponds to one cup moving through the beam measuring at a constant frequency. The distance between the centers of two points on one line is 0.44 mm, while the points' diameters are 0.3 mm. As we decided to measure a distance of about 45 mm in x-direction, we need 90 repetitions of one complete FCA measurement. Ninety repetitions times 44 cups each gives a total of 3960 current values with corresponding positions from which this profile is reconstructed. We can see that the ratio of measured area to total area is large enough to guarantee reliable information about the profile. Furthermore, we see that the diameter of the apertures is small enough to provide high resolution in position. Since the origin of the axes $(x,y=0)$ equals our desired beam line, we observe a small misadjustment of the beam. In addition, one can see the image of the blinds that reduce the beam in the beam line at positions $x=-16$, $x=17$, and $y=-13$. Here the intensity drops from a value of ≥ 0 to 0. Since the beam center is skewed in the $-y$-direction, the limiting blinds in the positive y-axis range are not visible in this color scale. In addition to the normal use as a profile monitor, we can use this detector as a FC with variable diameter or even form. The circle in Fig. 3 shows the location of the large FC. Given the high degree of coverage of the beam profile, an accurate estimate of the

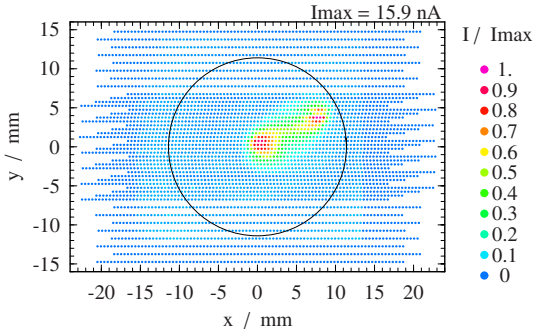

FIG. 4. (Color online) Beam with two maxima in the intensity distribution and a ring around the peaks (approximately at the position of the drawn-in FC but hard to see in this color scaling) (uncorrected).

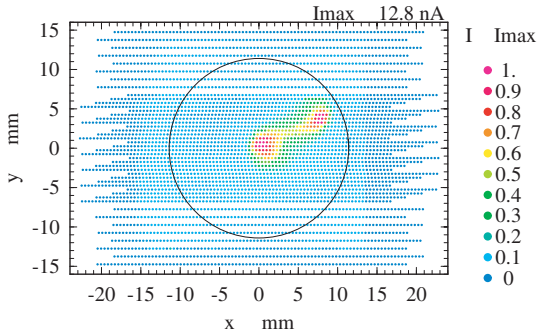

FIG. 6. (Color online) Same profile as shown in Fig.4 but corrected (Bezier-fit).

total beam current can be obtained and verified using the FCA and the large FC in combination. The line of low currents at $y=-4.5$ mm is discussed in Sec. V.

B. Resolution of current measurements

From the measured data we find the limiting resolution in our current measurements to be about 50 pA. This value equals the theoretical value determined in section B and is limited by the resolution of the ADC and/or the values of the feedback resistors in the I-U-converter. In retrospect, using another ADC or feedback resistors, the resolution could be increased. Additionally, we measured the noise produced by the electronics using a pico-amperemeter. We found the noise to be less than 5 pA, showing the excellent sensitivity of the setup.

C. Position resolution

Examining the figures showing measured profile scans (see Figs. 3, 4, and 7, respectively), we can ascertain that the chosen resolution is high enough to precisely present details of the particular beam profiles. The resolution in y-direction is defined by the detector design. In x-direction the resolution is variable. While reducing the distance between two repetitive measurements increases the time for one scan, an increase in this distance would lead to worse resolution. To us, the chosen compromise seems reasonable and allows us to detect structures on a millimeter-scale.

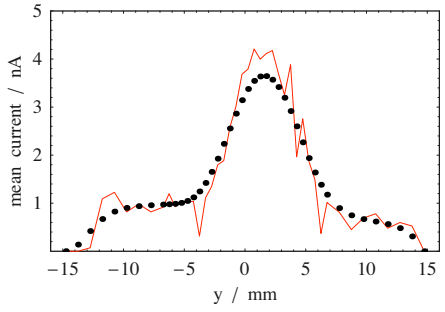

FIG. 5. (Color online) Transverse profile (y-direction) of the beam shown Fig. 4; red line=uncorrected, black dots=fitted with Bezier.

D. Cross-talk

To examine the cross-talk between two adjacent cups and the wires connecting the cups to the electronics, we focus on the second and third lowest cups in the y-direction ($-13 \leq y \leq -14$). Here one cup detects a beam current ($I_{\text{cup}} \geq 0$), while the other does not ($I_{\text{cup}}=0$, caused by the $-y$ blind). Though the current hitting the upper cup is quite low, we expect the same behavior even if the intensity difference between both cups is remarkably larger because of geometrical reasons of the design. To investigate cross-talk between single wires, we again choose the second lowest cup not measuring any current. The wire closest to the wire of this cup leads to a cup positioned at $y=-6$. This cup measures a comparatively high current. This seems to have too little influence on the neighboring wires to be measurable with our electronics. In summary, we can state that we are not able to detect any cross-talk neither between cups nor wires. Even at higher intensities the induced signal would be orders of magnitude smaller than the true signal, so we can neglect this effect. Profiles measured at higher intensities confirm this.

V. INTERCALIBRATION OF THE FCA CUPS

The three profiles shown in Fig. 3 as well as in Figs. 4 and 7 have been measured using the same detector. Especially in Fig. 7, one can obviously see that the measured intensities of the cups at $y=-4$, 4, and 6 are remarkably lower than the intensities measured with the neighboring cups. This effect is not a result of the true beam profile. It is based on a variation in the apertures' diameters. While production tolerances are low enough to guarantee only very small variations in the diameters of the apertures, pollution of the apertures by dust or dirt seems a realistic reason for this effect. However, at the three mentioned cups the variations seem large enough to be realized directly. Variations on smaller scales need more detailed analysis. For this purpose we propose an intercalibration routine, which is explained in the following. It can be used for a rough calibration. Here, no further data than the measured profile data are needed. For standard applications the accuracy received with the first method should be sufficient.

For this calibration method we use the recorded data of the measured profile. For each cup we calculate the mean value of the measured current. Plotting the mean current of each single cup over the cups y-position, we get a one-

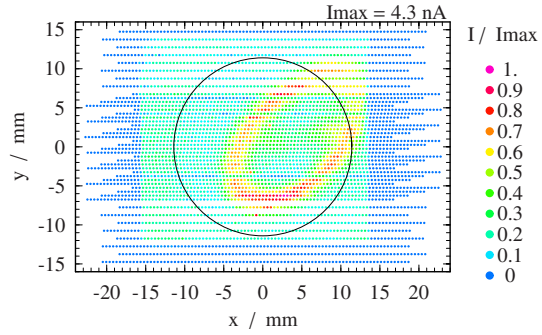

FIG. 7. (Color online) Typical hollow beam (uncorrected).

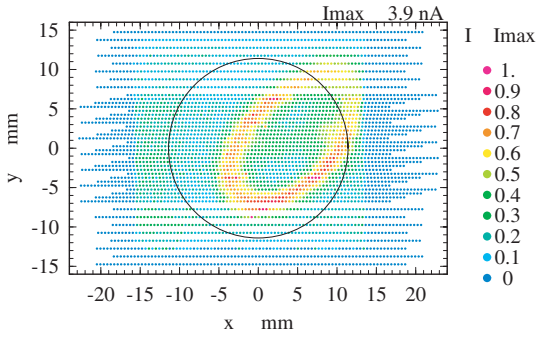

FIG. 9. (Color online) Same profile as shown in Fig. 7 but corrected (Bezier-fit).

dimensional profile of the beam in y-direction as if using a wire scanner. These profiles are shown in Figs. 5 and 8 (red lines). One can find that the main minima in these one-dimensional profiles appear at the same y-positions where the corresponding two-dimensional profiles show a constantly smaller measured intensity (in y-direction, as mentioned above). Assuming a small variation in the holes' diameters around a mean value, we roughly correct this effect by applying a Bezier-fit to the transverse profiles (see Figs. 5 and 8, black dots, one for each cup). From the measured and the fitted values for each cup, we can calculate a correction coefficient. Using these coefficients to correct the measured values, we receive corrected profiles as shown in Figs. 6 and 9.

We can state that this kind of data correction efficiently modulates current values of cups with too low measured intensities compared to neighboring cups. Using the Bezier-fit, we only make the assumptions that the beam profile has a continuous gradient and the diameters of the apertures vary around a mean value, which both seem reasonable. However, we also obtain slightly smoothened profiles that are very close to the true profiles. Unfortunately, the smoothing also has an effect on the prior sharp intensity drops influenced by blinds on the beam line. Here, the sharp decrease in intensity is also smoothened and falsified. In addition, in some cases we can observe that the automatically corrected profile leads to a lower total intensity. This, of course, could be adjusted too. To optimize cup intercalibration, also a more adapted fitting routine could be developed. In each case one can decide depending on the needs whether to perform the intercalibration or not. Since the variations in the apertures are detector-specific, intercalibration only needs to be performed

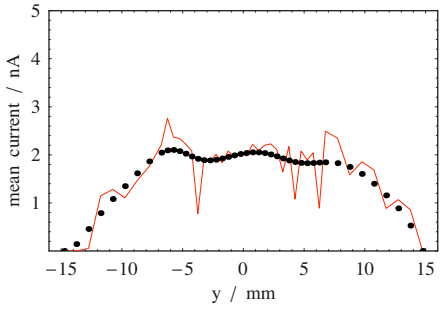

FIG. 8. (Color online) Transverse profile (y-direction) of the beam shown in Fig. 7; red line=uncorrected, black dots=fitted with Bezier.

once for each detector or (if the variations are pollution-induced) in certain time intervals. Finally, we note that a second identical detector, which was placed much closer to the ion source at significantly higher beam powers, shows much smaller variations. The reason might be that possible dust or dirt is burned away because of the mentioned enormous thermal stress.

VI. CONCLUSIONS AND DISCUSSION

The new kind of detector presented here is based on the proven FC design and combines durability and high sensitivity for high-resolution measurements of current and position. Compared to the sensitive scintillation screens made of crystals, the resolution reached with this detector is lower but as high as 58 dpi in x-direction and 51 dpi in y-direction. This enables us to detect structures on millimeter-scale easily. Regarding the detectable beam current range, this detector exceeds the ranges of scintillation screens in both directions. Accepting errors of about 10%, we are able to measure current fluxes as low as 200 $\mathrm{nA/cm^2}$ using the current feedback resistor configuration in the I-U-converter. Tolerating even higher errors or changing the configuration, the detectable current flux can be lowered. Since the recorded signal does not depend on the extraction voltage, we are also able to measure current fluxes up to 20 $\mathrm{mA/cm^2}$, as long as the total beam power does not exceed ~40 W. This again is valid for the current configuration of the feedback resistors and can be adapted depending on the demands.

Compared to wire scanners this detector has the disadvantage of destroying the beam during the measurement. However increasing the measuring speed, interruption time of the beam should be reducible to approximately 10 s. Assuming the same sensitivity in the measuring electronics, a wire scanner should be able to detect current fluxes with lower intensity since wire scanners always measure across a larger area interacting with the beam (charge integration over the length of a wire). However, wire scanners show three disadvantages. First, they do not provide the possibility to suppress secondary electrons, so the recorded signal is too high and requires calibration with a FC. Second, the useful lifetime of the thin wires is limited due to sputtering effects. Third, the profile cannot be measured directly but needs to be inverted from fitted values by Abel inversion as mentioned above. This leads to smoothening effects or even more se-

vere problems, which might falsify the results, depending on the true shape of the beam. For example, Figs. 4 and 7 show two profiles that could not be reconstructed from wire scanner measurements.

So far, our detector has been exposed to the beam for roughly 10 h in total at different beam intensities and powers. We were not able to detect any changes in the response. If after a long period of exposure single parts of the detector (i.e., the front plate containing the apertures of the FCA or the tiny cups of the FCA themselves) needed to be renewed because of sputtering or deposition defects, these parts were easily accessible and replaceable. To reduce costs and to simplify the replacement, we used standard crimp pins as the tiny cups of the FCA.

In conclusion, we have presented a novel concept for a position-sensitive beam monitor, which is very sensitive (50 pA), has a large dynamic range (50 pA$\rightarrow$50 μA), and is very durable. An additional advantage is the high speed of the measurement, which is possible in a limited spatial region.

ACKNOWLEDGMENTS

This work was supported in part by the German Research Foundation HBFG-100–494.

[1] D. S. Todd, D. Leitner, and M. Strohmeier, *Low Energy Beam Diagnostics at the Venus ECR Ion Source*, Beam Instrumentation Workshop 2008 (Lake Tahoe, CA, 2008).
[2] P. Spädtke, R. Lang, J. Mäder, J. Rossbach, K. Tinschert, and J.Stetson, *Ion Beam Extracted from a 14 GHz ECRIS of Caprice Type* 17th Workshop on ECR Ion Sources and their Applications, ECRIS 06, Chinese Academy of Sciences, (HEP&NP, 2007).
[3] T. Iida, Y. Maekawa, R. Taniguchi, M. Byakuno, and K. Sumita, Rev. Sci. Instrum. **52**, 1328 (1981).
[4] *Handbook of Ion Sources*, edited by B. Wolf (CRC, NY, 1995).
[5] M. Suchanska, A. I. Bazhin, and E. I. Konopelko, Phys. Status Solidi B **182**, 231 (1994).
[6] G. Stover, IEEE Trans. Nucl. Sci. **32**, 1988 (1985).
[7] D. Knolle, D. Ratschko, and M. Gläser, Rev. Sci. Instrum. **67**, 3082 (1996).
[8] E. P. EerNisse, G. D. Peterson, and D. G. Schueler, Rev. Sci. Instrum. **46**, 266 (1975).

NEXT REFERRED PUBLICATION: OWN CONTRIBUTION: approx. 85%

SPATIALLY RESOLVED MEASUREMENTS OF ELECTRON CYCLOTRON RESONANCE ION SOURCE BEAM PROFILE CHARACTERISTICS Lauri Panitzsch, Michael Stalder, and Robert F. Wimmer-Schweingruber, Rev. Sci. Instrum. 82, 033302 (2011), DOI:10.1063/1.3553013

MEASURING TECHNIQUE AND POSITION OF DATA ACQUISITION:

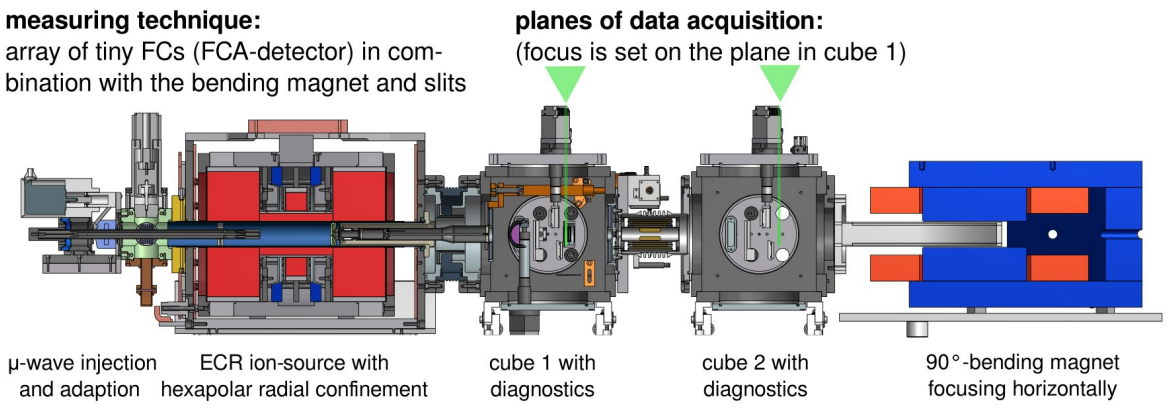

MOTIVATION:

The first investigation regarding the distribution of charged particles along the axis of an ECR ion source was performed at a comparatively large distance of about 45 cm downstream from the extraction. The object plane of the bending magnet is located at this position (the green plane marked in cube 1), and the beam can be clipped/reduced by the use of slits. The detection principle can be described as follows: The source is tuned to deliver a beam of residual gas ions (mostly oxygen and nitrogen) at all charge states. By adapting the extraction voltage and the puller electrode's axial position the beam is strongly focused. This can be verified by detecting triangular and star-like structures in the beam profiles measured at the position (marked in green in cube 1 in the figure above). Then, the slits are used to only allow one spatially limited fraction of the beam at a time to pass the bending magnet for subsequent m/q-separation and identification. The various probed positions are chosen at characteristic positions of the beam profile. To obtain the beam profiles in high resolution the FCA (see first publication) is used. The results show the spatial distribution of different ion species in that plane.

NEW EXPERIMENTAL INSIGHTS:

The triangular and star-like structures observed in strongly focused ion beams are dominated by ions of one charge state, each. Beam-steering can be achieved by the use of a 3D-movable extraction.

Spatially resolved measurements of electron cyclotron resonance ion source beam profile characteristics

Lauri Panitzsch,[a] Michael Stalder, and Robert F. Wimmer-Schweingruber
Institute for Experimental and Applied Physics (IEAP), University of Kiel, Kiel, Germany

(Received 24 November 2010; accepted 15 January 2011; published online 7 March 2011)

Simulations predict that the concentric rings and the triangular structures in the profiles of strongly focused ion beams that are found in different experiments should be dominated by ion species with the same or at least similar *m*/*q*-ratio. To verify these theoretical predictions we have tuned our ECR ion source to deliver a beam consisting of multiple ion species whose particular *m*/*q*-depending focusing ranges from weakly focused to overfocused. We then recorded spatially resolved charge-state distributions of the beam profile at characteristic positions in the plane perpendicular to the beam line. The results validate theoretical predictions and are summarized in this paper. To achieve the required beam profile characteristics we moved the extraction along the beam line to achieve stronger focusing than by only changing the extraction voltage. To fit the regions of interest of the beam profile into the transmission area of the sector magnet, we steered the beam by moving the extraction in the plane perpendicular to the beam axis. The results of both investigations, beam focusing and beam steering by using a 3D-movable extraction, are also reported in this paper. A brief overview of the new beam monitor extensively used during these measurements, the Faraday cup array, is also given. © *2011 American Institute of Physics*. [doi:10.1063/1.3553013]

I. INTRODUCTION

The beam profile is a crucial parameter of an ion beam. Therefore, great effort has been spent on the visualization of beam profiles and the understanding of their formation. Wire scanners were often used to record the ion current distribution in the plane perpendicular to the beam axis. Starting with a single-peaked Gaussian-distributed ion flux, one then attempts to reconstruct an estimate of the beam profile. However, when probing non-Gaussian ion flux distributions, that method may lead to a strong discrepancy between true and inferred beam profile. At the cost of losing absolute values for the beam-current distribution an enormous increase in spatial resolution can be gained by using scintillating materials such as KBr or quartz for profile visualization. This technique has shown that the true beam profile may differ significantly from a Gaussian. In fact, depending on the tuning of the corresponding ion source, a superposition of concentric rings of increased particle density can often be observed. In some cases a triangular structure may overlay these rings.

Extensive computer simulations lead to the conclusion that each ring is dominated by ions of a specific *m*/*q*-ratio due to ion-optical effects.[1,2] According to the simulation results the diameter of a particular ring decreases with decreasing *m*/*q*-ratio because the focusing increases. The lowest *m*/*q*-ratios may then be overfocused and form triangular structures (if using a hexapolar magnetic radial plasma confinement), as found in different experiments.[3–6]

To validate these simulation results by experiment we tuned our ECR ion source to provide a strongly focused to overfocused beam of multiple ion species with different *m*/*q*-ratios. The strong focusing was achieved by lowering the extraction voltage and moving the extraction electrode along the beam axis. Our experimental observations regarding beam focusing using both techniques mentioned above are summarized in Sec. III A. As a result, we succeeded to tune the source to deliver an ion beam with a beam profile consisting of a triangular structure superimposed on circular structures. To fit the regions of interest of the beam into the analyzing magnet (for subsequent *m*/*q*-recordings), we steered the beam by moving the extraction electrode in the plane perpendicular to the beam axis. The 3D-movable extraction electrode is a special feature of our source, not only allowing us to focus but also to steer the beam. The results of our beam-steering investigations are reported in Sec. III B. Limiting the beam to profile-characteristic positions in the plane perpendicular to the beam line, we recorded the *m*/*q*-spectra of the particular spots to receive a spatially resolved charge-state distribution of the ion-beam profile. Using this technique we were able to confirm that each ring as well as the triangular structure is dominated by a specific *m*/*q*-ratio and therefore validate the simulation results by experiment as shown in Sec. III C.

To monitor the beam from the ECRIS to the experimental chamber we developed a high-resolution beam-profile measuring device (a Faraday cup array, abbreviated as FCA in the following), that will be introduced briefly in Sec. II C. More detailed information concerning the FCA may be found in Ref. 7.

II. EXPERIMENTAL SETUP

A. The ECR ion source

The ion source we are using to generate charged particles is an all-permanent magnet ECR ion source. The radial magnetic field for plasma confinement has hexapole geometry, the axial field is plateau-shaped to increase the resonance

[a]Electronic Mail: panitzsch@physik.uni-kiel.de.

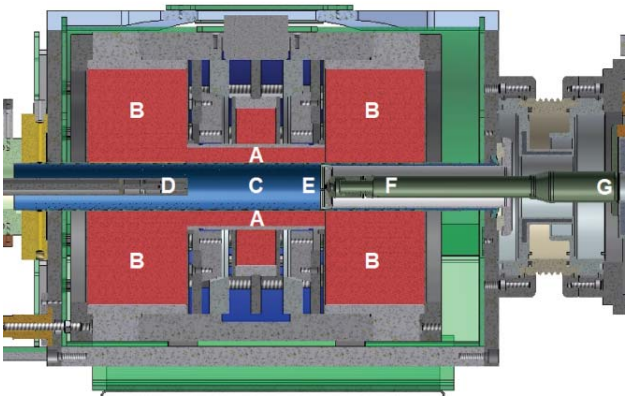

FIG. 1. (Color online) ECRIS with 3D-movable extraction system. The red areas (A and B) indicate the field-forming permanent magnets. In addition, the plasma chamber (C) with a biasable microwave antenna (D), the plasma electrode (E), and the 3D-movable puller electrode (F) with its output (G) are shown.

zone. The superposition of the magnetic fields is optimized for a microwave frequency of 11 GHz. All the experiments described in Sec. III were performed at this frequency. The output power of our microwave amplifier was set to 50 W at a comparatively high vacuum pressure of 1.0×10^{-5} mbar. The microwaves are guided axially into the plasma using an antenna. The source can be biased up to 20 kV with respect to the 3D-movable extraction electrode that is on ground potential to extract the ions. A sketch of the ECR ion source is shown in Fig. 1.

B. Setup of the source

Figure 2 shows an overview of the setup. At the bottom, you can see the ECR ion source which generates the beam of charged particles. Accelerated by a high-voltage gap the beam passes two cubes before entering the sector magnet. Both cubes are equipped with a FCA, as well as with slits to limit/clip the beam in the $\pm x$- and $\pm y$-direction (where the z-direction is coaxial with the beam). At these positions ("cube 1" and "cube 2") the detector can be used to record beam profiles and to measure the total beam current. During our measurements we used the detectors to determine the beam profiles only. After having passed the sector magnet the ions of the beam are separated by their m/q-ratio. Thus, tuning the magnetic field, we use the FCA in "cube 3" to record the respective ion charge spectra. More detailed information about the particular test procedures is given in the corresponding subsections of Sec. III while detailed information on the detector itself will be given in Subsection II C.

C. The FCA detector

To monitor the ion-beam profile we have developed a new kind of detector system. This new system is a combination of a standard (large) Faraday cup for measuring the total beam current, and an array of tiny ($\varnothing = 0.3$ mm) Faraday cups for direct and accurate beam profile recordings in high resolution. The FCA is designed for a spatial resolution of 22×20 measurements/cm^2. This high spatial resolution enables the detection of beam structures on mm-scale covering a scannable area of 45×30 mm^2. The detector electronics is characterized by its large dynamic range (present configuration: 50 nA $\rightarrow$ 50 μA at 10- bit resolution, the lowest measurable current is 50 pA). The detector can be used for profile measurements at current densities ranging from 200 nA/cm^2 up to 20 mA/cm^2 as long as the total beam power remains lower than approximately 40 W for continuous heat loads. Since this system performs a direct profile measurement with secondary electron suppression, the influence of systematic errors (inversion calculations with assumptions for the beam profile as well as secondary electron escape) is minimized. Typically, a single profile scan takes 10 s with the present electronics. Due to the high dynamic range of the current measuring electronics it is also possible to use the detector-integrated large Faraday cup to determine the total beam current or, in combination with a sector magnet, for beam spectra recordings. A CAD view of the detector system is shown in Fig. 3. The complete FCA detector is presented in more detail in Ref. 7.

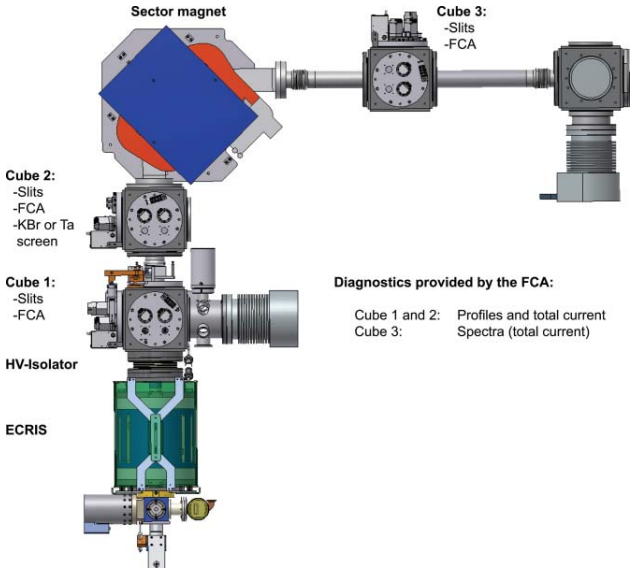

FIG. 2. (Color online) Setup of the source. The ions are generated in the ECRIS. Moving along the beam line the ions pass two cubes providing possibilities for beam diagnostics (FCA) and limitation (slits) before entering the sector magnet. The FCA in cube 3 is used in combination with the sector magnet to record the ion-beam spectra.

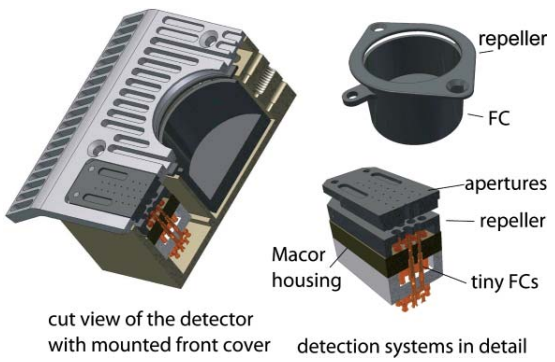

FIG. 3. (Color online) CAD drawing of the new detector system.

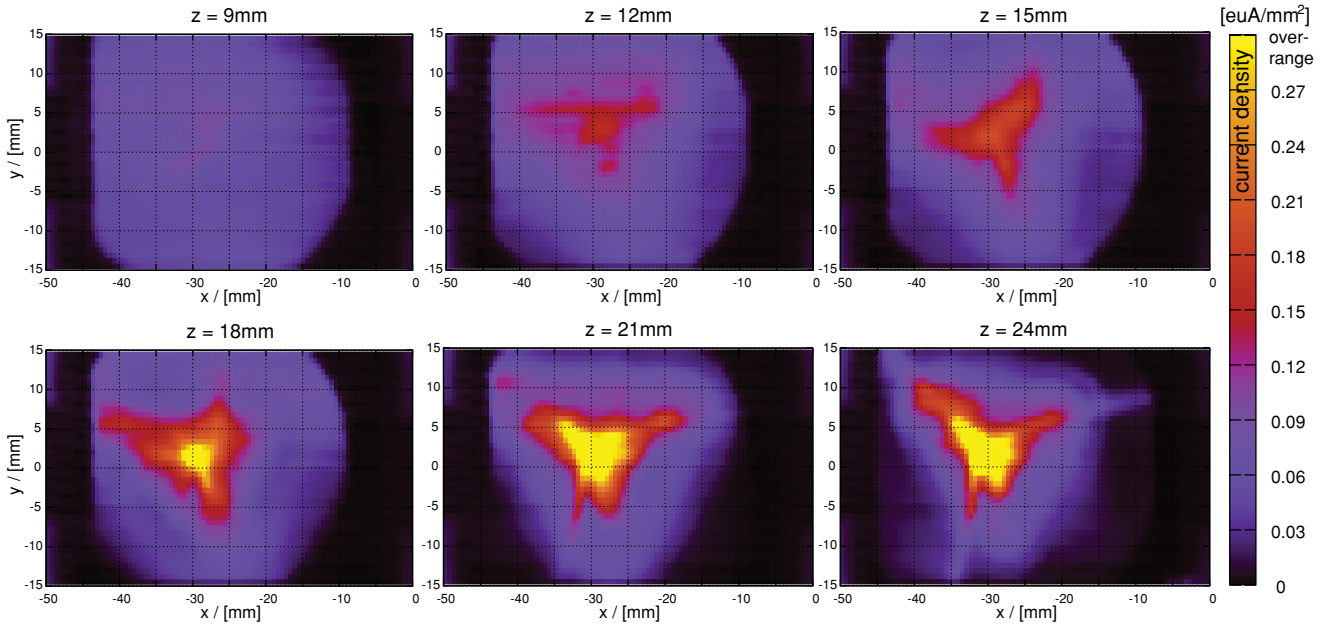

FIG. 4. (Color online) Beam profiles: beam focusing by moving the extraction electrode along beam axis; profiles recorded in cube 1.

III. MEASUREMENTS

A. Beam focusing

In order to investigate the beam focusing capabilities of the 3D-movable extraction we ignited an oxygen-dominated plasma with residual gas impurities and recorded beam profiles in cube 1 for different extraction electrode positions along the beam axis at a constant acceleration voltage. The results can be seen in Fig. 4.

The recorded profiles are shown in the same current density scale. This reduces the visible resolution slightly but simplifies comparison. The focusing effect with increasing distance between the extraction electrode and the plasma electrode is clearly visible. The main beam area appears to shrink in size and a triangular structure emerges. In addition, one can see an abrupt decrease of intensity with circular shape in all recorded profiles. This is caused by the extraction electrode. Since its diameter-to-length ratio is small, outer beam regions are clipped away and the round, limiting shape of the extraction electrode's output (marked "G" in Fig. 1) is mapped here.

To increase focusing to a strongly focused beam, we also lowered the acceleration voltage with the extraction electrode fixed at the greatest distance to the plasma electrode where the greatest focusing effect at present plasma parameters was observed, as seen in Fig. 4. The results for this voltage-dependent focusing are shown in Fig. 5.

One can easily observe that the technique of lowering the extraction voltage leads to further beam focusing resulting in a strongly focused beam. Again, the main area of the beam appears to shrink, and the clear rings that are superimposed by a triangularlike structure become visible.

With the described plasma parameters (especially, plasma density) the focusing behaves as follows: By increasing the distance between the plasma electrode and the extraction electrode at a constant acceleration voltage the shape of the neutral plasma sheath changes due to the change of the electrostatic extraction field. With the given source geometry this results in a change of the divergence of the beam. Passing through the fringe field caused by the magnets for axial plasma confinement the change in divergence leads (again, in this case) to beam focusing. The same is true for the focusing at a constant position of the extraction electrode when lowering the extraction voltage. By lowering the voltage, the penetration length of the electric field into the plasma is reduced, and therefore changes the shape of the neutral plasma sheath in the same manner. This also results in beam focusing via changing the beam divergence at the extraction.

B. Beam steering

To investigate the beam steering capabilities of the 3D-movable extraction, we again used an oxygen-dominated plasma with residual gas impurities at the same source conditions as in Sec. III A and recorded beam profiles measured in cubes 1 and 2 for different extraction electrode positions perpendicular to the beam axis. The resulting profiles can be seen in Fig. 7.

The upper cross in Fig. 7 shows the profiles recorded in cube 1 while the profiles measured in cube 2 are presented in the lower cross. The green x and y axes illustrate the position of the extraction electrode when the particular profile was measured (the origin of the x and y axes is at the beam line).

Our beam steering investigations lead to the conclusion that we can effectively steer the beam by changing the position of the extraction electrode. When moving the extraction horizontally the beam is shifted mainly vertically and *vice versa*. The resulting movement of the beam is always roughly perpendicular to the movement of the extraction. The beam seems to be rotated by $\approx 90^\circ$. Due to the greater radial

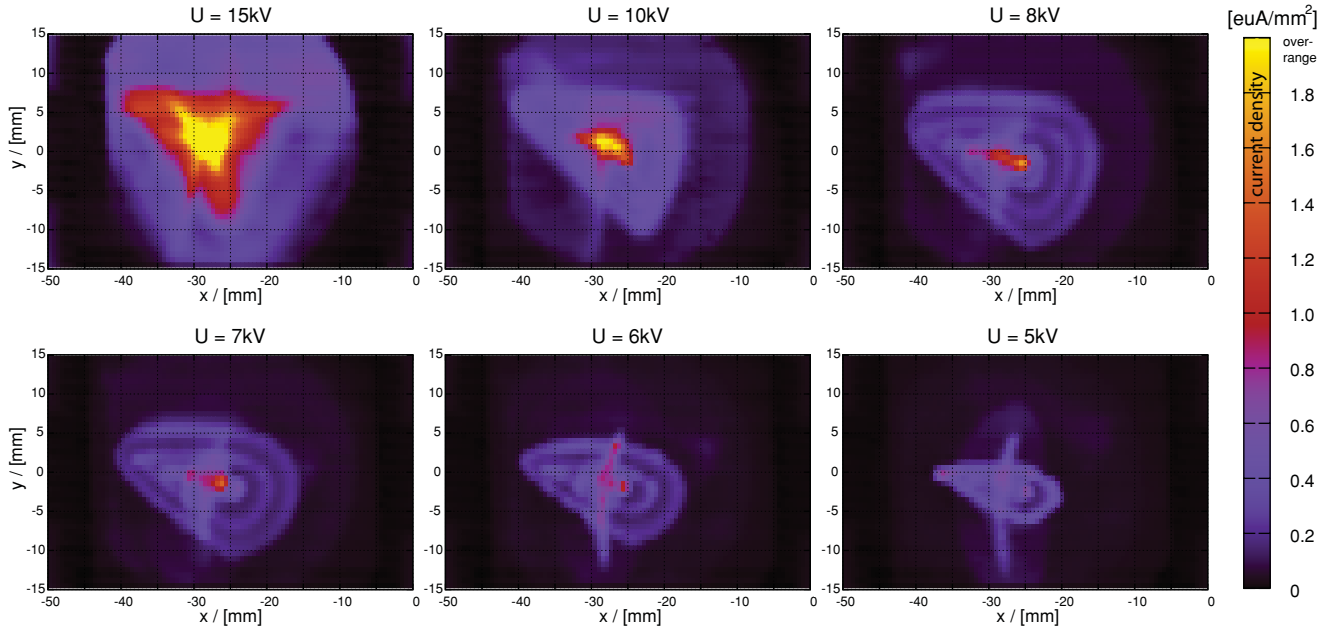

FIG. 5. (Color online) Beam profiles: beam focusing by lowering the extraction voltage; profiles recorded in cube 1.

displacement of the beam with longer drift distance it is easier to track the response of the beam in cube 2 where the beam structures are enlarged and only slightly changed in their characteristics. A compendium of the observed beam shifts is presented in Fig. 6.

One possible explanation for this effect could be the magnetic rotation that a beam of charged particles experiences when traveling through a magnetic lens[8] (in this case caused by the fringe field of the plasma confining axial magnets). The degree of rotation can be estimated by the following formula valid for magnetic lenses:[9]

$$\Theta_{\text{tot}} = \frac{q}{2mv} \int B_z dz \tag{1}$$

with Θ_{tot} being the angle of rotation in units of π, and B_z being the magnetic field strength in axial direction z. The particles' charge, mass, and velocity are expressed by q, m, and v, respectively. Using the expression $qU = \frac{1}{2}mv^2$ to replace the velocity v, the formula converts to

$$\Theta_{\text{tot}} = \sqrt{\frac{q}{8mU_{\text{extr}}}} \int B_z dz, \tag{2}$$

where U_{extr} is the extraction voltage. The magnetic field configuration along the beam axis at the extraction region can be seen in Fig. 8. The integral $\int B_z dz$ is approximately 0.035 Tm.

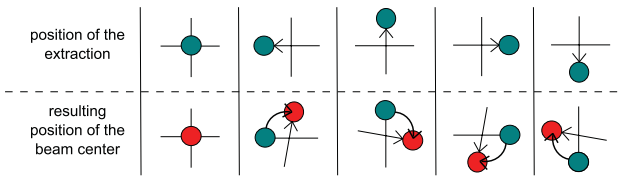

FIG. 6. (Color online) Schematic summary of the reaction of the beam to the traverse of the extraction electrode perpendicular to the beam line.

We used an oxygen-dominated plasma for this beam-steering test, again with residual gas impurities. We determined the main ion compositions of the two rings visible in the beam profiles of Fig. 7 using the same technique as described in Sec. III C. The outer ring in Fig. 7 is dominated by O^{2+} while the inner ring is dominated by N^{2+}. Because the m/q-ratios of these two ion species have similar values, magnetic rotation (depending on q/m) has a similar effect. We use the following values to estimate the angle of rotation Θ_{tot}: $q = 2 \times 1.602 \times 10^{-19}$ C, $m = 16 \times 1.7 \times 10^{-27}$ kg, and $U_{\text{extr}} = 7$ kV.

This leads to a total rotation of $\approx 0.5\pi$. This equals a rotation of 90° and would explain the reaction of the beam movement we have recorded. Of course this crude attempt to explain the beam reaction is only an approximation. Sophisticated beam transport simulations which take the electric and magnetic fields and the exact source geometry into account

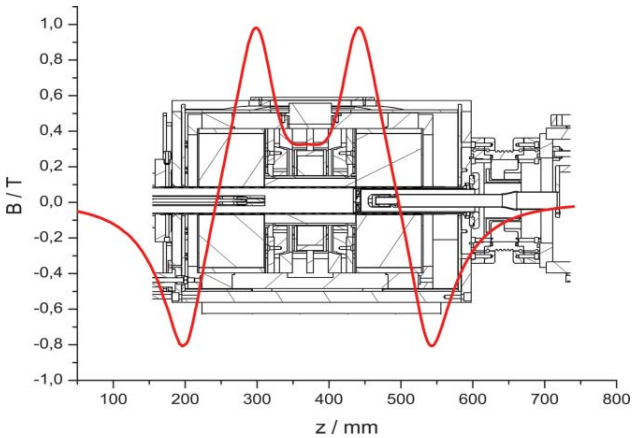

FIG. 7. (Color online) Axial magnetic field at the extraction.

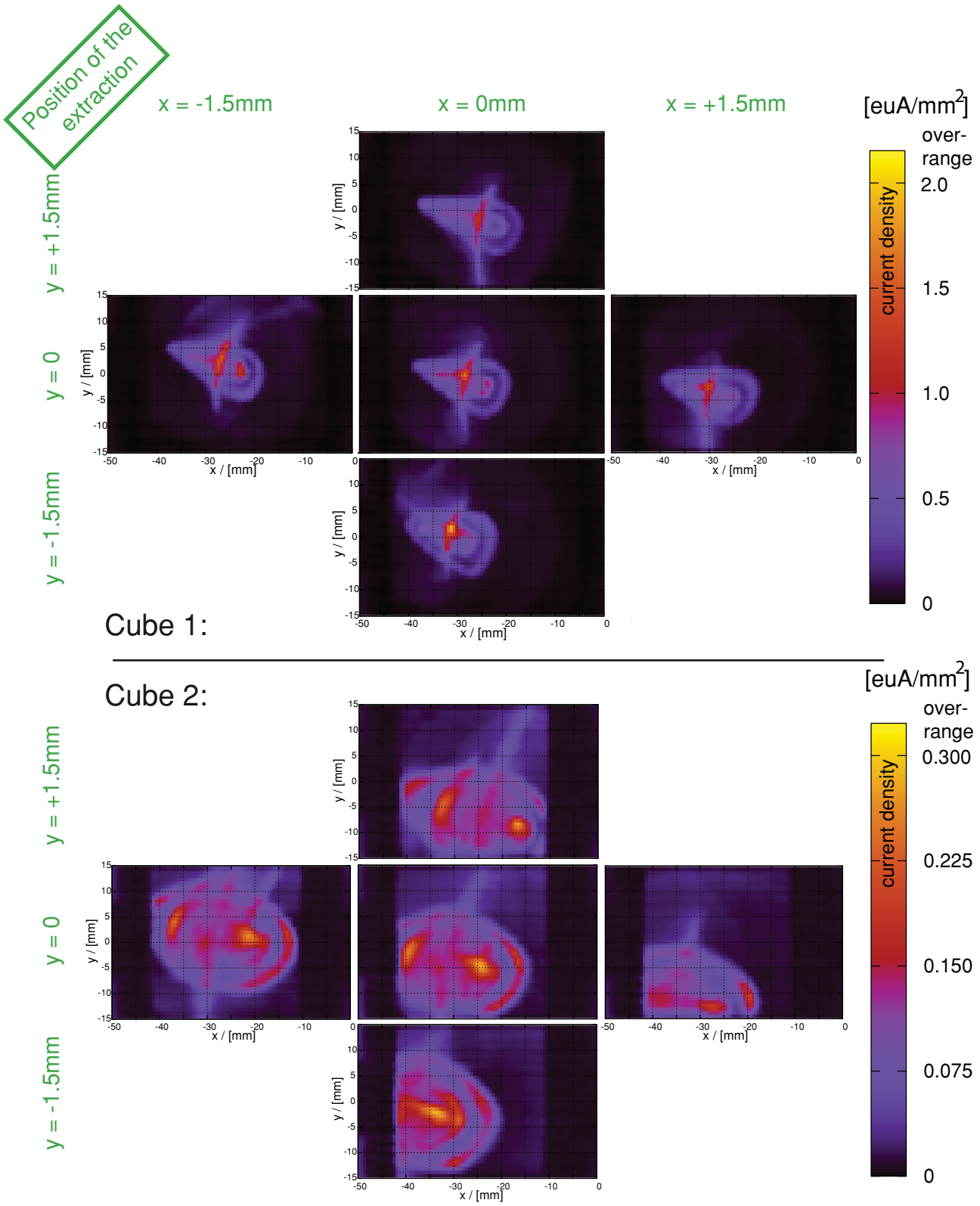

FIG. 8. (Color online) Beam steering by moving the extraction in the plane perpendicular to the beam axis; profiles recorded in cubes 1 and 2.

would be necessary to obtain deeper insights into the beam-steering processes.

A further effect to be mentioned is the beam broadening while traveling from cube 1 to cube 2 as a result of beam divergence.

In conclusion we can state that it is possible to steer the center of the beam by moving the extraction electrode in the plane perpendicular to the beam line. This steering slightly changes the beam structure. The capability of beam steering is, for example, of interest when a certain, noncentral area

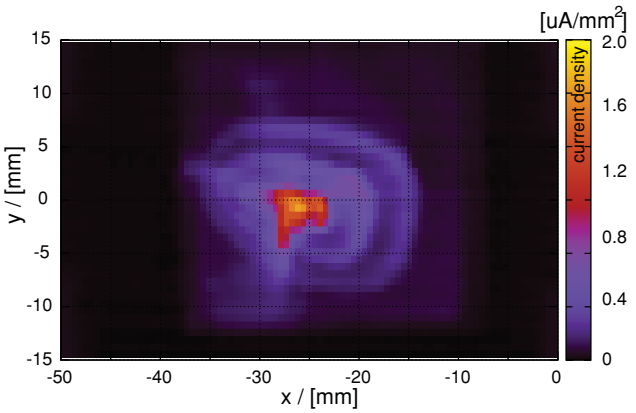

FIG. 9. (Color online) Profile of a strongly focused, oxygen- and nitrogen-dominated beam recorded in cube 1.

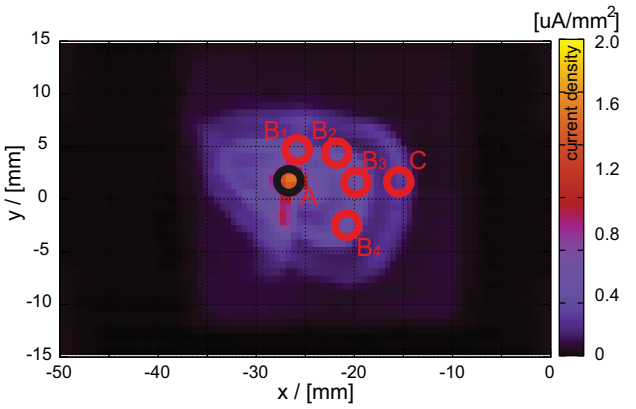

FIG. 10. (Color online) Profile of the beam that was analyzed (recorded in cube 1); since we needed to steer (lift) the beam, the structure differs slightly from the original profile shown in Fig. 9; the circles indicate the areas where spectra have been recorded from; the results are summarized in Table I.

of the beam (profile) needs to be selected/centered, e.g., to optimize for charge states (see Sec. III C).

C. Spatially resolved charge-state distribution of a strongly focused beam

Spatially resolved simulations of beam propagation (e.g., see Refs. 1 and 2) have shown that the profile of a multi-ion-species beam can contain circular and triangular structures instead of one central peak. This property becomes visible when the beam is focused adequately. These simulation findings are in agreement with observations recorded in several experiments[3–6] where beam profiles for different focusings have been recorded. Within these experiments, hollow rings (circular structures) are visible in the beam profiles that focus with increasing focusing strength of the used ion-optical lens and finally result in triangular structures. These triangular structures are supposed to be overfocused higher charge states. According to Spädtke *et al.*[3] the hollow structure and the triangular shape have their origin in the starting conditions of the ions and the hexapolar error, respectively. Simulations also show that each ring (or circular structure) is dominated by ions of a specific m/q-ratio because particles with equal m/q-ratio experience the same focusing. Ions with smaller m/q-ratio populate the inner regions while the species with higher m/q-ratio can be found in the outer regions of the beam profile.

As far as we know, spatially resolved charge-state distributions for the different profiles have not been recorded up to now. To validate the simulations by experimental observations we tuned our source to a beam profile similar to those reported in Refs. 3–6. The resulting profile measured with our profile scanner (the FCA) is shown in Fig. 9. We can see an (again oxygen- and nitrogen-dominated) ion beam with rings ranging from focused to overfocused at current focusing settings.

To determine the spatially resolved charge-state distributions of the beam profile at different positions, we used slits (in cube 1) to reduce the beam to a very small area that was then allowed to pass the sector magnet for m/q-spectra measurements. These small areas were chosen at characteristic profile positions, as marked in Fig. 10. To fit all these areas of interest into the analyzing magnet (especially, areas "B_4" and "C"), we needed to steer (elevate) the beam. Therefore, we moved the extraction electrode to the left perpendicularly to the beam axis in the horizontal plane. As expected, this lead to a minor change in the profile as can be seen by comparing Figs. 9 and 10. Using the limiting slits we recorded the m/q-spectra for the ion-distributions at the different marked positions (red circles) shown in Fig. 10. In Table I we summarize the results of the different spectra recordings. Since the absolute current values of the recorded spectra strongly depend on the size and the precise position of the particular clipping point, only relative values are of interest and therefore no absolute values are referenced in the table.

According to our measurements, the outer ring (measured at position C) mainly consists of the low charged ion species

TABLE I. Dominant m/q-ratios at different profile-characteristic positions (marked in Fig. 10).

A	N^{3+}	37%
	O^{3+}	50%
	N^{2+}	10%
	O^{2+}	2%
B_1	N^{3+}	5%
	O^{3+}	12%
	N^{2+}	37%
	O^{2+}	37%
	N^{+}	4%
	O^{+}	4%
B_2	N^{2+}	45%
	O^{2+}	45%
	N^{+}	4%
	O^{+}	4%
$B_3 + B_4$	N^{2+}	28%
	O^{2+}	55%
	N^{+}	10%
	O^{+}	5%
C	N^{+}	40%
	O^{+}	55%

N^+ and O^+. The inner ring (measured at positions B_1 and B_2 as well as at positions B_3 and B_4) is dominated by the "medium" charged ion species N^{2+} and O^{2+}. At position B_1 where the inner circular structure and the triangularlike, central structure overlap (as visible in Fig. 10) we additionally were able to detect the "higher" charge states N^{3+} and O^{3+}. We believe the reason for the higher charge states at this position to be the triangular (central) structure (consisting of the higher charge states) that is superposed on the circular structures (containing the medium charge states) here. The twice ionized ion species N^{2+} and O^{2+} seem to be strongly focused, forming the inner circular structure under current source settings while the comparatively higher charged ion species N^{3+} and O^{3+} are already overfocused and form the triangular structure and also populate the beam center (spot A). As already mentioned the formerly triangular structure—as recorded in Fig. 9— has been modified slightly by steering the beam and is therefore not directly identifiable since its shape has changed. At the central position A, forming part of the triangular structure, we detected mainly the higher ionisation states (N^{3+} and O^{3+}).

Analyzing our measurements we found the different rings around the center of a strongly focused beam profile to be dominated by ions in a narrow interval of the m/q-ratio. We have also verified the simulation findings that ions with higher charge states form the inner rings while the highest charge states are already overfocused and populate the triangular structure.

IV. CONCLUSIONS AND DISCUSSION

In conclusion, we can state that by using the 3D-movable extraction it is not only possible to focus the extracted ion beam by moving the extraction along the beam line, but also that beam steering can be achieved. For this the extraction needs to be moved in the plane perpendicular to the beam axis which results in a shift of the beam in the same plane (perpendicular to the beam axis). The shift direction depends on the exact extraction geometry including electric and magnetic fields and is a result of the magnetic fringe field formed by the magnets for axial plasma confinement. Inspite of these complications, a simple equation [Eq. (1)] appears to give a good approximation. Furthermore, no additional ion-optical elements are needed to effect beam steering already at the extraction.

In addition, we were able to determine a spatially resolved ion charge-state distribution of a strongly focused beam profile and experimentally validate simulation results from other groups. This, to our knowledge, is the first experimental confirmation that the observed rings around the beam center and the triangular structure of strongly focused beams are dominated by one m/q-ratio each.

ACKNOWLEDGMENTS

We thank C. Helmke for technical assistance and S. Kolbe for engineering support. This work was supported in parts by HBFG Grant No. 100-494.

[1] D. S. Todd, D. Leitner, and M. Strohmeier, *Low Energy Beam Diagnostics at the Venus ECR Ion Source*, Proceedings of the 13th Beam Instrumentation Workshop, Lake Tahoe, CA (2008).
[2] C. Pierret, L. Maunoury, S. Biri, J. Y. Pacquet, O. Tuske, and O. Delferriere, Rev. Sci. Instrum. **79**, 02B703 (2008).
[3] P. Spädtke, K. Tinschert, R. Lang, J. Mäder, J. Roßbach, J. W. Stetson, and L. Celona, Rev. Sci. Instrum. **79**, 02B716 (2008).
[4] J. Stetson and P. Spädtke, in *Proceedings of the IEEE Particle Accelerator Conference (PAC2007), Albuquerque, NM, 25–29 June 2007*, pp. 3789–3791.
[5] P. Spädtke, R. Lang, J. Mäder, J. Roßbach, K. Tinschert, and J. Stetson, High Energy Physics and Nuclear Physics **31**(S1), 192 (2007).
[6] J. Mäder, J. Roßbach, F. Maimone, P. Spädtke, K. Tinschert, R. Lang, L. Sun, Y. Cao, and H. Zhao, Rev. Sci. Instrum. **81**, 02B720 (2010).
[7] L. Panitzsch, M. Stalder, and R. F. Wimmer-Schweingruber, Rev. Sci. Instrum. **80**, 6 (2009).
[8] *Elektromagnetismus*, Auflage 8, edited by L. Bergmann, C. Schaefer, and W. Raith (Gruyter, Berlin, 1999).
[9] *Grundlagen der Elektronenoptik*, edited by W. Glaser (Springer-Verlag, Berlin, 1952).

NEXT REFERRED PUBLICATION: OWN CONTRIBUTION: approx. 90%

SPATIALLY RESOLVED CHARGE-STATE AND CURRENT-DENSITY DISTRIBUTIONS AT THE EXTRACTION OF AN ELECTRON CYCLOTRON RESONANCE ION SOURCE Lauri Panitzsch, Thies Peleikis, Michael Stalder, and Robert F. Wimmer-Schweingruber, Rev. Sci. Instrum. 82, 093302 (2011), DOI:10.1063/1.3637462

MEASURING TECHNIQUE AND POSITION OF DATA ACQUISITION:

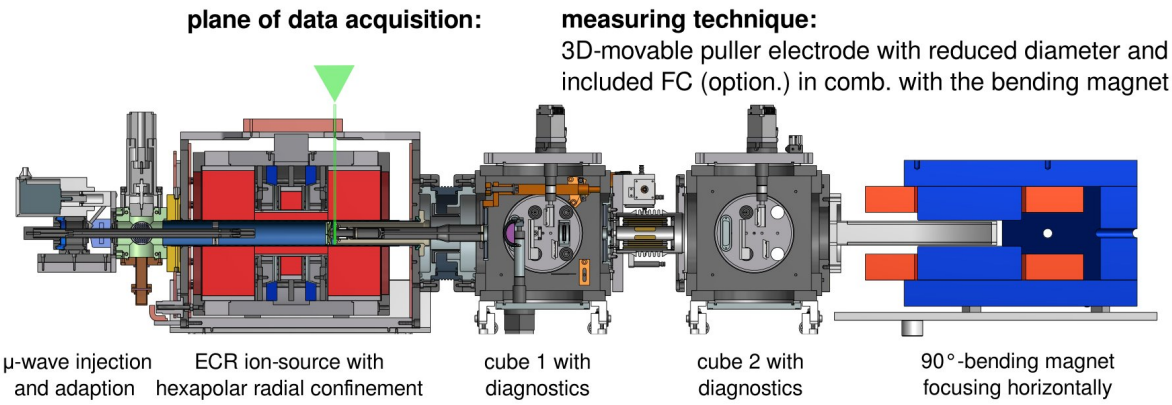

MOTIVATION:

The second investigation regarding the distribution of charged particles along the axis of an ECR ion source was performed at much closer vicinity of the plasma than the previous one. Here, several beam profiles were recorded only 15 mm downstream of the plasma electrode (for reference see the plane marked in green in the figure above). To acquire the beam profiles under that difficult conditions (very limited space, strong magnetic fields, surrounding high voltage) the 3D-movable puller electrode was modified to work as a device capable of beam-profile acquisition itself: its aperture was reduced to 0.5 mm to gain spatial resolution and a customized FC was developed. That FC could optionally be inserted into the puller electrode to record the extracted currents. If not inserted, the extracted beam passes the bending magnet for m/q-analysis. The aperture of the plasma electrode was sampled using that modified puller electrode. The measurements yielded the spatial distribution of the various ion-species and the current-density distribution in the plane 15 mm downstream the plasma electrode. From these results, both corresponding distributions in the plane of the plasma electrode were deduced.

NEW EXPERIMENTAL INSIGHTS:

The various ion species in ECR ion sources are arranged in bloated triangles with the same orientation but different sizes in the plane of the plasma electrode. The size of each triangle depends inversely on the charge state. The current density of each charge state increases towards the center of the plasma electrode. Here, the highest current density is observed.

Spatially resolved charge-state and current-density distributions at the extraction of an electron cyclotron resonance ion source

Lauri Panitzsch,[a] Thies Peleikis, Michael Stalder, and Robert F. Wimmer-Schweingruber
Institute for Experimental and Applied Physics (IEAP), Christian-Albrechts-Universität, Kiel, Germany

(Received 24 June 2011; accepted 20 August 2011; published online 26 September 2011)

In this paper we present our measurements of charge-state and current-density distributions performed in very close vicinity (15 mm) of the extraction of our hexapole geometry electron cyclotron resonance ion source. We achieved a relatively high spatial resolution reducing the aperture of our 3D-movable extraction (puller) electrode to a diameter of only 0.5 mm. Thus, we are able to limit the source of the extracted ion beam to a very small region of the plasma electrode's hole (Ø = 4 mm) and therefore to a very small region of the neutral plasma sheath. The information about the charge-state distribution and the current density in the plane of the plasma electrode at each particular position is conserved in the ion beam. We determined the total current density distribution at a fixed coaxial distance of only 15 mm to the plasma electrode by remotely moving the small-aperture puller electrode which contained a dedicated Faraday cup (FC) across the aperture of the plasma electrode. In a second measurement we removed the FC and recorded m/q-spectra for the different positions using a sector magnet. From our results we can deduce that different ion charge-states can be grouped into bloated triangles of different sizes and same orientation at the extraction with the current density peaking at centre. This confirms observations from other groups based on simulations and emittance measurements. We present our measurements in detail and discuss possible systematic errors. © *2011 American Institute of Physics*. [doi:10.1063/1.3637462]

I. INTRODUCTION

Already in the design phase of a future electron cyclotron resonance ion source (ECRIS) extensive computer simulations are performed to find a setup permitting the achievement of the desired source parameters such as achievable charge state, extractable current, and beam emittance at the extraction. For good beam transmissivity, especially the last parameter, namely the beam emittance at the extraction, is of great importance and serves as an input parameter for subsequent beam line design optimization calculations. Therefore, emittance measurements have been performed and benchmarked against simulations.[1–3] From these emittance measurements some knowledge about the spatial charge-state distribution (CSD) of the particular beam in the plane of the extraction can be deduced but no precise information can be gained. The CSDs deduced from experiments in general match the simulation results which show higher charge states peaking closer to the beam axis than the lower charged ion species.[2,4] But in addition, some simulations also show another interesting feature. If the source is operated with a hexapole for radial plasma confinement, the simulated distributions show that the different charge states are arranged in characteristically shaped triangular stars.[3–7] This property cannot be deduced from the emittance measurements. To make it visible spatially resolved charge-state measurements are required. The current-density distribution (CDD) of ion beams is usually recorded using scintillation screens or wire scanners. As reported in Ref. 8, our Faraday cup array (FCA)-detector can also be used to obtain an accurate profile of the beam in absolute values. All these measuring techniques lead to the same conclusion that (for a reasonably well focussed beam) the current density peaks at the centre. This is generally believed to be the case already at the extraction. To our knowledge there are no measurements of the CDD or the CSD at the extraction.

Therefore, we have performed two different types of measurements at our ECRIS. From these measurements we were able to deduce both, the CSD (for charge states 2+ to 4+) and the CDD directly at the extraction and spatially resolved. The key enabling technology for these measurements is a 3D-movable extraction (puller) electrode, which is also movable in the plane perpendicular to the beam line. It has a tiny aperture (Ø = 0.5 mm) and can optionally be equipped with a small Faraday cup (FC) inside. This allows us to record spatially resolved CDDs. We obtain spatially resolved CSDs by removing the FC and recording m/q-spectra of the extracted beam. The ability to move the puller electrode remotely without venting the source enables us to keep the time for the data acquisition comparatively short (≈ 30 min for the CDDs and ≈2 h for the CSDs). The source runs stable over such time scales.

In Secs. II–VI we describe our measurements and summarize our results.

II. MEASUREMENTS – GENERAL CONSIDERATIONS AND SETUP

Our aim is to determine both the spatially resolved CDD and the spatially resolved CSD at the plasma electrode for the same source settings. This allows correlating CSD and CDD. To reach high spatial resolution we fix the distance from the slit (Ø = 0.5 mm) inside the puller electrode to the plasma

[a]Electronic mail: panitzsch@physik.uni-kiel.de.

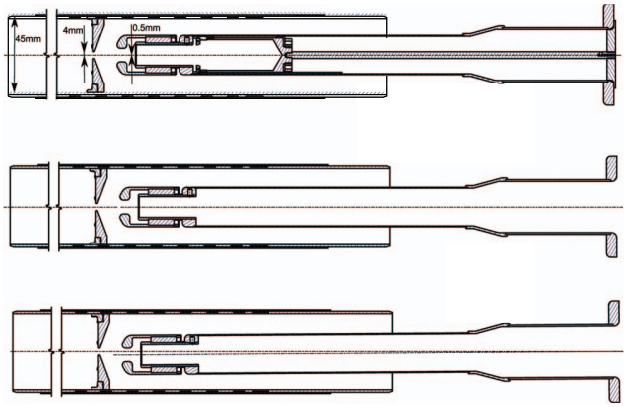

FIG. 1. Computer aided design drawings of the plasma chamber, the plasma electrode, and the puller electrode for different settings: (1) central with implemented FC, (2) central without FC, (3) at the outmost position without the FC.

electrode (Ø = 4.0 mm) to the closest achievable distance (15 mm). To determine the CSD it is of great importance to have good transmissivity from the slit inside the puller electrode into the sector magnet to avoid systematic errors. For both measurements it is absolutely necessary to limit the extracted beam to a small region of the plasma electrode. As will be pointed out (see Secs. IV E and IV G for transmissivity, and Sec. III B for limited extraction) both requirements are met in our case.

The Kiel ECRIS beam line is briefly described in Ref. 9 (see Fig. 2 in that paper). To precisely describe the situation (including the dimensions and positions of the single parts) at the extraction we start with a view on a drawing of our puller electrode (see Fig. 1). In this figure we present the plasma tube (inner diameter = 45 mm), the plasma electrode (diameter of the aperture = 4.0 mm), and the movable puller electrode (slit diameter = 0.5 mm). In the first row the puller electrode is at central position with the FC implemented. The setting with implemented FC is used to determine the CDDs. The geometrical dimensions of the FC and the use of a negatively biased repeller guarantee the suppression of secondary electron escape. In the second row we see the same situation but without the implemented FC. This setting is used to record the CSDs. In the third row, again the FC is removed but the puller electrode is set to its outermost position. Here the puller electrode is tilted by 0.4°. The resulting shift is 2 mm.

Before starting our measurements we optimized source parameters for high transmissivity by recording and maximizing a set of two parameters while increasing the acceleration voltage:

1. We measured the beam profile at the ion-optical object plane of the sector magnet which is at a distance of 0.6 m from the plasma electrode. The beam profile needed to be as focussed as possible.
2. We determined the number of different charge states as well as their intensity in the recorded spectra. Both needed to be as high as possible.

For this measurement the FC was of course removed from the puller electrode. Analyzing the results we found an extraction voltage of about 7 kV to be a good setting. Here, the profile was well focussed and the intensity of the peaks in the spectrum was comparatively high. At central position we found all possible ion species (namely N and O in all charge states) within the spectrum which underlines a well chosen focussing. Increasing this voltage did not improve the recorded parameters significantly. We aimed to keep the voltage as low as possible to avoid discharges from the puller electrode to the walls of the plasma chamber for non-central positions of the puller electrode. Therefore we chose an extraction voltage of 7 kV for all the following measurements. The injected microwave power was set to 50 W. To see how a change of the ion composition and the pressure inside the electron cyclotron resonance (ECR) zone influences the results of our CSD- and CDD-measurements, we varied both parameters (pressure and ion composition) by adding helium into the plasma chamber and repeating the measurements. The first measurements were performed at a residual gas pressure of 5×10^{-7} mbar inside the plasma chamber. In the following paragraphs we will call this setting RG. For the second measurement we added helium until the pressure reached 1×10^{-6} mbar (we will call this setting RGHe).

III. SPATIALLY RESOLVED CDD

To record the spatially resolved CDD, we used the puller electrode with reduced aperture and included FC. For the two different settings (RG and RGHe) we have moved the puller electrode in the plane perpendicular to the beam line and recorded the ion current hitting the FC for different positions. Again, the coaxial distance from the plasma electrode to the slit inside the puller electrode was fixed to 15 mm. The resulting distributions are shown in Fig. 2. The figures show the CDD for both settings (RG (left) and RGHe(right)) in the plane of the plasma electrode at comparatively high resolution. The x- and y-axes denote the position in the plane of the plasma electrode with the origin being at beam centre. The colour bars indicate the measured current densities.

Analyzing the results two points are of great interest (A and B):

A. Current distribution

There is a clear distribution in the electrical current density. It can be affirmed that the highest currents are present in the centre. In addition we observe that current densities with similar intensity are grouped into bloated triangular-like structures with different orientations and sizes. At this point we are not yet able to determine the composition of these triangles, but in Sec. V we will combine these results with results from the CSD measurements and observed sputter marks. We will show that each of these triangular structures is dominated by ions of one m/q-ratio and that their orientation is equal directly at the extraction as predicted by simulations performed by other groups.[3–7]

B. Circular plasma electrode

The nearly circular shape of the plasma electrode is clearly visible and its diameter can be verified to be 4 mm. The reason for not having a “perfect” circular shape is

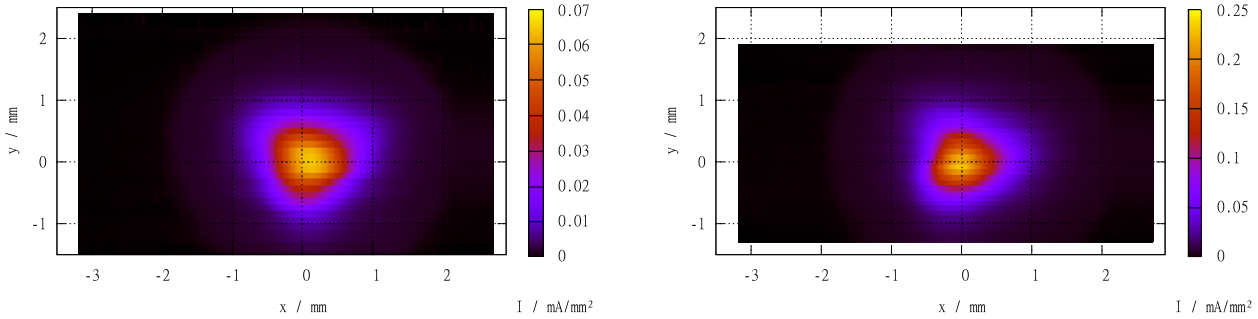

FIG. 2. (Color online) Measured current density distributions shortly behind the plasma electrode for setting RG (left) and setting RGHe (right). Note that the colour bars are scaled differently to match the particular intensity range.

supposed to lie in the uncertainties in the end-position switch of the stepper motor driving the puller electrode in horizontal direction and also triggering the start signal of the current recordings. The ability to clearly resolve the circular shape of the plasma electrode as well as the triangular structures in the CDD measurements indicates that the ions passing through the tiny aperture are indeed extracted from a very limited region of the neutral plasma sheath only. If the ions were extracted from larger regions the resulting figures would be blurred and we would not be able to clearly resolve structures like these. Herewith, the first criterion to successfully perform these measurements (that the extracted beam needs to be limited to a very small region of the plasma electrode to achieve good spatial resolution) is validated.

IV. SPATIALLY RESOLVED CSD

To determine the spatially resolved CSD we used the puller electrode with reduced diameter (but without the FC) and a sector magnet which is installed in our beam line. We moved the puller electrode in the plane perpendicular to the beam line at the constant and short distance as in the previous paragraph (15 mm from the plasma electrode to the slit inside the puller electrode) and analyzed the beams extracted from the different regions of the plasma electrodes aperture (and therefore the neutral plasma sheath). The thus obtained spatial distributions for the most dominant ion species (N and O) are presented in Fig. 3 for setting RG (residual gas only) and in Fig. 4 for setting RGHe (with additional helium), respectively. We have to point out that these distributions are strongly influenced by the transmissivity of the particular charge states. The key parameter for the transmissivity is the extraction voltage defining the focussing of the different beam components. The results shown here have to be regarded as a "snapshot" looked at from behind the sector magnet for the applied focussing only. Nevertheless, some information gained from these measurements is crucial to draw the conclusions presented in Sec. V. This will be described more in detail in that section.

The left-hand columns of Figs. 3 and 4 show the spatial distributions for the different nitrogen charge states. The displayed charge states range from 1+ to 4+ because all higher charge states were only found at the exactly central position (and therefore are not shown). The right-hand columns show the same distributions for oxygen. Here also, charge states higher than 4+ were found only at the exactly central position and therefore are also not displayed separately. The intensities in the individual plots are scaled to the maximum measured intensity, Imax. This clearly brings out the spatial distribution of the individual charge-state beams. Imax is indicated at the top of the individual plots and increases from low to high charge states. In both settings (RG and RGHe) the highest charge states only fill the central pixel and therefore are confined to the very central region of the plasma electrode. The oxygen distribution is not quite as peaked as that of nitrogen which is consistent with the overall m/q tendency. With decreasing charge the distribution broadens and nearly fills the plasma aperture for doubly charged ions. Obviously the highest charge states clearly peak in the centre while lower charge states populate areas with larger radii around the centre. In addition we point out seven important aspects (A-G):

A. Current distribution

For the current distribution we see an overall tendency for the different charge states of both ion species. The recorded current densities peak at the centre and decline with increasing radial distance. The slope of the decline is distinctly steeper for more highly charged ions and more shallow for the lower charged species.

B. Comparison of settings RG and RGHe

Comparing the distributions of the single ion species in both settings (RG and RGHe) shows that the distributions are not significantly altered by these different source parameters. This shows that the distributions can be reproduced even when helium as a mixing gas is added. The addition of helium results in a significantly increased extracted flux of more highly charged ions (as can be seen comparing Figs. 3 and 4 and as summarized in Fig. 5). According to Ref. 10 the differently charged ions originate from different longitudinal locations inside the plasma chamber. Higher charged ion species are supposed to originate from regions closer to the (central) back side of the source. Tracing back the magnetic field lines from these locations of particle "generation" defines the beam diameter at the extraction for the particular ion species. Applying this to our results would lead to the

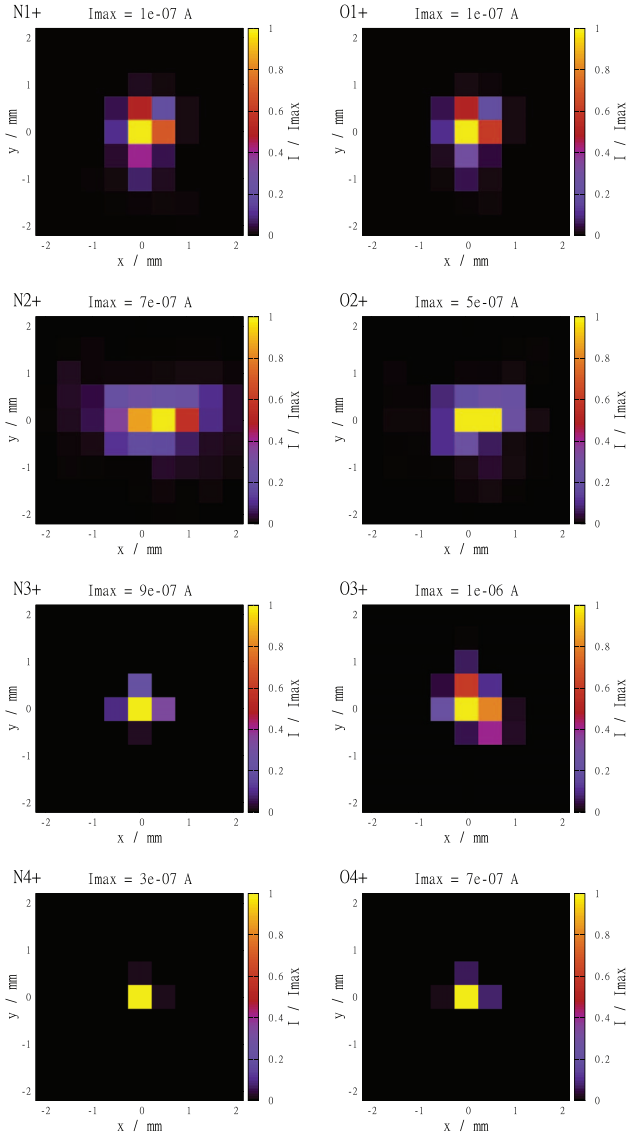

FIG. 3. (Color online) Measured charge state distributions at the plasma electrode as visible from behind the sector magnet for setting RG (residual gas only). The x- and y-axes denote the position in the plane of the plasma electrode with the origin being at beam centre. The colours show the measured current densities scaled to the maximum detected current, Imax, for each graph. This allows visualization of the entire distribution.

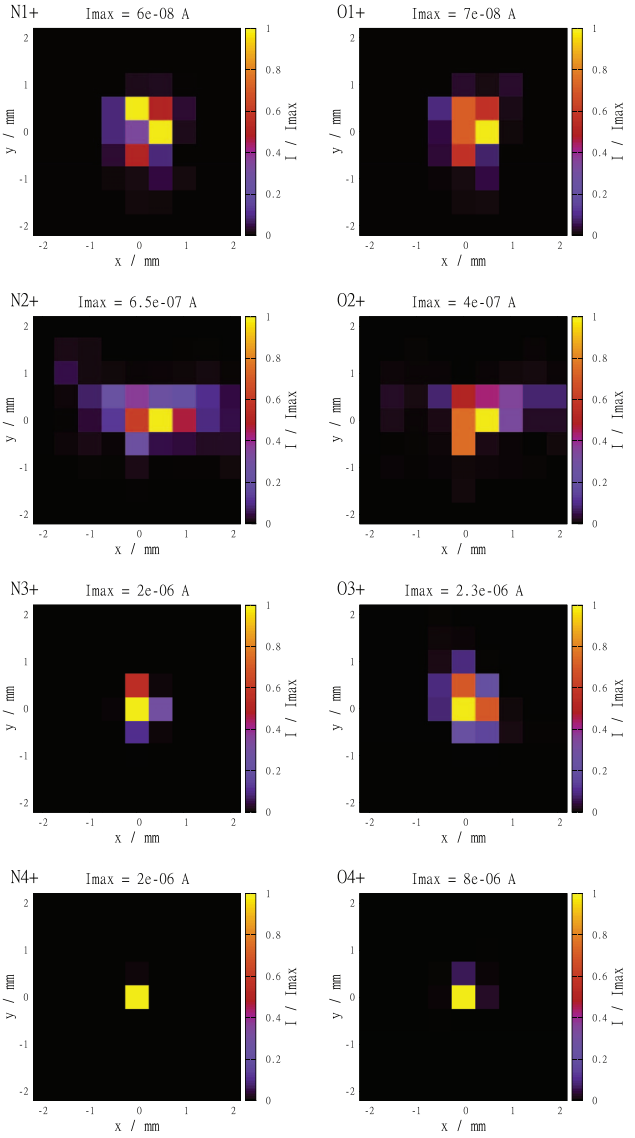

FIG. 4. (Color online) Measured charge state distributions at the plasma electrode as visible from behind the sector magnet for setting RGHe (residual gas and helium). See Fig. 3 for caption.

conclusion that (since the spatial distribution did not change significantly) the particular regions for particle generation have not changed, but the generation efficiencies have.

C. Calculated total CSD

The total charge-resolved current over the whole area of the plasma electrode (using the puller electrode with reduced aperture for ion extraction) can be calculated by summing up the currents for each particular ion species. This results in a total CSD which is presented in Fig. 5. Here, the currents measured for the different charge states of nitrogen and oxygen are shown for both settings (RG and RGHe). The results will be discussed shortly in Subsection IV D.

D. Gas mixing

The effect of gas mixing can be observed by comparing the calculated total CSDs for both settings (RG and RGHe, see Fig. 5). In the first setting (setting RG) the charge state with highest intensity was 2+. Measurements with the setting RGHe showed that the highest intensity was shifted to charge 3+ or 4+.

E. Transmissivity

In Sec. IV C (Fig. 5) we showed the calculated total CSDs from the single CSD measurements performed with the puller electrode with reduced aperture. In an additional measurement we have also recorded the total CSD for the same plasma parameters but using our standard-sized (Ø = 8 mm) puller electrode at central position. The results of both measurements are shown in Fig. 6 for setting RG. These

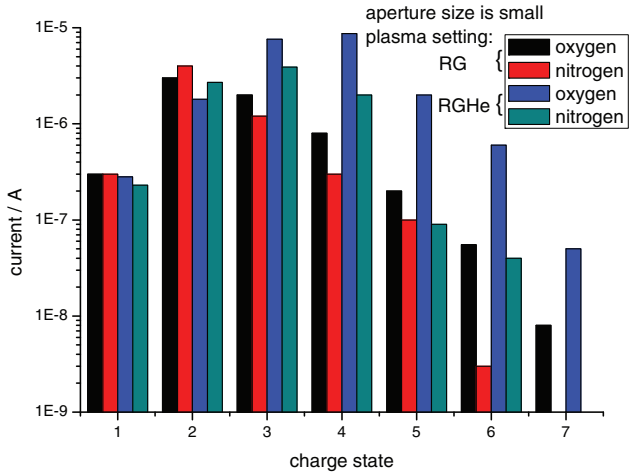

FIG. 5. (Color online) Comparison of the total charge state distributions for settings RG and RGHe. The distribution for the small sized aperture is calculated from the results of the CSD measurements by summing up the currents for each particular ion species. With helium as a mixing gas we see a shift of the maximum ($2+ \rightarrow 3+$ or $4+$) in the total charge state distribution and an increase of all higher charge states.

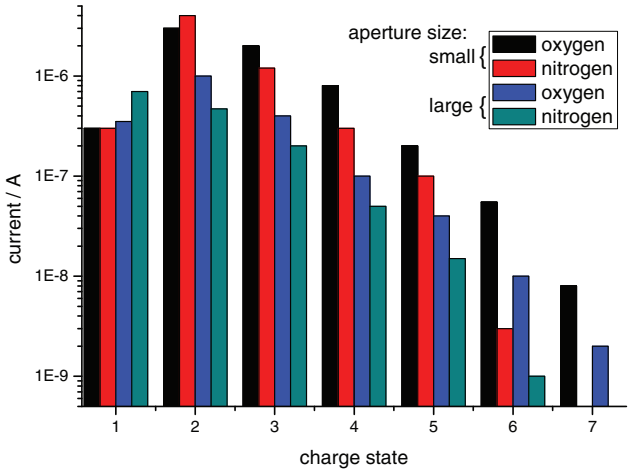

FIG. 6. (Color online) Comparison of the total charge state distributions for setting RG for a small and a standard sized (large, $\varnothing = 8$ mm) puller electrode. The distribution for the small sized aperture is calculated from the results of the CSD measurements (see Fig. 5). The distribution for the large aperture was recorded directly.

results can be used to check for good transmissivity. One can easily see that both distributions show same characteristics/trends. From this we can conclude that the relative transmissivity for all charge states is similar for both aperture sizes of the puller electrode. Therefore we can conclude that the transmissivity of the puller electrode with reduced aperture is comparable to that of the standard puller electrode. This we take as a proof for sufficiently high transmissivity. Another interesting fact is that the summed-up currents recorded with the puller electrode with reduced aperture are higher than the currents detected with the standard-sized puller electrode. This trend can be observed for all charge states higher than $1+$. Using the puller electrode with reduced aperture we extract the ions at many different positions and sum the currents up. Since geometrical effects can be excluded we believe this to be a "multi-aperture"-like effect. Multi-aperture extractions are known to result in significantly increased total currents.[11]

F. Triangular structures – low resolution

The existence of triangular structures at different positions along the beam line is well known and has been observed by many different groups. The appearance of these structures depends on the focussing. If the beam is strongly focussed this feature of the beam becomes visible in profile measurements. These triangular structures should already be present in the plane of the extraction. Moreover, simulations taking into account the magnetic field lines come to the conclusion that each single charge state should be distributed in a triangular shape already at the extraction.[3–7] Because of the still low resolution the CSD measurements presented here we cannot yet provide conclusive evidence for these structures. Nevertheless, we aim to demonstrate the following. Figure 2 shows the high resolution CDD at the extraction and we can clearly see triangular structures for both settings. However, it is not visible in the CSDs (compare Figs. 3 and 4) though they were recorded under same source settings. Their spatial resolution is simply far too low (120 times lower). We have artificially reduced the resolution of the measured positions of the CDD in Fig. 2 to that of the CSD measurements and present them in Fig. 7. We see that within these figures one cannot resolve the triangular structures anymore (though it was possible before) which demonstrates that the low resolution of the CSD measurements prevents the direct detection of triangular structures.

G. Sum of the spatially resolved currents (calculated CDD)

In Sec. III we have presented measurements of the CDD at the plasma electrode (see Fig. 2). As described in Sec. IV F we artificially lowered the resolution of the CDD measurements to adapt it to the resolution of the CSD measurements. The resulting CDDs (with adapted/reduced resolution) are shown in Fig. 7. Here, we show the CDDs calculated from the results of the CSD measurements. They were obtained by summing up the currents for all the measured ion species in the beam (namely N, O, and He in all charge states) at their particular positions. These calculated CDDs are shown in Fig. 8. They can be compared to those recalculated from the CDD measurements (Fig. 7) to check for consistency. The structures in both figures show same tendencies and the main characteristics are preserved. In both figures the effective total radii decrease from setting RG to RGHe. The centres of the structures are shifted slightly rightwards (+x direction). Only the background of Fig. 7 which has an intensity of only $\approx 1\%$ (displayed in dark purple) is not present in Fig. 8. Since this is only a background with very low intensity we do not see this as an exclusionary argument and we state that the structures are well reproduced. Also the currents in Figs. 7 and 8 are in the same range. From the ratio of both maximal currents (0.045/0.07 and 0.175/0.25) we can estimate the

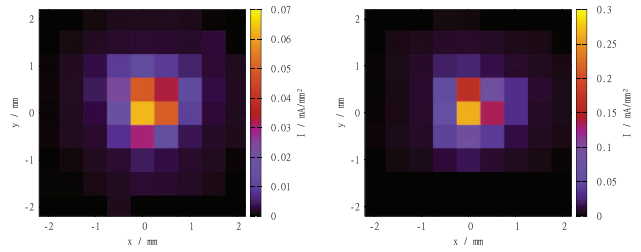

FIG. 7. (Color online) Current density distributions at the plasma electrode for setting RG (left) and setting RGHe (right) calculated from the CDD measurements. The original spatial resolution (compare Fig. 2) is adapted to match the spatial resolution of the CSD measurements (see Figs. 3 and 4).

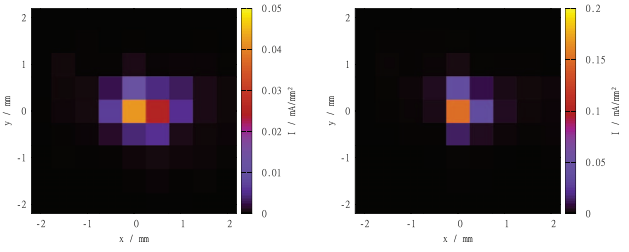

FIG. 8. (Color online) Current density distributions at the plasma electrode for setting RG (left) and setting RGHe (right) calculated from the spatially resolved CSD measurements.

transmissivity to be ≈70% for the actual focussing. The currents shown in Fig. 7 can be regarded as lossless since they were measured with the FC installed directly inside the puller electrode. This we take as a second hint for good transmissivity (starting at the slit inside the puller electrode passing through the sector magnet into a FC).

V. ANALYSIS OF THE PREVIOUS RESULTS

In this section we combine the results of the CSD measurements with the results of the CDD measurements. From that we are able to deduce the distribution of the ions directly at the extraction. We begin with a short discussion of systematic errors and the validity:

A. Validity and systematic errors

The CDDs are recorded using a FC inside the puller electrode. This results in a very short drift distance for the ion beam. For geometrical reasons the aperture size of the puller electrode in combination with the inner diameter of the FC guarantee the capture of the total beam passing the aperture. The use of a repeller in front of the FC restricts secondary electrons from escape. A magnetic field-induced rotation has to be considered but generally we can exclude systematic errors for the CDD measurements. For the results of the CSD measurements we observed a relatively high transmissivity (70%, see Sec. IV G) and a comparatively good consistency with the CDD measurements (Figs. 7 and 8) which we take as a reference. Though, we have to point out limited validity for the results of the CSD measurements. The presented CSDs portray only a "snapshot" for the current focussing settings. They can be regarded as source regions of the plasma electrode for the different ion species effectively transmitted through the sector magnet under the particular focussing settings. A change in the extraction voltage (the only ion-optical element besides the sector magnet) will change the presented distributions. Therefore the calculated total CSDs (Fig. 5) represent only the ion species that are transmitted through the sector magnet. They do not represent the real totally extracted CSD which we are interested in for our analyses in Sec. V B. We know that the transmissivities for the standard and the tiny-sized apertures of the puller electrode are nearly identical (Fig. 6). Thus, we have determined multiple total CSDs for beams extracted with the large puller electrode while varying the extraction voltage. The spectra show that the main trends (especially the dominating ion species) within the recorded total CSDs do not differ significantly within the checked voltage range (4 kV to 11 kV) from these shown in Fig. 5 (for 7 kV). Accordingly, we use the total CSDs already mentioned in Sec. IV C (Fig. 5) for the subsequent argumentation.

B. Conclusion of the results

In Sec. III (Fig. 2) the current density distribution in close vicinity of the extraction is shown. Here, triangular structures of different sizes and orientations are clearly visible but no information about the ionic composition of these structures can be gained. To solve this we consult the results obtained in Sec. III (Fig. 5). For our analysis we start with the blue structure of setting RG shown in Fig. 2 (left). This structure has a certain orientation and fills out a comparatively large area. The analysis of the total CSD (see Fig. 5) indicates that for setting RG the most dominant ion species are charged 2+ and 3+ with the 2+ component being slightly more dominant. The singly-charged ions are too strongly suppressed to contribute significantly. Since the ion species charged 3+ has lower intensity and should (according to the theory) fill out a smaller area it is supposed to be embedded within the structure created by the 2+ charged ions. Therefore we conclude that the blue structure of Fig. 2 of setting RG (left) is dominated by the 2+ ion component.

The central (red) structure of Fig. 2 (left, setting RG) with higher intensity has the same orientation as the blue structure. This we take as a hint that it is also dominated by ions charged 2+. The increased intensity results from the fact that the current density of each charge state peaks at the centre (see Sec. IV A). Another secondary effect may also be an additional superposition of higher charge states peaking at the centre. This effect we estimate to be less significant due to the dominance of 2+ and 3+ in the current intensities as seen in the total CSD (see Fig. 5).

For the blue structure of setting RGHe (see Fig. 2, right) two facts stand out. It is rotated compared to that of setting RG and its size appears to have decreased slightly. In analogy to the considerations of setting RG we suspect this blue structure to be dominated by ions of charge state 3+. These ions contribute to the dominant species for setting RGHe (see Fig. 5).

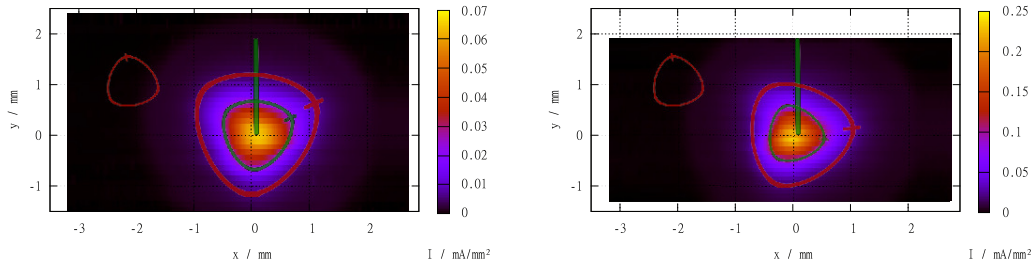

FIG. 9. (Color online) Measured CDD for settings RG and RGHe (compare caption of Fig. 2 for details). Here the detected structures are framed with marked bloated triangles to guide the eyes. The triangle in the upper left corner displays the orientation of the magnetic field (triangle) directly at the extraction as proved by sputter marks on the inner side of the plasma electrode (see Fig. 10).

The inner (red) structure of setting RGHe (Fig. 2, right) shows a different orientation (further rotation). Together with the information from the total CSD and due to its decreased size we believe this structure to be dominated by the intense 4+ component (again, see Fig. 5).

To guide the eyes we have framed the measured structures of Fig. 2 by bloated triangles. These plotted triangles have a mark to distinguish their orientation and are presented together with the already introduced structures (Fig. 2) in Fig. 9. With this aid it is possible to determine the angle of rotation of the different structures. Extracting the beam in a region where the axial magnetic field peaks at roughly 1 T a rotation is induced on a beam of charged particles. Knowing the axial magnetic field configuration B_z the magnetically induced rotation of the beam Θ_{tot} can be calculated with the formula,[12]

$$\Theta_{tot} = \sqrt{\frac{q}{8mU_{extr}}} \cdot \int B_z dz \qquad (1)$$

with q, m, and U being the charge, the mass, and the extraction voltage, respectively. The rotation of the beam that occurs after having passed the tiny aperture of the puller electrode does not affect the CDD measurements since all ions passing the aperture at its defined position will be collected by the FC.

The information gained so far about the structures is summarized in Table I. For each resolved structure we denote the estimated dominating charge state as well as the observed orientation in relation to the green line pointing upwards in Fig. 9 (which denotes 0°). We have simplified the identification of the observed orientation by drawing bloated triangles to guide the eye in Fig. 9. In an additional column we line out the expected ("calculated") rotation for the different charge states that can be calculated by using formula (1). The original orientation is given as the difference of both values and can be regarded as the orientation in the plane of the plasma electrode. We see that the orientation for all structures calculated back directly to the extraction shows roughly the same value (13°). This means that all triangular structures are oriented in the same direction at the extraction. This is further corroborated by the sputter marks observed at the inner side of the plasma electrode as shown in Fig. 10. They also show an orientation of ≈13° counter clockwise. Thus, our measurements support the simulations of various groups who have predicted this behaviour.[3–7] This can be seen as a strong positive evidence for the assumption that the different structures are dominated by different charge states each.

TABLE I. Summary of the information gained from the previous analyses. The observed orientation and the original orientation are given in relation to the green line which denotes 0°. The original orientation is calculated as the difference of the observed orientation minus the calculated rotation.

Considered structure	Suspected charge state	Calculated rotation	Observed orientation	Original orientation
RG blue	2+	−78°	−65°	+13°
RG red	2+	−78°	−65°	+13°
RGHe blue	3+	−95°	−81°	+14°
RGHe red	4+	−110°	−97°	+13°

VI. CONCLUSIONS

Having analyzed the probability of systematic errors we were able to deduce the CDD and the CSD directly at the extraction of a hexapole geometry ECR ion source in comparatively high resolution. The results clearly show higher currents peaking in the centre as well as the presence of (bloated) triangular structures.

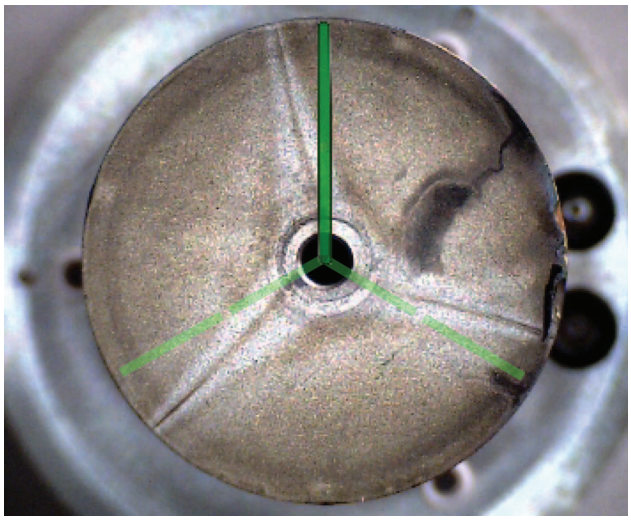

FIG. 10. (Color online) Sputter marks observed on the inner side of the plasma electrode. The tilt angle is ≈13° counter clockwise in relation to the vertical plane. This is in good agreement with the values for the original orientations calculated in Table I.

Each of these structures is populated by ions of the same charge state. At the extraction all the structures are orientated in the same direction determined by the orientation of the magnetic field. The surface area of these structures differs from comparatively large for low charged ions and decreases rapidly for more highly charged ions. The higher/highest charge states clearly peak only in the centre and therefore populate the smallest effective radii. The reason why the observed structures resemble bloated triangles instead of sharp ones lies in the comparatively small aperture size of our plasma electrode. It reduces the accessible part of the sharp star formed by the magnetic field lines (see Fig. 10) to the bellied central region.

This is to our knowledge the first direct measurement of the CSD and the CDD at the extraction. The results in general conform to results from simulations and facts deduced from emittance measurements, both performed by other groups. To determine the spatially resolved plasma potential in future measurements one could use the same extraction technique (reduced aperture size) in combination with a retarding field grid in front of a FC shortly behind the puller electrode.

[1]D. Wutte, M. A. Leitner, and C. M. Lyneis, Phys. Scr. **2001**, 247 (2001).
[2]M. Leitner, C. Wutte, and C. M. Lyneis, in *Proceedings of Particle Accelerator Conference, Chicago, IL, USA, IEEE*, (2001).
[3]D. Winklehner, D. Todd, J. Benitez, M. Strohmeier, D. Grote, and D. Leitner, J. Instrum. **5**, P12001 (2010).
[4]L. Maunoury, C. Pierret, and J. Pacquet, in *Proceedings of ECRIS08 18th International Workshop on ECR Ion Sources*, Chicago, IL, USA (2008), pp. 224–228.
[5]D. S. Todd, D. Leitner, M. Leitner, C. M. Lyneis, J. Qiang, and D. P. Grote, Rev. Sci. Instrum. **77**, 03A338 (2006).
[6]C. Pierret, L. Maunoury, S. Biri, J. Y. Pacquet, O. Tuske, and O. Delferriere, Rev. Sci. Instrum. **79**, 02B703 (2008).
[7]J. P. M. Beijers and V. Mironov, Rev. Sci. Instrum. **81**, 02A307 (2010).
[8]L. Panitzsch, M. Stalder, and R. Wimmer-Schweingruber, Rev. Sci. Instrum. **80**, 113302 (2009).
[9]L. Panitzsch, M. Stalder, and R. F. Wimmer-Schweingruber, Rev. Sci. Instrum. **82**, 033302 (2011).
[10]P. Spädtke, K. Tinschert, R. Lang, J. Mäder, J. Roßbach, J. W. Stetson, and L. Celona, Rev. Sci. Instrum. **79**, 02B716 (2008).
[11]R. Geller, *Electron Cyclotron Resonance Ion Sources and ECR Plasmas* (Institute of Physics, University of Reading, Berkshire, 1996).
[12]W. Glaser, *Grundlagen der Elektronenoptik* (Wien, Bristol, UK, 1952).

NEXT REFERRED PUBLICATION: OWN CONTRIBUTION: approx. 80%

CURRENT DENSITY DISTRIBUTIONS AND SPUTTER MARKS IN ELECTRON CYCLOTRON RESONANCE ION SOURCES Lauri Panitzsch, Thies Peleikis, Stephan Böttcher, Michael Stalder, and Robert F. Wimmer-Schweingruber, accepted for publication in Rev. Sci. Instrum.

MEASURING TECHNIQUE AND POSITION OF DATA ACQUISITION:

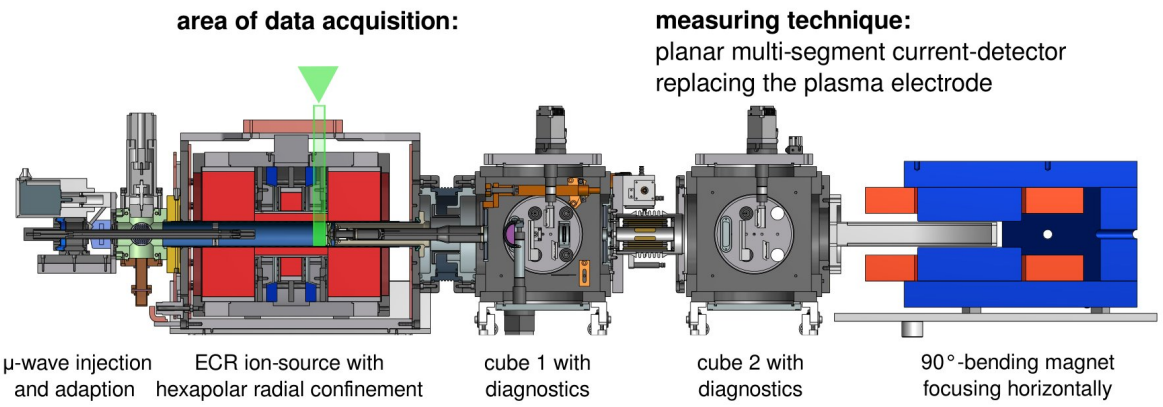

MOTIVATION:

The third investigation regarding the distribution of charged particles along the axis of an ECR ion source was performed inside the plasma chamber close to the plasma electrode (referring to the area marked in green in the figure above). At this position, several challenges have to be coped with: to work under high vacuum, to be strongly limited in space, to withstand the interaction with the plasma, and to deal with strong magnetic fields and high voltages. For that purpose, a planar multi-segment current-detector was developed to replace the plasma electrode. It was mounted via a carrier onto the (in this case only axially) movable puller electrode to reach regions even closer to the central plasma. Using this technique, the current-density distribution inside the plasma chamber close to the plasma electrode was measured while differentiating between ions and electrons. For the read-out of the signals the electronics developed for the FCA (see the first publication for reference) was used as it offers a 44-channel ampere-meter for both polarities with independently adaptable current ranges for each channel.

NEW EXPERIMENTAL INSIGHTS:

The electrons inside the plasma chamber are strongly connected to the magnetic field lines and therefore spatially well confined in triangular-shaped structures. Their intensity increases towards the center of the plasma electrode. The electrons seem responsible for the thin sputter marks inside the plasma chamber. The electrons are surrounded by less intense and spatially less confined ion populations that seem to account for the broad sputter marks.

Current density distributions and sputter marks in electron cyclotron resonance ion sources

Lauri Panitzsch,[a] Thies Peleikis, Stephan Böttcher, Michael Stalder, and Robert F. Wimmer-Schweingruber
Institute for Experimental and Applied Physics (IEAP), Christian-Albrechts-Universität zu Kiel, Germany

(Received 12 September 2012; accepted 16 December 2012; published online 14 January 2013)

Most electron cyclotron resonance ion sources use hexapolar magnetic fields for the radial confinement of the plasma. The geometry of this magnetic structure is then—induced by charged particles—mapped onto the inner side of the plasma electrode via sputtering and deposition. The resulting structures usually show two different patterns: a sharp triangular one in the central region which in some cases is even sputtered deep into the material (referred to as thin groove or sharp structure), and a blurred but still triangular-like one in the surroundings (referred to as broad halo). Therefore, both patterns seem to have different sources. To investigate their origins we replaced the standard plasma electrode by a custom-built plasma electrode acting as a planar, multi-segment current-detector. For different biased disc voltages, detector positions, and source biases (referred to the detector) we measured the electrical current density distributions in the plane of the plasma electrode. The results show a strong and sharply confined electron population with triangular shape surrounded by less intense and spatially less confined ions. Observed sputter- and deposition marks are related to the analysis of the results. Our measurements suggest that the two different patterns (thin and broad) indeed originate from different particle populations. The thin structures seem to be caused by the hot electron population while the broad marks seem to stem from the medium to highly charged ions. In this paper we present our measurements together with theoretical considerations and substantiate the conclusions drawn above. The validity of these results is also discussed. © *2013 American Institute of Physics*. [http://dx.doi.org/10.1063/1.4774052]

I. INTRODUCTION

Hexapolar magnetic fields are used in many ECRIS to confine the plasma radially. The triangular symmetry is conserved in the beam and can be seen under adequate beam focusing. This symmetry can also be found inside the source where the plasma loss areas are mapped onto the chamber walls. The processes involved are deposition and sputtering. In many sources[1,2] deeply sputtered triangular shapes can be found at the extraction and the biased disc. These sharp structures are surrounded by a broader halo. There are different theories about the origin of both structures based on simulation results. According to Mironov and Beijers, the sharp, sputtered structures originate from low-charge, hot ions which are desorbed as neutrals from the plasma chamber wall.[3] In contrast, Spädtke *et al.* propose the ions generated close to the axis to cause the thin grooves and the broader halo to result from ions connected to the magnetic stray field.[1] Our measurements presented in this paper prove that there also is (as found in various simulations) a strong and peaked electron contribution which we believe to be the reason for the thin sputter marks. To probe the current density distribution upon the plasma electrode we replaced it by a planar, multi-segment current-detector. We recorded the currents as a function of the biased disc voltage and for different axial positions as described in Sec. III. The energies of the impinging particles were roughly determined by biasing the source referred to the detector (Langmuir probe-like measurement, see Sec. IV for details). In Secs. II–VI we describe our measurements and summarize our results. It is important to note that our plasma electrode and biased disc do not (yet?) show any thin and deeply sputtered areas. This might be due to the limited injected microwave power (below 50 W). Nevertheless, we believe that our investigations provide useful insights regarding the identification of the sources of these patterns, because this lack might even be advantageous for the analysis, as discussed below.

II. GENERAL CONSIDERATIONS AND DETECTOR DESIGN

For our measurements we replace the full-metal plasma electrode by a custom-built multi-segment current-detector. As we want to determine the properties of the standard operational plasma conditions at the plasma electrode, we aim to keep the changes of the experimental conditions induced by the probe as small as possible. Therefore, one aspect is of major importance: The plasma loss areas need to terminate on electrically conductive surfaces. Using electrically conductive and virtually grounded areas for current-sensing this requirement is fulfilled for the most part of the detector as described below. We use our 44-channel ampere-meter with adaptable current ranges[4,5] for the current acquisition which we usually use for beam profile measurements. This leads to 44 different sensitive areas. We decided to arrange them as shown in Figure 1. Using this arrangement we are able to probe one of the triangular branches (or rays) in detail (marked "A"

[a]Electronic mail: panitzsch@physik.uni-kiel.de.

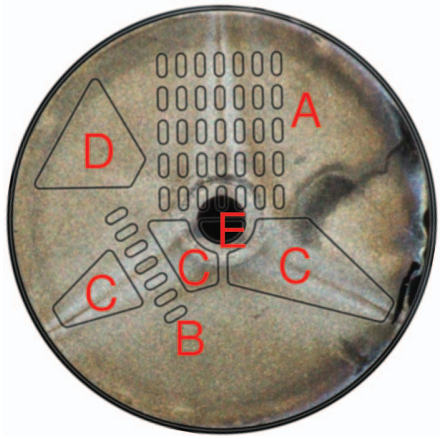

FIG. 1. Plasma electrode (⊘ = 45 mm) with typical sputter and deposition marks. The black marks indicate the grid of the planar multi-segment current-detector. Deeply sputtered areas and azimuthal deviations are not found. Areas referred to in the text are marked as follows: A = fine grid for spatial resolution; B = reference row for cross-checks; C = large areas; D = area outside the triangle; E = semicircle, barely visible here, see Figure 2 or 7 for reference.

in Figure 1). One second branch has a reference-row "B" at medium radial distance. It was designed to verify the results of the first branch assuming triangular symmetry. The large areas "C" enable us to measure the total current per branch though their main purpose is to ensure electrically conductive plasma loss areas. One of the large areas is located outside the plasma loss areas to probe for currents within these regions "D." The semicircle in the center "E" is used to apply a negative voltage simulating the electrical field applied for ion extraction under usual operating conditions. For the assembly of the detector we used a MACOR®-disc with the segmented pattern milled into it. Each segment/bin has a via hole for a wire connected from behind. The bins are filled with an electrically conductive and thermally resistant silver-epoxy glue that also is vacuum-proof to a certain extent. We have to point out that only the milled pattern (schematically shown in Figure 1) provides electrically conductive plasma loss areas. In-between these sensitive areas the plasma interacts with the bare MACOR®. We take this change in the experimental conditions as acceptable. To have the detector movable in axial direction we mounted it via a carrier to the puller electrode that was not in use during these experiments (as we did not extract any ion beams). The carrier guarantees a proper orientation of the disc adapting it to the triangular symmetry of the magnetic fields. The setup of the hardware can be seen in Figure 2.

A. Plasma parameters

For the benefit of getting these measurements into a context with prior investigations[6] we operate the source under similar conditions: residual gas at a pressure of about 2E-6 mbar and a microwave frequency of 11 GHz at an injected power of 30 W. The confining magnetic fields were identical. In the investigations cited above we were able to demonstrate by experiment that the different charge states at the plasma electrode are arranged in a triangular (star-shaped) symmetry with same the orientation each, and that the higher charge states are more concentrated along the axis.

B. Sputtering and deposition

For the following analysis we need to distinguish between sputtering (desorption of the target material induced by the incoming particle) and deposition (absorption of the incoming ion; electrons not sputtering the material only lead to an electrical current but no surface modification). Sputtering of the solid plasma electrode can generally be evoked by both ions and electrons under specific conditions. In the case of electron-induced sputtering of solids the electrons require a kinetic energy in the range of 100 keV for light target materials increasing up to 200–300 keV for elements with a higher atomic number[7] (see Table II in that reference). Assuming a bi-Maxwellian energy-distribution of the electrons a certain fraction of the electrons in high-performance sources can hold that high energies. At lower energies the electrons are absorbed by the target material. If the sputtering is induced by impinging ions these ions need to have a kinetic energy of at least 20–40 eV (depending on the surface binding energy of the target and the particle's mass ratio). This value represents the threshold energy for ion-induced sputtering.[8] At lower energies no sputtering can occur but deposition is observed. Increasing the incoming ion's energy to multiple tens of eV the sputtering yield can be strongly increased (see Figure 3 in that reference). This leads to the separation scheme for sputtering and deposition of ions and electrons as indicated in Table I.

As the ions in an ECRIS plasma are usually treated as cold (about 1 eV) their initial energy is far too low for

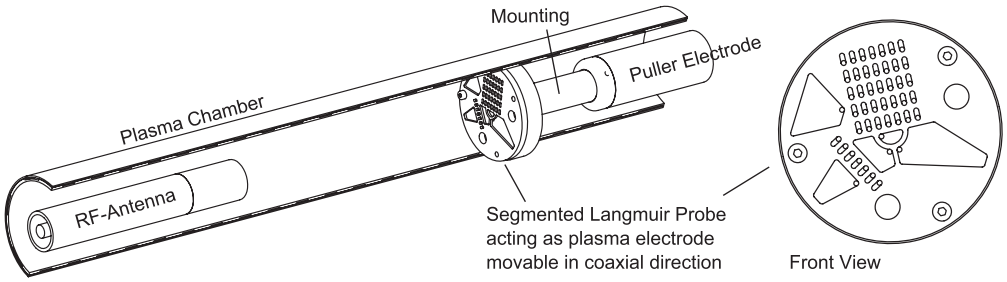

FIG. 2. Computer-aided design (CAD) view of the planar multi-segment current-detector installed into the ion source. This detector replaces the plasma electrode during these investigations. As it is attached to the movable puller electrode its position can be changed to determine the current distribution as a function of the detector's position.

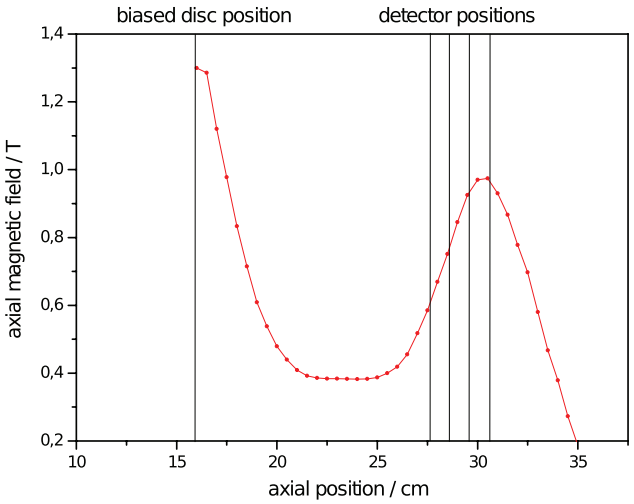

FIG. 3. Axial magnetic field of the source. The position of the biased disc and different axial detector positions (marked from 1 to 4) are presented.

sputtering. Ions moving towards the plasma electrode (which is usually at the same potential V_{Source} as the plasma chamber walls being our reference-potential) can be accelerated outwards by the plasma potential V_{Plasma} (usually a few tens of V).[3,9] This effect also takes place in the opposite direction towards the injection. Here, usually a biased disc is installed at a negative voltage V_{Disc} referred to V_{Source}, further increasing the energy gain of the impinging ions. We can conclude that the energy gain of the ions traveling to the extraction (or the injection) is V_{Plasma} (or $V_{Plasma} - V_{Disc}$, respectively) times their charge state q. For ion sources with a comparably high plasma potential and a charge-state distribution (CSD) peaking at the medium to highly-charged ions the resulting energy of a (large) fraction of the ions hitting onto the biased disc or the plasma electrode exceeds the energy threshold for ion sputtering. Then, only the lower charged ions contribute to deposition. The influence of V_{Disc} or V_{Plasma} on the energies of the electrons capable of sputtering is negligible as the threshold lies in the 200 keV-range. Here, other parameters are of importance which are not the subject of our investigation.

III. MEASURED CURRENT DENSITY DISTRIBUTIONS

The measurements were performed at different axial positions of the detector (see Figure 3) at different bias voltages V_{Disc} of the biased disc. We kept the detector (by which we mean the sensitive metalized areas of the detector) at the same potential as the source V_{Source} to simulate standard operation. The central semicircle was biased to 70 V lower than the sensitive areas to simulate the extraction field. This value was chosen as our measuring electronics provides this voltage at an extremely low noise level. The electrical field is effectively screened by the plasma in the boundaries over short distances and was observed not to influence the results significantly. Also, as we did not extract ion beams the resulting shape of the neutral plasma sheath was not of importance. During these measurements both, ions and electrons including secondary particles (mainly electrons) contribute to the measured currents. The resulting current density distributions in the plane of the plasma electrode (standard position: 30.6 cm) and at three additional axial positions closer to the plasma are shown as a function of the biased disc voltage V_{Disc} in Figure 4. The recorded currents dominated by electron impact (negative currents) are scaled in blue, the ion-dominated currents (positive currents) are scaled in red. To show the total dynamic range the distributions are scaled logarithmically. A short discussion of systematical errors is given after the analysis of the measurements.

TABLE I. Energy threshold for sputtering for ions and electrons. (According to Refs. 7 and 8.)

Particle	Energy threshold for sputtering
Ions	≈40 eV
Electrons	≈200 keV

First of all, we observe, in Figure 4, a strongly-confined triangular-shaped electron contribution which only peaks in the central region and is spatially even more concentrated along the branches of the triangle. This is visible as a general tendency under all analyzed conditions. The intensity of the electron contribution is more than one order of magnitude higher than that of the ionic contribution. The spatially strongly-limited electron fluxes are even high enough to exceed the total surrounding ion currents at all large areas (areas marked "C" in Figure 1 with the left ones divided by the reference row "B" and the right one). The electrons are surrounded by far less intense ion currents. The reference row shows triangular symmetry just as the detected currents reproduce the values of the central (3rd) row of the fine pattern "A" very well. As a second general tendency we observe the currents to increase approaching the ECR zone. The currents recorded in the area outside of the triangular symmetry are caused by ions but only the lowest fluxes were measured. In this color-scaling showing the whole current range, the differences between the various biased disc settings are not well distinguishable. As the pressure and the injected microwave power were not completely constant during these measurements and the biased disc was not exactly axially aligned we take these measurements as a qualitative but representative result for the ion- and electron distributions. In summary, multiple plasma parameters have been changed during these investigations always resulting in the same detected particle distributions: a strong and triangular-shaped electron contribution is well confined by the magnetic field and is surrounded by less intense and spatially less confined ion populations. Therefore, the results presented here claim general validity (in ECR ion sources with hexapolar radial confinement) and do in principle not depend on the exact plasma parameters. Nevertheless, some differences are seen. When applying a negative voltage to the biased disc, the negative currents in the central region slightly increase which is a hint for a higher electron density. For a biased disc at source potential the ion fluxes are somewhat increased. To emphasize this we show one distribution for both settings in a linear scale for the out-most position (z = 30.6 cm) in Figure 5. The systematic errors of these

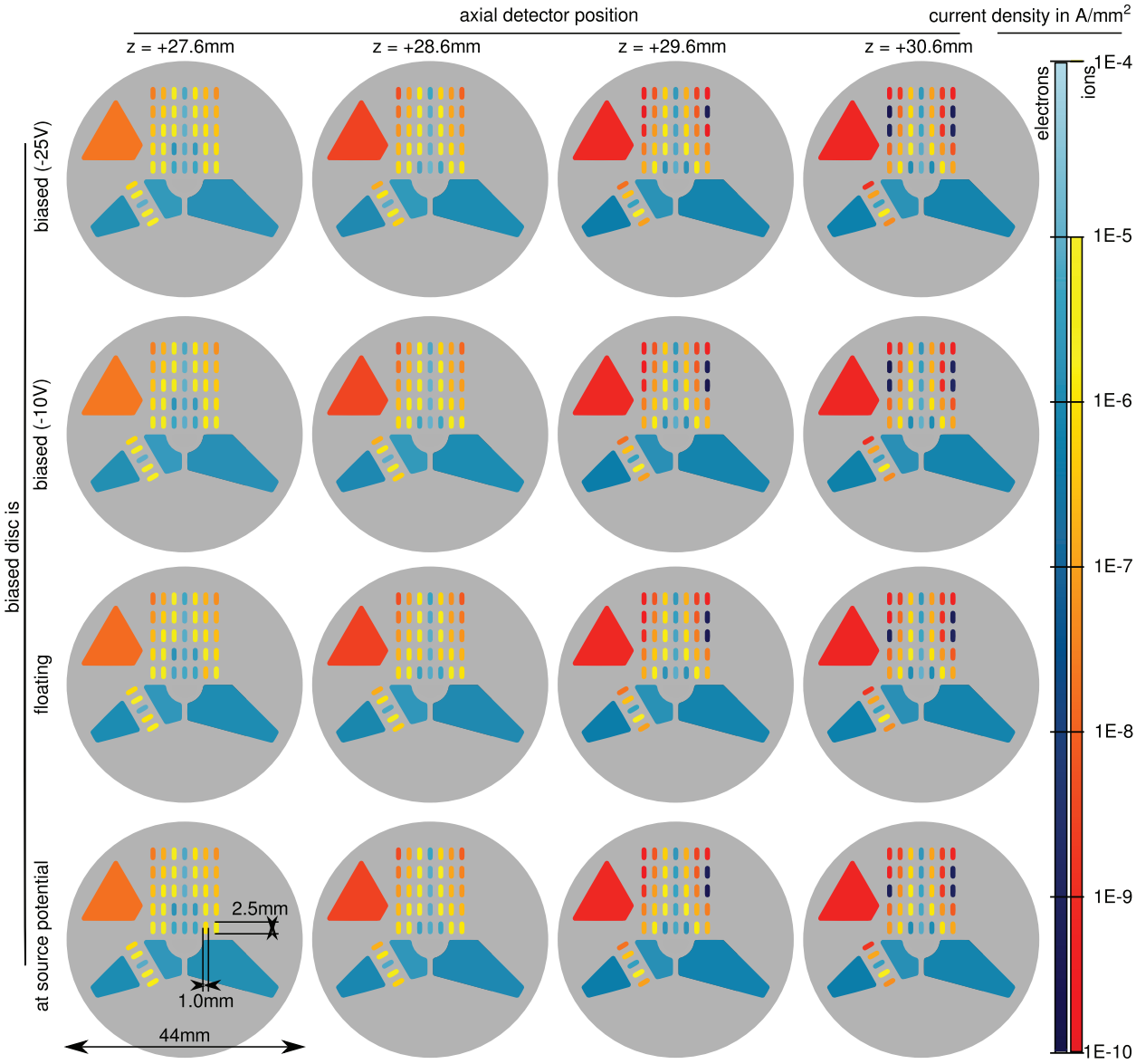

FIG. 4. Current density distribution recorded in the plane of the plasma electrode (z = 30.6 cm) and at three additional axial positions at different biased disc voltages V_{Disc}. Currents resulting from electrons are scaled in blue (negative), the ion-dominated components are scaled in red (positive, see scaling). To show the total dynamic range the scaling is logarithmic. A strongly-confined triangular-shaped electron contribution surrounded by far less intense and spatially less confined ion fluxes is observed as a general tendency.

measurements as well as their influence on the results is discussed briefly:

- electron- and ion-induced currents partly neutralize each other
- ion-induced currents can be amplified by secondary electron emission
- electron-induced currents can be attenuated by secondary electron emission
- as the ions can be multiply charged their particle flux is (compared to the electrons) overestimated by their mean charge state q

In conclusion, the true ion- and electron currents are expected to be even higher. Especially in the central parts of each branch there surely is an ionic component which is exceeded by the electron flux that dominates. Also, as the attenuation for negative currents (electrons) is more efficient, distinctly more electrons are supposed to hit the surfaces than represented by the measured negative currents. Thus, the spatial distribution of the electrons might even be more peaked than detectable with this detectors resolution (pad-width is 1 mm). The only spatially resolved measurement of the electron distribution in the plane of the plasma electrode we found in the literature was performed by Kenéz *et al.*[10] The results agree well.

IV. BIASED-SOURCE MEASUREMENTS

In a second measurement we bias the source to different positive and negative potentials, again recording the currents.

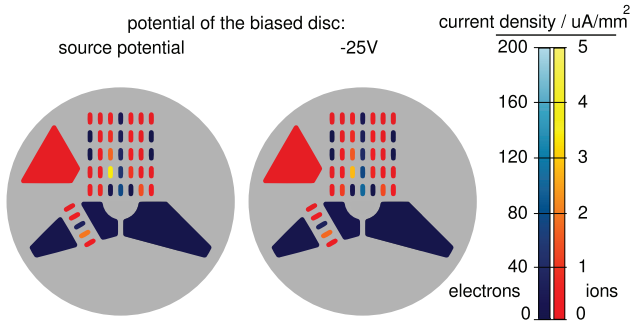

FIG. 5. Current density distributions for different biased disc voltages at the plasma electrodes standard position (z = 30.6 cm) in linear scale. A negative bias voltage results in slightly increased negative (electron) currents, at source potential the positive (ion) currents are increased. The increase lies in the range of about 25% in both cases.

This brings the grounded detector to variable (inverse) potentials referred to the source. For positive source voltages the detector is on negative potential referred to the source and vice versa. This measuring technique resembles a planar Langmuir-probe measurement. Using this technique we can repel the ions or a fraction of the electrons, respectively, thus obtaining an estimate for their energies. The measurements were performed at the out-most position (+30.6 mm, see Figure 3 for reference). The results are shown in Figure 6. For negative source voltages we observe rapidly increasing negative currents which saturate at a voltage of about −20 V. This can be explained as follows: At voltages close to zero ions and electrons are neutralizing each other in parts. For increasing negative source voltages V_{Source} the "positively biased" detector (referred to the source) repels the ions more efficiently resulting in less current neutralization and higher (negative) electron currents recorded. Therewith we get an estimate for the energy of the ions (imposed by the plasma potential) which is within the expected range. In the inverse case (source biased positively) the start conditions are equal. With increasing positive voltages of the source the detector repels an increasing fraction of the electrons. But here, we do not observe saturation which is a hint for much higher electron energies. These are two important findings we use for our argumentation in Sec. VII.

V. SPUTTER MARK ANALYSIS

During source operation we observed sputtering and deposition at both, the extraction and the injection. The resulting marks are shown in Figure 7 and will be discussed within this section.

A. The detector

Figure 7 (leftmost) shows the detector after about 10 h of operation. Apart from a proper azimuthal adjustment of the detector (the azimuthal adjustment was even better during the measurements reported in Secs. III and IV, but unfortunately it was slightly misadjusted before the long-term runs to increase deposition- and sputter marks) we observe comparatively strong depositions. These depositions are visible on the sensitive areas (that were always virtually kept on source potential via the measuring electronics) as well as on the spaces (insulator) in-between these areas. Only the central area biased negatively to simulate the extracting field is sputtered relatively bare. We take this as a hint that in our case the combination of plasma potential and CSD (which means $V_{Plasma} \cdot q$) results in a large fraction of ions energetically below the threshold for ion sputtering (≈40 eV) in the regions off-axis. We can draw that conclusion only for the positions off-axis as the central area of the detector was biased. Here, the ions were further accelerated and their energies exceeded the threshold and obviously sputtering occurred. Figure 7 (medium left) shows the central part of the detector enlarged. This figure proves that only in the central area (biased semicircle "E," which is bare) the sputtering processes seem to exceed the deposition rates. In the regions off-axis deposition seems dominant.

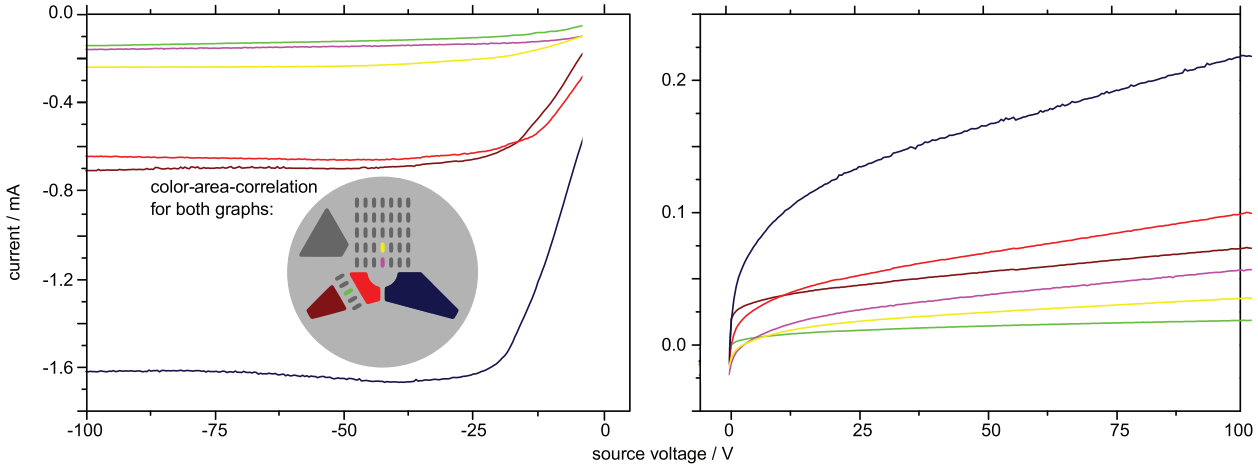

FIG. 6. Results of the biased-source measurements (planar Langmuir probe-like measurements). The recorded currents of a few representative areas are shown as a function of the bias voltage of the source referred to the detector for both polarities. The areas and the corresponding curves have the same color. For a certain voltage all ions can be repelled while this is not possible for the more-energetic electrons at inverted polarity.

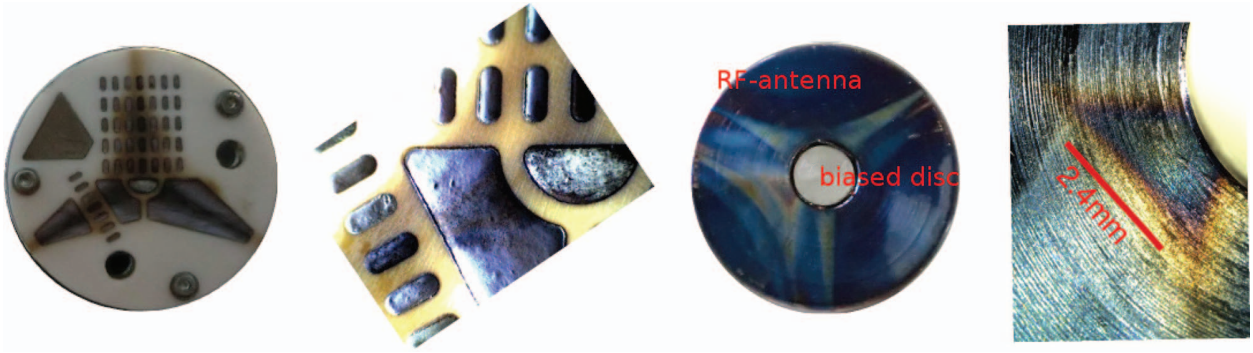

FIG. 7. Leftmost: Picture of the detector after about 10 h of operation at the position of the plasma electrode (z = 30.6 cm, see Figure 3 for reference). We see a proper adjustment of the detector as well as distinct deposition marks (dark colorations) on the sensitive areas and the spaces (the insulator) in-between. The areas were virtually kept at source potential. Only the central area (biased to −70 V referred to V_{Source}) shows a surface modification induced by sputtering. Medium left: Enlargement of the central region of the detector. Medium right: Picture of the RF-antenna with integrated biased disc. The axial position of this surface is shown in Figure 3 (biased disc position). The antenna itself (the outer ring) was always at source potential and shows different colorations of triangular symmetry induced by sputtering and/or deposition next to slight radial misadjustments. The central part (the bare circle) was mostly biased to different negative voltages and shows a clean and bare surface which was sputtered. No preferred direction or symmetry is observable in the clean area. The multiple triangular structures result from variations in the azimuthal adjustments of the antenna for different runs. Rightmost: The enlarged section focuses on the axially centered part of the RF-antenna being exposed to the central plasma loss lines. No deepening of the surface can be observed but various colors are present and a slight elucidation of the center may be realized.

B. The RF-antenna

A similar behavior can be observed at the injection side (see Figure 7, medium right). Here, slight radial misadjustments of the RF-antenna with included biased disc provide additional valuable information: Due to the slight misadjustment the biased disc was partly off-axis and the center of the axial plasma loss area hit the tip of the RF-antenna which was always at source potential (no additional acceleration occurred!). Again, we recognize the triangular structure imposed by the magnetic fields and we see different colorations (apart from the blue) which stem from a combination of sputtering and deposition. The center of the triangular structure is slightly lighter than the rest as shown in detail in Figure 7 (rightmost). This brightening we interpret as an increased sputter rate. In contrast to the off-axis areas, the sputter rate seems higher at the regions close to the source axis. Sputtering limited to these central areas can be explained by the strong and spatially peaked presence of highly charged ions (HCIs) near the source axis.[2,3,6,11,12] As the energy of the ions increases with their charge state, the HCIs seem to gain enough energy (accelerated by the plasma potential) to overcome the threshold and are able to sputter even without additional biasing. In high-performance sources this effect is even more dominant. However, it should be pointed out that all the sputter- and deposition marks discussed here are fairly broad and in the range of the broad halos observed at other sources. Thin grooves are not found.

C. The biased disc

The bare biased disc on the other hand (made of iron to increase the local magnetic field, included into the RF-antenna as shown in Figure 7, medium right) was clearly sputtered as it is clean. The additional potential difference enabled the ions to overcome the threshold for sputtering and even pulled a remarkable part of the ions off-axis. The ions do not seem to be strongly connected to the magnetic field lines as no structure is visible and the sputtering seems homogeneous.

D. Sputter mark conclusions

We state that in well-performing ECR ion sources a certain ratio of the ions is able to sputter solids, if the plasma potential is high enough and/or the CSD peaks at sufficiently-high charge states to overcome the threshold energy. Ions with lower energies impinging onto the in- or extraction are deposited. Both processes result in a modification of the surface. From the measurements presented in Figure 4 and from the sputter/deposition marks shown in Figure 7 we find that the triangular ion distributions at both ends of the source are fairly broad and of about the same size than the broad halos observed in other ECRIS. This observation supports the widely accepted assumption that the ions are responsible for the creation of the broader halos. We agree (as discussed above) that especially the highly-charged ions accelerated by the plasma potential can easily exceed the threshold for ion-induced sputtering. We also agree that their spatial distribution is likely to be much more concentrated along the branches of the triangle than that of the lower-charged ions as yielded by simulations.[3] But if these highly-charged ions were responsible for the creation of the thin grooves observed in other ECRIS we would expect them also to establish in our source. But this is explicitly not the case. In our ECRIS these sharp marks have not been observed so far. The measurements presented in this publication yield a dominance of electrons by one or even two orders of magnitude (when referring to particle fluxes). In contrast to the ions these electrons are spatially much more concentrated. This is in particular true along the branches of the triangle as shown in Figure 4 (see the small pads colored blue). Therefore, if a fraction of these electrons holds energies higher than the threshold energy, these hot electrons are very plausible candidates to cause the thin grooves as their spatial distributions are similar. Reasonable values for the magnetic

field strength (B > 1 T) and the electron energy (high enough for sputtering; E = 200 keV) result in gyro-radii <1 mm. This value is in approximate accordance with the width of the sharp structures. As these sharp structures are not found in our source this would imply that even the hot electrons of our source are below that threshold energy. This will be investigated in Sec. VI.

VI. ELECTRON ENERGY ESTIMATIONS

As already reported we did not observe thin grooves on the biased disc or the plasma electrode of our source. As we think them to be caused by hot electrons (E $\gtrsim$ 200 keV) we have performed investigations to measure the electron-induced bremsstrahlung-spectrum to obtain an estimate of the energy distribution of the electrons. The results from other groups[13] show that the electron energy in high-performance sources exceeds a few hundreds of keV easily. For our investigations we used the x- and gamma-ray-sensitive dosimetry telescope DOSTEL[14] originally developed to measure dose rates. As the detector was developed for higher energies, the resolution in the 100 keV-region is somewhat limited. Therefore, we do not aim to present a high-resolution bremsstrahlung-spectrum. Instead, we intend to determine the higher-energetic tail of this distribution to understand if the electrons inside our source are energetic enough for sputtering. The detector was positioned close to source at the source axis and recorded the bremsstrahlung-spectrum during our investigations. As a result we obtain the count rates as a function of the energy deposit as presented in Figure 8. The black curve represents the distribution recorded while the source was in operation (the injected microwave power was 30 W). The red curve shows the natural background measured separately. In the energy range of the detected bremsstrahlung the probability of interaction is limited in a silicon-based detector. This results in the comparatively small count rates observed. On the other hand, in that energy region the dominant interaction process is the photoelectric effect. As a result, the total energy of the incoming (and interacting) photon is deposited in the detector. From these DOSTEL-measurements (see Figure 8 for the results) we get an estimate of about 100 keV for the highest electron energies. This value is still below the threshold for electron-induced sputtering. This we take as the reason why we do not find the thin grooves caused by hot electrons but only the broader structures/halos which are ion-induced. We expect the electron energy to increase when increasing the injected microwave power. Unfortunately, this is not possible with the current lead shielding which needs to be thickened before.

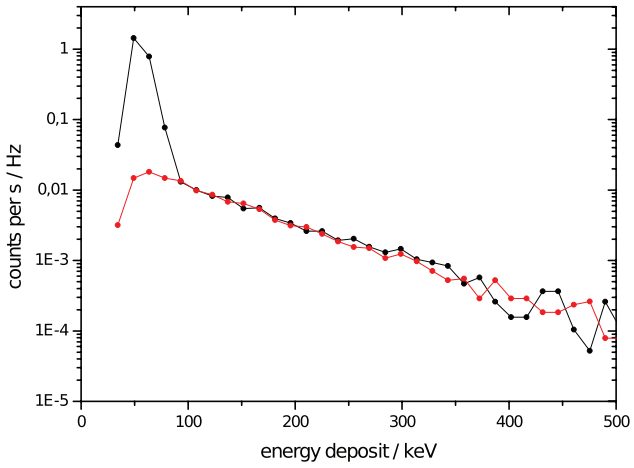

FIG. 8. Measured count rates as a function of the energy deposit in the detector recorded during these investigations on axis close to the source. The black curve represents the distribution recorded during source operation (30 W of injected microwave power) while the red curve shows the natural background measured separately. We get an estimate of about 100 keV for the highest electron energies for the reported source settings.

VII. CONCLUSIONS

Our measurements have shown that the electrons are distinctly the dominant particle population along the plasma loss lines defined by the magnetic fields. They are arranged in a sharply confined triangular-shaped structure over the whole radial distance from the axis to the plasma chamber walls. The electrons are surrounded by ion populations with a spatially far broader distribution. This is in accordance with the model that the electrons are strongly coupled to the magnetic fields and attract the ions by the resulting negative potential. The electron fluxes are one to two orders of magnitudes larger than the ion fluxes. We observe the currents to increase when approaching the ECR zone. From our Langmuir probe-like measurements we see the plasma potential to lie in the range of about 20 V at our source for the applied source settings. This is a reasonable value. Medium to highly-charged ions accelerated by that voltage are able to sputter. Ions with lower charge state will be deposited. Thus, if the HCIs were responsible for the creation of the thin grooves, these structures should establish in our source, but they do not. Due to the fairly broad spatial distribution of the ions showing the same spatial characteristics as the broad halo, we state that it is them (the ions) that cause the broad marks. We propose the spatially much more confined electrons to cause the thin grooves if their energy exceeds the threshold for the electron-induced sputtering of solids. Their spatial distribution resembles that of the thin grooves observed in other sources. The investigations performed on the bremsstrahlung spectrum showed a maximum energy of about 100 keV for the hot electrons in our source which is too small for electron-induced sputtering. This finding supports our presumption.

ACKNOWLEDGMENTS

The authors thank Dr. Sönke Burmeister for providing the DOSTEL data which was an important contribution for the analysis of the results. Special thanks also to Christiane Helmke for her technical and Stefan Kolbe for his engineering assistance.

[1]P. Spädtke, K. Tinschert, R. Lang, and R. Iannucci, AIP Conf. Proc. **749**, 47–54 (2005).

[2]D. Winklehner, D. Todd, J. Benitez, M. Strohmeier, D. Grote, and D. Leitner, J. Instrum. **5**, P12001 (2010).
[3]V. Mironov and J. P. M. Beijers, Phys. Rev. ST Accel. Beams **12**, 073501 (2009).
[4]L. Panitzsch, M. Stalder, and R. F. Wimmer-Schweingruber, Rev. Sci. Instrum. **80**, 113302 (2009).
[5]L. Panitzsch, S. Böttcher, M. Stalder, and R. F. Wimmer-Schweingruber, in *Beam Instrumentation Workshop 12*, edited by T. Satogata (Newport News, Virginia, USA, 2012).
[6]L. Panitzsch, T. Peleikis, M. Stalder, and R. F. Wimmer-Schweingruber, Rev. Sci. Instrum. **82**, 093302 (2011).
[7]R. Egerton, R. McLeod, F. Wang, and M. Malac, Ultramicroscopy **110**, 991 (2010).
[8]W. Eckstein, C. Garciá-Rosales, J. Roth, and J. László, Nucl. Instrum. Methods Phys. Res. B **83**, 95 (1993).
[9]O. Tarvainen, P. Suominen, and H. Koivisto, Rev. Sci. Instrum. **75**, 3138 (2004).
[10]L. Kenéz, J. Karácsony, A. Kitagawa, M. Muramatsu, S. Biri, and A. Valek, Publ. Astron. Dept. Eotvos Lorand Univ. **15**, 135 (2005).
[11]C. Pierret, L. Maunoury, S. Biri, J. Y. Pacquet, O. Tuske, and O. Delferriere, Rev. Sci. Instrum. **79**, 02B703 (2008).
[12]J. P. M. Beijers and V. Mironov, Rev. Sci. Instrum. **81**, 02A307 (2010).
[13]D. Leitner, J. Y. Benitez, C. M. Lyneis, D. S. Todd, T. Ropponen, J. Ropponen, H. Koivisto, and S. Gammino, Rev. Sci. Instrum. **79**, 033302 (2008).
[14]R. Beaujean, J. Kopp, S. Burmeister, F. Petersen, and G. Reitz, Radiat. Meas. **35**, 433 (2002).

8 COMPARISON: 3D-SIMULATIONS VS MEASUREMENTS

In this chapter, the computational results of two different simulation codes for plasma formation ([12] and [7, 5], as already referred to in the introduction) are compared to the experimental results and observations specified in the publications included in this thesis. The comparison is limited to the codes mentioned above as they are capable of calculating the solution in three dimensions without assuming radial symmetry. Besides the comparison, some fundamentals of the particular codes are mentioned in the corresponding sections below.

8.1 PIC-MCC CODE DEVELOPED AT KVI (NETHERLANDS)

At the Kernfysisch Versneller Instituut (KVI) Groningen, a Particle-In-Cell (PIC) Monte Carlo Collision (MCC) code [12] was developed to model the full 3D ion-dynamics in ECRIS plasmas. The simulations start with an equal number of neutral and singly-charged particles uniformly distributed over the whole plasma chamber. The electron energies obey a single Maxwell-Boltzmann distribution which is the main approximation in this code. The electron temperature is used as fitting parameter while the electron density is determined by the requirement of local charge neutrality. Therefore, no ion-confining electric fields ("potential dip") can evolve in the plasma. The code considers ion-ion and electron-ion collisions which account for electron-ion heating, ion-ion temperature equilibration, ion diffusion, and the ionization dynamics. The particles are allowed to evolve in space and charge state until a stationary solution is reached. The movement of the different ion species is tracked using a leapfrog particle mover. Particles that are lost from the plasma chamber as they pass the extraction aperture or collide with the chamber walls are re-entered as neutrals to keep the number of particles constant. From the results the 6D phase-space distributions (profiles and emittances) of the different ion species can be calculated in the plane of the extraction.

In this section, the results of the PIC-MCC code [12] are qualitatively compared to experimental observations gained at the ECR ion source in Kiel. The PhD-thesis of S. Saminathan [3] serves as the source of the simulation findings. In that work, the plasma formation adapted to the KVI-AECR ion source [34, 35] is modeled with the PIC-MCC code. Then, the beam extraction is simulated using GPT [9] and LORENTZ3D [10]. The simulations yield the beam profiles and emittances of different ion species in the plane of the plasma electrode and further downstream. The results have been benchmarked against measurements (presented in that thesis [3]) at two positions along the beam line: well behind the extraction and in the image plane of the bending magnet. A good agreement is observed.

Due to a lack of experimental data the regions closer to the extraction have not been evaluated so far. To overcome this limitation, we compare findings

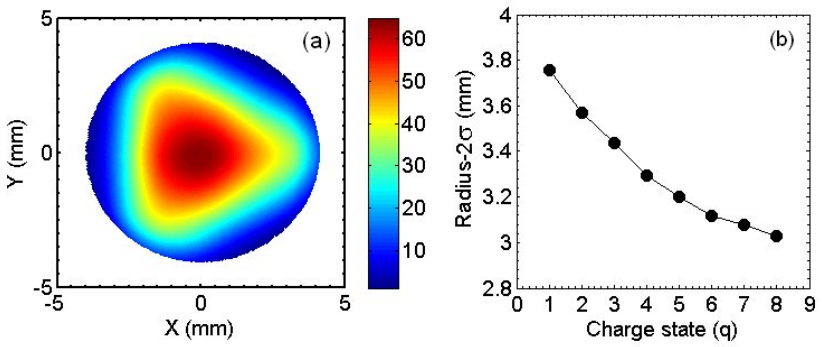

Figure 43: Calculated spatial distribution of Ne^+ ions at the aperture of the plasma (a) and effective beam radius (2 σ) for each charge state of the neon ions at the aperture of the plasma electrode (b). From [3], courtesy of Suresh Saminathan.

presented in chapters 6 and 7 of this thesis to the simulation results of [3]. As these experimental observations do not include explicit information about the momentum distribution (the emittance), the validation is limited to the spatial distribution of various charged particles (i.e. the beam profiles). Note, that only qualitative comparisons can be made as the experiments and the simulations were performed independently at different ion sources and with different plasma parameters. Nevertheless, as the basic principles (including the radial magnetic confinement) of these ion sources are not that different, the qualitative results are comparable.

Figure 43 (a) shows the calculated spatial distribution of Ne^+ ions at the aperture of the plasma electrode. Two facts stand out: The spatial arrangement resembles a slightly bloated triangle. Its intensity increases towards the center of the aperture. Figure 43 (b) shows the calculated effective beam radii for different charge states of the neon ions in the same plane. Clearly, the higher-charged ions are concentrated to smaller effective radii, or in other words, the effective beam radii depend inversely on the charge state.

All three phenomena (triangular structure, increasing intensity towards the center, and smaller effective radii for higher-charged ions) are in total accordance with the experimental observations reported in chapter 6 ([16], see figures 3, 4, and 9 in that publication). Going further into detail, the calculated results shown in figure 44 (a) are consulted. Here, the spatial distribution of the He^+ ion component in the plane of the plasma electrode but inside the plasma chamber in shown. The ions are arranged in a star-like structure, again with the intensity increasing towards the center.

Again, the findings of the simulations in principle agree well with the experimental results as presented in chapter 7 ([18], see figure 4 in that publication). It should be pointed out that the spatial distributions presented in that reference are plotted on a logarithmic scale with much lower spatial resolution (imposed by the detector hardware). Therefore, the width of each branch of the star-like structure appears much broader than presented in figure 44.

Figure 45 visualizes the simulated profile of a beam of multiple ion species (from Ne^{1+} to Ne^{8+}) behind the extraction system [3]. It shows that the shapes

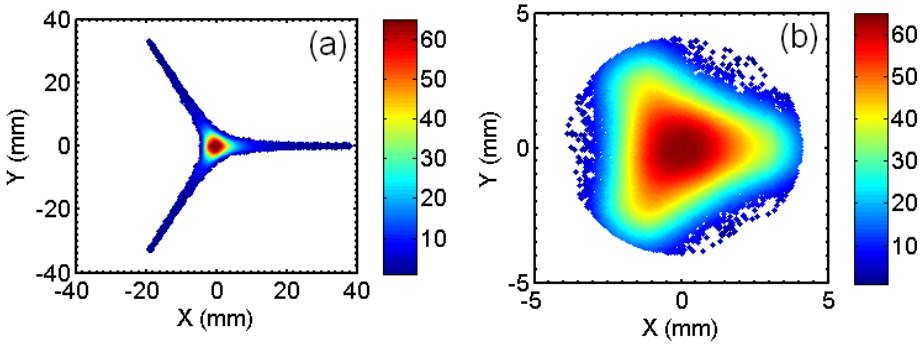

Figure 44: Calculated spatial distribution of He^+ at the plasma electrode (a) and through the aperture of the plasma aperture (b). From [3], courtesy of Suresh Saminathan.

of the different ion species are expected to still resemble bloated triangles but their orientation has changed. We are able to prove that simulation finding by experimental results presented in chapter 6 ([16], see figure 9 in that publication). Starting in the plane of the extraction with an identical orientation, the profiles of the various ion species (with different mass-per-charge ratios) are systematically rotated by the fringe field of the magnets by different angles. The angle of rotation can be calculated by a formula derived by Glaser [36] and is confirmed by our experimental observations presented in chapter 5 [17].

In conclusion, the PIC-MCC code developed at KVI seems to reproduce many important aspects of plasma formation in good agreement with experiments which is a great advance. This includes the regions close to the plasma electrode. According to the authors, the electron dynamics including RF-heating are planned to be incorporated to the code in a the next step. This will result in a more realistic description of the electron population parameters.

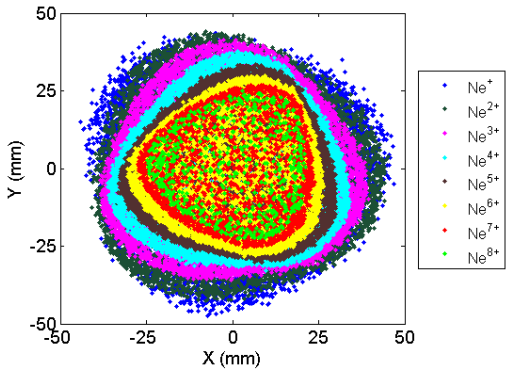

Figure 45: Calculated spatial distribution for a 90% space-charge compensated Ne^{q+} beam behind the extraction system. The various colors indicate the different charge states of the neon beam. From [3], courtesy of Suresh Saminathan.

8.2 HYBRID APPROACH DEVELOPED AT INFN-LNS (ITALY)

In order to simulate the 3D mechanisms of plasma formation and heating in ECR ion sources a hybrid approach [7, 5, 6, 4] has been developed at Instituto Nazionale di Fisica Nucleare, Laboratori Nazionali del Sud (INFN-LNS) in Italy. The term "hybrid" accentuates that the model differentiates between collisionless long-timescale phenomena (calculated by Particle-in-Cell (PIC) codes) and the collisional processes handled with a Monte Carlo (MC) code. By the use of single-particle and PIC simulations the motion of the electrons dominated by the injected electromagnetic waves and the present magnetostatic fields is determined. The advantage of this approach is that the heating of the electrons by electromagnetic modes excited in the plasma chamber (assumed as a circular resonant cavity) is modeled. Then, the electron and ion dynamics are calculated using the fields obtained by solving the Maxwell equations in a self-consistent way. At this stage the plasma is assumed to be collisionless which is a second assumption. The calculations lead to a preliminary spatial distribution of the plasma. Then, Coulomb-collisions are included and the dynamics of the ions and electrons is modeled with a Monte Carlo (MC) code in the presence of the self-generated electro-static fields yielded by the PIC simulations. The calculations result in the final spatial distribution of the plasma particles started from a homogeneous distribution. As ionization processes are not included yet, the CSD of the plasma is a necessary input parameter. Now we compare some of the simulation findings of that group with the experimental observations presented chapters 6 [16] and 7 [18].

Figure 46 shows the spatial distribution of different charge states of argon that were calculated for two different CSDs [4]. According to the findings presented in that figure, the higher-charged ions are concentrated closer to the center of

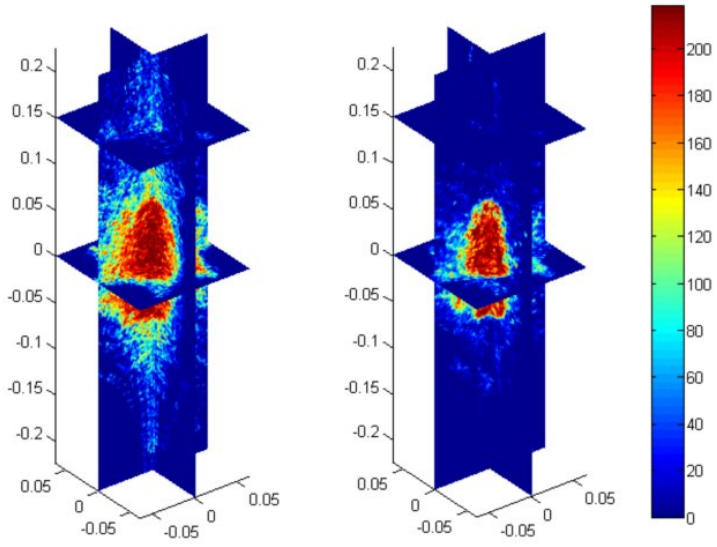

Figure 46: Comparison between simulated ion distributions (a.u.) for Ar plasma, with 1<q<4 (left), and 5<q<8 (right). From [4]

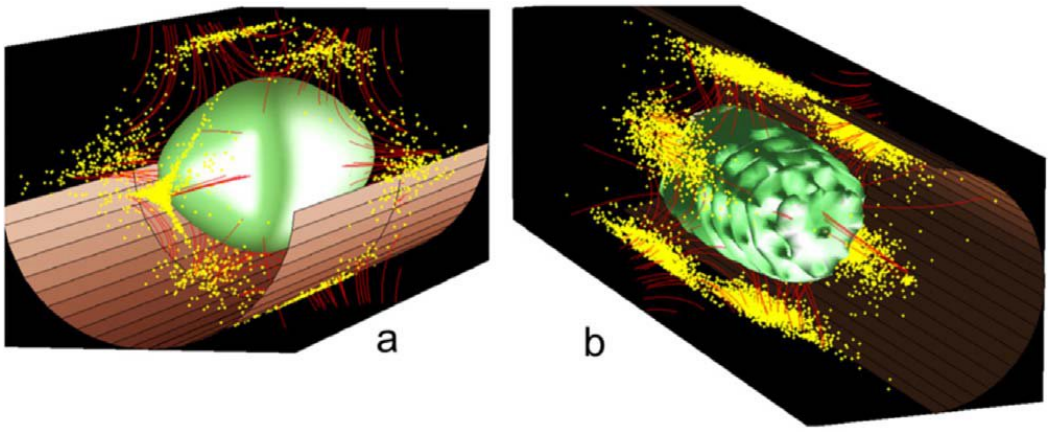

Figure 47: Ions (yellow dots) hitting the chamber walls in case of (a) smooth and (b) strongly corrugated isodensity surfaces. From [5]

the source than the lower-charged ion populations. This is in accordance with conclusions that have been drawn from ion-beam emittance analyses [37, 38, 39]. This finding also agrees with the simulation results referred to in the previous section [12, 3] and with the experimental results presented in chapter 6 of this thesis. As already pointed out, the effective radii of the extracted ion species inversely depend on the charge state. Thus, the higher-charged ions are extracted from smaller effective radii at the plasma electrode.

Another interesting result of that group is the spatial distribution of the ions and electrons inside the plasma chamber. These results are presented in figures 47 and 48.

In figure 47, the spatial distribution of the ions (not distinguishing between the various charge states or ion species) inside the plasma chamber is visualized. Figure 48 shows the electron's distribution. Both distributions show the same trends: The particles are arranged in a triangular-shaped structure (shown in

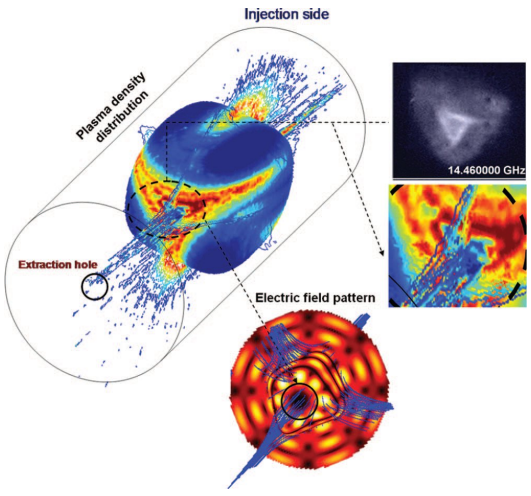

Figure 48: Three-dimensional electron density and pattern of electromagnetic field compared with the real shape of the extracted ion beam. From [6] Reprinted with permission from D. Mascali, S. Gammino, L. Celona, and G. Ciavola, Review of Scientific Instruments, 83, 02A336, 2012. Copyright 2012, American Institute of Physics.

yellow in figure 47) imposed by the radial magnetic fields. As both graphics originate from different publications, the orientations of the structures differ. If they were describing the situation in one source from the same point of view, their orientation would be identical.

The experiments performed inside the plasma chamber (see chapter 7 [18]) show that the electron fluxes are more intense and spatially much more confined to a star-like structure than the ion populations. This observation cannot be assessed with the information presented in figures 47 and 48 as no scales are given. We can only state that the simulation results agree in principle with our findings.

The group points out that the spatial distributions of the different electron populations (cold and warm) vary greatly [7]. In that publication the simulations show, that the hottest electrons are found close to the resonance surface while the colder electrons populate the regions closer to the center of the source. In the closest vicinity of the axis only the coldest electrons accumulate. As the percentage of electrons in a that low energy domain is negligible, a nearly electron-free zone is established at the axis. The size of that region is predicted (depending on the energy) to be a few millimeters in diameter [7, 6]. This is illustrated in figure 49. Here, the white region in the center defines the electron-depleted area (for the energies mentioned in the caption). Unfortunately, we cannot verify this prediction by the experiments described in chapter 7. The spatial resolution of the detector prohibits the detection of a particle-free zone in the center of the source with an approximate size of a few millimeters.

In conclusion, our experimental observations substantiate, at least at a qualitative level, the simulation results although it is not clear whether the ion and electron populations show exactly the same characteristics: the electron component is experimentally found to be spatially much more confined and more intense than that of the ions. In addition, some features of the simulation can not be resolved by the experiments.

Finally, we point out that the simulations predict a so-called "double-layer" (DL) [6] in which a structure of the shape of the (ellipsoidal) ECR volume is formed by the warm and hot electrons of the plasma that are well-confined by the magnetic trap. This layer is characterized by its negative potential produced by the excess of negative charges very close to the ECR layer. The diffusive ions are

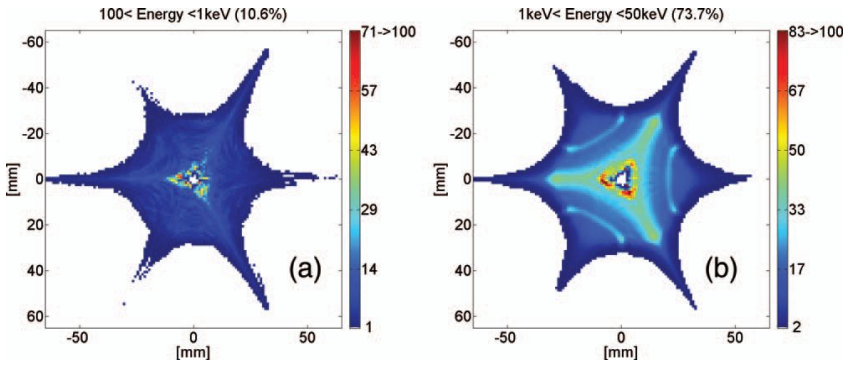

Figure 49: Electron density distribution: (a) energy between 100 eV and 1 keV; (b) energy between 1 keV and 50 keV. From [7] Reprinted with permission from L. Neri, D. Mascali, L. Celona, S. Gammino, and G. Ciavola, Review of Scientific Instruments, 83, 02A330, 2012. Copyright 2012, American Institute of Physics.

arranged just outside this structure establishing a self-consistent positive potential. These simulation findings are supported by experimental results reported by [40]. Our measurements presented in chapter 7 (see figure 4 in that publication) show in principle a very similar situation with the difference that is has been recorded in the outer regions of the plasma. We see a strong electron population with star-like symmetry which is well-confined by the magnetic field lines. The electrons are surrounded by less intense and spatially less confined ions. We are able to clearly separate the electrons from the ions because we can measure the currents. This implies that the concept of quasi-neutrality breaks down in the outer regions of ECR plasmas. When further approaching the bulk plasma, i.e. moving inward, we are still able to separate the electron- from the ion-dominated areas, which further reinforces the point made above.

We believe this to be an interesting finding that needs further study. This behavior could well be caused by the same mechanism that is described in the previous paragraph to explain the double layer inside the plasma (see above or [6]).

9 CONCLUSIONS

In this thesis, we presented the experimentally determined, spatially resolved distributions of charged particles along the ion-optical axis of an ECR ion source with the focus on the extraction region. Besides showing the current distributions (i.e. the beam profiles integrated over all charge states) in high spatial resolution in absolute values, we also showed spatially resolved measurements of the current density of different ion species in the plane of the plasma electrode and in the object plane of the bending magnet. To acquire data with such a high degree of information content and in that high precision, we developed new systems for beam diagnostics and combined them with existing systems. Much of the vacuum-sided detector hardware is based on the well-established and proven FC technique. These investigations confirmed several predictions: Each triangular or star-shaped structure in the beam profiles of strongly focused ion beams is dominated by ions of one charge state. At the extraction, the various ion species are each grouped into bloated triangular structures. Their orientation is defined by the radial magnetic field and their radial extend decreases for increasing charge states. The current density of each particular ion species increases towards the center of the beam where, as a consequence, the total current density peaks. Investigations performed inside the plasma chamber close to the plasma electrode were performed with a third, customized detector. They provided the first spatially resolved current distributions in that region. The measurements differentiate between positive and negative currents (i.e. ions and electrons). The electrons are found to be arranged in a spatially well-confined triangular shape defined by the magnetic fields with their intensity increasing towards the center. They are surrounded by a spatially less-confined and less-intense ion population. The observations of currents of both signs (positive and negative) in the presented pattern raises the question whether quasi-neutrality is still valid at these outer plasma regions. In fact, these patterns are still well distinguishable even when approaching the resonance zone. The results of this thesis can qualitatively be transfered to other ECR ion sources with hexapolar confinement. From the observed sputter marks and the measured Bremsstrahlung-spectra a new approach for the creation of the sputter marks is developed. The broad structures we agree to be created by the (higher-charged) ions accelerated by the plasma potential while the thin groves seem to have their origin in the hot electrons with energies above $\approx 200\,\mathrm{keV}$.

10

OUTLOOK

The FCA-detector [15] for acquiring beam profiles will be used in the framework of two different projects in the near future:

We started a collaboration with Emily Lamour and her team from the Paris Institute of Nanosciences (INSP) and the University Pierre et Marie Curie (UPMC) in France. Within the scope of the FISIC (Fast Ion Slow Ion Collision)-project, ion-ion collisions in the intermediate velocity regime are to be investigated. Here, the cross-sections for electron-capture, ionization, and excitation are not well known while the stopping power is maximum. The experiments will be performed at GANIL (Grand Accélérateur National d'Ions Lourds) in France. The FCA-detector will be used to accurately determine the beam profiles in absolute values as this information is crucial for those experiments. For this purpose, the aluminum-parts of the detector have been replaced by parts manufactured of stainless steel to work under UHV-conditions.

At the Helmholtzzentrum für Schwerionenforschung Darmstadt (GSI Darmstadt) we will use the detector to benchmark its performance against scintillation screens often used for beam-profile acquisition in the LEBT (Low Energy Beam Transport). The main interests are to compare the information content of the FCA-detector with that of the screens, and to see how linear the light-yield of the scintillation screens indeed is.

Another point of interest regarding ECRIS are plasma instabilities and oscillations. Observations of currents extracted from ECR ion sources driven in continuous wave operation show oscillations at frequencies in the sub- or low-kHz-range [41]. As reported in that reference, the amplitude of these oscillations typically lies in the range of about 10 % with respect to the continuously measured current (the mean DC component) of the particular ion species. The amplitude of these oscillations is observed to increase for the higher-charged ion species. The identification of the reason(s) for these oscillations is a major task. Motivated by a private conversation with Hannu Koivisto [from JYFL, Finland] in 2012, the measuring techniques presented within this thesis could turn out to be useful instruments to gain deeper insight into these oscillating processes inside the plasma, as well. With the detector presented in [16] (the puller electrode with reduced aperture but without the FC implemented), it should be possible to measure the oscillation frequencies and amplitudes of different ion species extracted from different regions of the neutral plasma sheath. Again, the unique 3D-movable puller electrode of our source would provide us with the opportunity to gain spatially resolved experimental data. Using the detector introduced in [18] (the planar multi-segment current-detector), different regions inside the plasma chamber can be probed for oscillations with the detector-given spatial resolution. This measuring technique allows to probe the electron-dominated regions for oscillations, as well. If each of the different

ion species oscillates at another frequency, this information could be used as a fingerprint for identification. If this was provided, the source regions of the different ion species could possibly be tracked into the plasma.

BIBLIOGRAPHY

[1] R. Geller. *Electron cyclotron resonance ion sources and ECR plasmas*. Institute of Physics Pub., 1996.

[2] U. Stroth. *Plasmaphysik: Phänomene, Grundlagen, Anwendungen*. Studium (Vieweg + Teubner). Vieweg+Teubner Verlag, 2011.

[3] S. Saminathan. *Extraction and Transport of Ion Beams from an ECR Ion Source*. PhD thesis, Rijksuniversiteit Groningen, 2011.

[4] L. Celona G. Ciavola N. Gambino S. Gammino R. Miracoli L. Neri D. Mascali, G. Castro and F. Maimone. Some considerations about frequency tuning effect in ecris plasmas. Grenoble, France, 2010. 19th International Workshop on ECR Ion Sources.

[5] D. Mascali, L. Neri, S. Gammino, L. Celona, G. Ciavola, N. Gambino, R. Miracoli, and S. Chikin. Plasma ion dynamics and beam formation in electron cyclotron resonance ion sources. *Review of Scientific Instruments*, 81(2):02A334, 2010.

[6] D. Mascali, S. Gammino, L. Celona, and G. Ciavola. Towards a better comprehension of plasma formation and heating in high performances electron cyclotron resonance ion sources (invited). *Review of Scientific Instruments*, 83(2):02A336, 2012.

[7] L. Neri, D. Mascali, L. Celona, S. Gammino, and G. Ciavola. A 3d monte carlo code for the modeling of plasma dynamics and beam formation mechanism in electron cyclotron resonance ion sources. *Review of Scientific Instruments*, 83(2):02A330, 2012.

[8] P. Spädtke. Model for the description of ion beam extraction from electron cyclotron resonance ion sources. *Review of Scientific Instruments*, 81(2):02B725, 2010.

[9] S B Van der Geer and M J De Loos. General particle tracer: A 3d code for accelerator and beam line design. 1998.

[10] INTEGRATED Engineering Software. Lorentz3d, 2012.

[11] J. Qiang, D. Todd, and D. Leitner. A 3D model for ion beam formation and transport simulation. *Computer Physics Communications*, 175:416–423, September 2006.

[12] V. Mironov and J. P. M. Beijers. Three-dimensional simulations of ion dynamics in the plasma of an electron cyclotron resonance ion source. *Phys. Rev. ST Accel. Beams*, 12:073501, Jul 2009.

[13] P. Spädtke, R. Lang, J. Mäder, J. Rossbach, K. Tinschert, and J.Stetson. Ion beam extracted from a 14 ghz ecris of caprice type. Lanzhou, China, 2007. 17th International Workshop on ECR Ion Sources.

[14] D. S. Todd, D. Leitner, and M.Strohmeier. Low energy beam diagnostics at the venus ecr ion source, 2008.

[15] Lauri Panitzsch, Michael Stalder, and Robert F. Wimmer-Schweingruber. Direct high-resolution ion beam-profile imaging using a position-sensitive faraday cup array. *Review of Scientific Instruments*, 80(11):113302, 2009.

[16] Lauri Panitzsch, Thies Peleikis, Michael Stalder, and Robert F. Wimmer-Schweingruber. Spatially resolved charge-state and current-density distributions at the extraction of an electron cyclotron resonance ion source. *Review of Scientific Instruments*, 82(9):093302, 2011.

[17] Lauri Panitzsch, Michael Stalder, and Robert F. Wimmer-Schweingruber. Spatially resolved measurements of electron cyclotron resonance ion source beam profile characteristics. *Review of Scientific Instruments*, 82(3):033302, 2011.

[18] Lauri Panitzsch, Thies Peleikis, Stephan Böttcher, Michael Stalder, and Robert F. Wimmer-Schweingruber. Current density distributions and sputter marks in electron cyclotron resonance ion sources. *Review of Scientific Instruments*, 84(1):013303, 2013.

[19] F. W. Meyer, editor. *Application of ECR ion source beams in atomic physics*, 1987.

[20] A. Girard, D. Hitz, G. Melin, and K. Serebrennikov. Electron cyclotron resonance plasmas and electron cyclotron resonance ion sources: Physics and technology (invited). *Review of Scientific Instruments*, 75(5):1381–1388, 2004.

[21] I.G. Brown. *The Physics and Technology of Ion Sources*. Wiley, 2006.

[22] C. Perret, A. Girard, H. Khodja, and G. Melin. Limitations to the plasma energy and density in electron cyclotron resonance ion sources. *Physics of Plasmas*, 6(8):3408–3415, 1999.

[23] Thomas A. Carlson, C.W. Nestor Jr., Neil Wasserman, and J.D. Mcdowell. Calculated ionization potentials for multiply charged ions. *Atomic Data and Nuclear Data Tables*, 2(0):63 – 99, 1970.

[24] Wolfgang Lotz. An empirical formula for the electron-impact ionization cross-section. *Zeitschrift für Physik*, 206:205–211, 1967.

[25] Alfred Müller and Erhard Salzborn. Scaling of cross sections for multiple electron transfer to highly charged ions colliding with atoms and molecules. *Physics Letters A*, 62(6):391 – 394, 1977.

[26] S.V. Golubev, S.V. Razin, V.E. Semenov, A.N. Smirnov, A.V. Vodopyanov, and V.G. Zorin. Features of quasi-gasdynamic plasma confinement in ecr ion source with powerful microwave pumping. In *Electronics and Radiophysics*

of Ultra-High Frequencies, 1999. International University Conference Proceedings, pages 451 –454, aug 1999.

[27] Denis Hitz, Gérard Melin, and Alain Girard. Fundamental aspects of electron cyclotron resonance ion sources: From classical to large superconducting devices (invited). *Review of Scientific Instruments*, 71(2):839–845, 2000.

[28] H Koivisto, P Frondelius, T Ropponen, P Suominen, O Tarvainen, and R C Vondrasek. Ecr ion source plasma related research and development at jyfl. 2005.

[29] A. G. Drentje, A. Girard, D. Hitz, and G. Melin. Role of low charge state ions in electron cyclotron resonance ion source plasmas. *Review of Scientific Instruments*, 71(2):623–626, 2000.

[30] O. Tarvainen, P. Suominen, and H. Koivisto. A new plasma potential measurement instrument for plasma ion sources. *Review of Scientific Instruments*, 75(10):3138–3145, 2004.

[31] K U Riemann. The bohm criterion and sheath formation. *Journal of Physics D: Applied Physics*, 24(4):493, 1991.

[32] G. D. Severn. A note on the plasma sheath and the bohm criterion. *American Journal of Physics*, 75(1):92–94, 2007.

[33] Noah Hershkowitz. Sheaths: More complicated than you think. *Physics of Plasmas*, 12(5):055502, 2005.

[34] H. R. Kremers, J. P. M. Beijers, and S. Brandenburg. Characteristics of the kvi electron cyclotron resonance ion source. *Review of Scientific Instruments*, 77(3):03A311, 2006.

[35] J. P. M. Beijers, H. R. Kremers, V. Mironov, J. Mulder, S. Saminathan, and S. Brandenburg. Ion source development at kvi. *Review of Scientific Instruments*, 79(2):02A320, 2008.

[36] W. Glaser. *Grundlagen der Elektronenoptik*. Wien, 1952.

[37] D Wutte, M A Leitner, and C M Lyneis. Emittance measurements for high charge state ion beams extracted from the aecr-u ion source. *Physica Scripta*, 2001(T92):247, 2001.

[38] M.A. Leitner, C.M. Wutte, and Lyneis C.M. Design of the extraction system of the superconducting ecr ion source venus. In *Particle Accelerator Conference, 2001. PAC. IEEE*, 2001.

[39] D Winklehner, D Todd, J Benitez, M Strohmeier, D Grote, and D Leitner. Comparison of extraction and beam transport simulations with emittance measurements from the ecr ion source venus. *Journal of Instrumentation*, 5(12):P12001, 2010.

[40] K. Takahashi, T. Kaneko, and R. Hatakeyama. Double layer created by electron cyclotron resonance heating in an inhomogeneously magnetized plasma with high-speed ion flow. *Physics of Plasmas*, 15(7):072108, 2008.

[41] O. Tarvainen, Toivanen V., H. Koivisto, J. Komppula, T Kalvas, C. M. Lyneis, and M. Strohmeier. An experimental study of ecris plasma stability and oscillation of beam current. Sydney, Australia, 2012. 20th International Workshop on ECR Ion Sources.

EIDESSTATTLICHE ERKLÄRUNG

Ich versichere an Eides Statt durch meine eigenhändige Unterschrift, dass ich die vorliegende Arbeit selbstständig und ohne fremde Hilfe angefertigt habe. Stellen, die wörtlich oder dem Sinn nach auf Publikationen anderer Autoren beruhen, sind als solche kenntlich gemacht. Ich versichere außerdem, dass ich keine andere als die angegebene Literatur verwendet habe. Diese Versicherung bezieht sich auch auf alle in dieser Arbeit enthaltenen Grafiken, Skizzen, bildlichen Darstellungen und dergleichen.
Die Arbeit als Ganzes wurde bisher keiner anderen Prüfungsbehörde vorgelegt. Teile der Arbeit wurden bereits in begutachteten Fachzeitschriften veröffentlicht und sind als solche erkennbar. Die Quellennachweise der in den einzelnen Veröffentlichungen referenzierten Inhalte finden sich in der jeweiligen Veröffentlichung selbst und werden nicht zusätzlich im Quellennachweis dieser Arbeit aufgeführt. Für das Einbinden der Veröffentlichungen in diese Arbeit wurde die ausdrückliche Genehmigung der publizierenden Fachzeitschrift eingeholt.
Außerdem erkläre ich, dass die Arbeit unter Einhaltung der Regeln guter wissenschaftlicher Praxis der Deutschen Forschungsgemeinschaft entstanden ist.

Kiel, Dezember 2012

Lauri Panitzsch